SURFACE ENHANCED VIBRATIONAL SPECTROSCOPY AND HIGH PRESSURE STUDIES OF BIOMOLECULES

By

NAVEEN KUMAR

PHYS01201304023

Bhabha Atomic Research Centre, Mumbai

A thesis submitted to the

Board of Studies in Physical Sciences

In partial fulfillment of requirements

for the Degree of

DOCTOR OF PHILOSOPHY

of

HOMI BHABHA NATIONAL INSTITUTE

December, 2019

Homi Bhabha National Institute

Recommendations of the Viva Voce Committee

As members of the Viva Voce Committee, we certify that we have read the dissertation prepared by Naveen Kumar entitled "Surface enhanced vibrational spectroscopy and high pressure studies of biomolecules" and recommend that it may be accepted as fulfilling the thesis requirement for the award of Degree of Doctor of Philosophy.

Chairman – Prof. S. M. Yusuf	Md. Yusuf 31.10.2020
Guide / Convener – Prof. R. J. Kshirsagar	R J Kshirsagar 31.10.2020
Examiner 1- Dr. Dheeraj Kumar Singh	
Examiner 2- Dr. Pallavi Ghalsasi	P P Ghalsasi
Member 1- Prof. S. Kapoor	
Member 2- Prof. Alka A. Ingale	A A Ingale
Member 3- Prof. Nandini Garg	Nandini 31-10-2020

Final approval and acceptance of this thesis is contingent upon the candidate's submission of the final copies of the thesis to HBNI.

I/We hereby certify that I/we have read this thesis prepared under my/our direction and recommend that it may be accepted as fulfilling the thesis requirement.

Date: 31.10.2020

Place: BARC, Mumbai

R J Kshirsagar

Signature

Guide

STATEMENT BY AUTHOR

This dissertation has been submitted in partial fulfilment of requirements for an advanced degree at Homi Bhabha National Institute (HBNI) and is deposited in the Library to be made available to borrowers under rules of the HBNI.

Brief quotations from this dissertation are allowable without special permission, provided that accurate acknowledgement of source is made. Requests for permission for extended quotation from or reproduction of this manuscript in whole or in part may be granted by the Competent Authority of HBNI when in his or her judgment the proposed use of the material is in the interests of scholarship. In all other instances, however, permission must be obtained from the author.

Naveen Kumar

DECLARATION

I, hereby declare that the investigation presented in the thesis has been carried out by me. The work is original and has not been submitted earlier as a whole or in part for a degree / diploma at this or any other Institution / University.

Naveen Kumar

List of Publications arising from the thesis

(a) Publications in Refereed Journal:

1. Plasmon–induced dimerization of Thiazolidine-2, 4-dione on Silver nanoparticles-Revealed by surface- enhanced Raman scattering study
   Naveen Kumar, S. Thomas, R. Rao, N. Maiti, R. J. Kshirsagar;
   Journal of physical chemistry A, 2019, 123, 9770-9780.
2. Surface-enhanced Raman scattering based sensing of trans-urocanic acid, an epidermal photoreceptor using silver nanoparticles aided by density functional theoretical calculations.
   Naveen Kumar, S. Thomas, R. Rao, N. Maiti, R. J. Kshirsagar
   Journal of Raman Spectroscopy, 2019, 50, 837–846.
3. Investigation on the adsorption characteristics of sodium benzoate and taurine on gold nanoparticle film by ATR-FTIR spectroscopy.
   Naveen Kumar, S. Thomas, R. B. Tokas, R. J. Kshirsagar
   Spectrochimica Acta Part A: Molecular and Biomolecular Spectroscopy, 2014, 118, 614-618.
4. SEIRA studies of uracil adsorbed on wet-chemically prepared gold nanoparticles film on glass substrate -Effect of morphology of film.
   Naveen Kumar, S. Thomas, R.B. Tokas, R. J. Kshirsagar
   Spectrochimica Acta Part A: Molecular and Biomolecular Spectroscopy, 2014, 129, 359–364.
5. Effect of pressure on trans-urocanic acid probed by Raman spectroscopy (manuscript prepared): To be submitted
   Naveen kumar, Meera Varma, H. K. Poswal, S. Thomas, C. Murli, R. J. Kshirsagar

(b) Other Publications:

AIP (American Institute of Physics) Proceedings:

1. Surface-enhanced infrared absorption spectroscopy of cytosine using gold film deposited on CaF_2 substrate.
   Naveen Kumar, S. Thomas, R. B. Tokas, N. Padma, R. J. Kshirsagar
   AIP Conference Proceedings, 2018, 1942, 080013.
2. FTIR study of thin film of uracil on silanised glass substrate using attenuated total reflection (ATR).

Naveen Kumar, S. Thomas, R. J. Kshirsagar;

AIP Conference Proceedings, 2013, 1512, 716.

Conference Papers:

1. High pressure raman study of trans-urocanic acid.

   Naveen kumar, Meera Varma, H. K. Poswal, S. Thomas, C. Murli, R. J. Kshirsagar; Accepted in 15th DAE-BRNS Biennial Trombay Symposium on Radiation & Photochemistry (TSRP-2020).

2. SERS studies on the adsorption of taurine on silver nanoparticle film deposited on glass Substrate.

   Naveen Kumar, S. Thomas, Rekha Rao, R. J. Kshirsagar

   7th International Conference on Perspectives in Vibrational Spectroscopy (ICOPVS-2018), DAE Convention Centre, Mumbai, Nov. 25-29, 2018, Page No.45.

3. Surface-enhanced infrared absorption (SEIRA) studies of uracil adsorbed onto gold nanoparticles (AuNp) film.

   Naveen Kumar, H. K. Poswal, S. Thomas, R. J. Kshirsagar, S. M. Sharma

   DAE-BRNS Conference on Condensed Matter Physics under Extreme Conditions (CoMPEC-2016), 86, April 13-16, 2016.

4. Surface enhanced Raman scattering studies of uracil on silver nanoparticles film.

   Naveen Kumar, H. K. Poswal, S. Thomas, R. J. Kshirsagar, S. M. Sharma

   DAE-BRNS Conference on Condensed Matter Physics under Extreme Conditions (CoMPEC-2016), 85, April 13-16, 2016.

5. Study of Cysteine Adsorbed on Gold Nanoparticles Film: Probed by ATR-FTIR Spectroscopy.

   Naveen Kumar, S. Thomas, R.J. Kshirsagar

   DAE-BRNS 5th Interdisciplinary Symposium on Material Chemistry (ISMC), December 9-13, 346 (2014).

Dedicated

To

My parents

ACKNOWLEDGEMENTS

The accomplishment of the dissertation was possible with the unconditional support and help from several amazing people. I would like to express my sincere thanks to all of them.

First and foremost, I would like to express my sincere gratitude to my advisor Prof. R. J. Kshirsagar for his constant support and motivation. His absolute guidance and support were present all the time of my Ph.D research and writing of the thesis. His immense knowledge and expertise in the field of molecular spectroscopy were instrumental in establishing the overall direction of the research works and helped me to grow as a research scientist. I would also like to express my sincere thanks to Dr. Susy Thomas for her enormous support, guidance and scientific discussions. Her proficiency in the surface enhanced spectroscopy field has helped me to move forward with research investigations. I owe a lot of gratitude to her for always being present for me and I feel privileged to be associated with a person like her during my life. I do take the opportunity to thank my doctoral committee members, Prof. S. M. Sharma, Prof. S. M. Yusuf, Prof. S. Kapoor, Prof. A. Ingale and Prof. N. Garg for their valuable suggestions, insightful comments, support and guidance throughout my Ph.D tenure. I also wish to thank Dr. R. C. Rannot for his constant support, motivation and encouragement.

I sincerely thank my collaborator, Dr. N. Maiti for carrying out the vibrational frequencies calculations using density functional theory method which were instrumental in analysing the data. I also thank my other collaborators for their help in conducting the experiments; Dr. R. Rao for Raman measurements, Dr. N. Padma for providing the gold film, Dr. C. Murli and Dr. H. K. Poswal for high pressure Raman experiments and Dr. R. B. Tokas for AFM measurements.

Next, I wish to thank my senior colleagues Dr. H. Bhatt and Shri A. K. Pal for their fruitful and conclusive scientific discussions and for helping me to get out from various

difficulties. I also wish to thank my colleagues and friends Shivkumar, Naini, Meera and Swayam for their support and kind help. I like to express my sincere thank to Dr. K. Sunanda, Shri. A. K. Poswal and Kum. A. Gupta for helping me in numerous ways during my Ph.D.

It is my fortune to thank my friends, Awadh, Amresh, Jalaj, Vikash, Neeraj, Sanjeev, Aradhana and all my friends for their love and making my life cheerful.

Heartiest thanks to my parents, Amma and Papa for their unconditional love, sacrifice and support. This journey would not have been possible without their blessing. Their sacrifice will remain my inspiration throughout my life. Many thanks to my beloved sisters, Mamta, Amita, Akansha and my elder brother Shyam sunder and younger brother Neelkamal for their love and affection. I also take the opportunity to thank my mother in law, Madhu and sister in law, Sona for their constant encouragement during the Ph.D tenure. I am very grateful to my pretty daughter Avani for making my life joyful and beautiful. I owe my deepest gratitude towards my wife Jagrati Gupta for her eternal support, caring and understanding my goals and aspirations. Without her help and sacrifice, I would not have been able to complete much of what I have intended to do and achieve.

CONTENTS

SUMMARY

Localized surface plasmon resonance (LSPR) property of plasmonic metal nanoparticles (e.g. Au, Ag) has attracted wide attention due to exhibition of amplified field around the nanoparticles (NP) and generation of hot carriers (electrons and holes). Near field enhancement of metal NP has given rise to a new branch of spectroscopy known as surface enhanced vibrational spectroscopy (SEVS) which includes surface-enhanced Raman scattering (SERS) and its complementary technique, surface-enhanced infrared absorption (SEIRA) spectroscopy. Both these techniques have the ability to acquire vibrational spectrum of various molecular systems including biological molecules with unprecedented sensitivity and molecular specificity. In addition, non-radiative decay of LSPR leading to generation of hot carriers has the potential to initiate several chemical reactions and form new molecules on metal NP surface. These reactions are termed as plasmon induced chemical reaction and can be probed by SERS method.

The charge-transfer (CT) process between metal substrates and molecules has attracted much interest because of its potential applications in physics and chemistry, although the phenomenon is poorly understood. High pressure vibrational spectroscopic tool can provide a better understanding of the CT process. However, under pressure, both the CT process and the molecular structure gets affected and therefore, to comprehend the CT process, it is important to first understand the behaviour of molecule (without the metal) under external pressure.

Hence the thesis entitled “Surface enhanced vibrational spectroscopy and high pressure studies of biomolecules” elaborate the research works carried out on SEVS and high pressure studies of several important biomolecules.

SERS study of trans-urocanic acid (t-UCA), an epidermal molecule found in skin, has enabled us to probe the vibrational finger print spectrum of t-UCA down to 50 picomolar concentration with good signal to noise ratio which was possible due to the near field enhancement of silver NP (Ag NP). The change in molecular orientation from slight titled to flat geometry on the Ag NP surface on decreasing the molecular concentration was deduced and supported by the DFT calculated optimized geometry. The SERS results of thiazolidine-2 4-dione (TZD), points to the other aspect of LSPR such as plasmon-induced chemical reaction. TZD on Ag NP was found to dimerise by undergoing self condensation reaction via interfacial indirect transfer of hot-electrons generated by non-radiative decay of LSPR.

SEIRA (complementary method to SERS) studies of various important biomolecules were carried out using Fourier transform infrared spectroscopy coupled with attenuated total internal reflection (ATR). ATR-SEIRA studies were carried out using a wet chemically prepared Au NP films on glass substrate. ATR-SEIRA studies of sodium benzoate and taurine suggest the presence of both chemisorbed and physisorbed layers of both sodium benzoate (food preservative) and taurine (amino acid) on the Au NP film with bottom layer chemically bound to Au NP through carboxylate and sulphonate groups, respectively. In SEIRA study of uracil (RNA base), impact of morphology (varied by changing the deposition time) of wet-chemically fabricated Au NP films indicate that SEIRA intensity of adsorbed molecules is greatly affected by the Au NP film morphology. The tuning of morphology has allowed us to detect vibrational finger print of uracil down to 1 μM.

High pressure Raman investigation on t-UCA up to ~14 GPa indicates onset of ring opening polymerization involving the imidazole ring at pressure 1.4 GPa, and on further compression, across 7.5 GPa, an irreversible conformational transformation of t-UCA monomer into cis form.

LIST OF FIGURES

LIST OF TABLES

LIST OF SCHEMES

CHAPTER 1.

INTRODUCTION

1.1. SURFACE ENHANCED VIBRATIONAL SPECTROSCOPY (SEVS)

The structural characterization and identification of molecular systems is very important and necessary for elucidating various molecular properties, since the molecular structure of materials holds the key to understand their complex functions and behaviour in various environments. Therefore, during the last many decades, there has been increasing interest and demand of sensitive techniques to obtain this information. Vibrational spectroscopy technique has been widely used to characterize and identify the molecules based on characteristic spectral fingerprints generated by the molecular vibrations when illuminated by electromagnetic (EM) radiation or by inelastic neutrons scattering (INS) [1]. Vibrational spectroscopy using EM radiation, which comprises of infrared (IR) absorption and Raman scattering spectroscopy, emerges as a potentially attractive, simple, molecule specific and label-free noninvasive approach to study various types of molecules used in a variety of scientific fields such as physics, chemistry, geology, biology, forensic, environmental and biomedical sciences [2-5]. Basically, in Raman spectroscopy, molecular vibrational features are obtained based on inelastic scattering of photons by a molecule, which was first experimentally observed by Raman [6], whereas in IR absorption spectroscopy, molecular vibrational features are generated by the absorption of EM radiation by molecule. Both these spectroscopy techniques are sensitive to different types of vibrations and thus provide complementary vibrational spectrum features. Mostly, all the molecules have their molecular fingerprint vibrational spectra in mid infrared range [7] as shown in Figure 1.1 [8]. Both the techniques are capable of providing detailed information about the molecular structure and compositional properties of materials. The advantage of these techniques is that they can be used to probe the molecules in solid, liquid or gas phase. Additionally, optical approaches used in these techniques are nondestructive in nature and samples may be further analyzed with additional characterization methods if required. Vibrational spectroscopy can also be

used to get the information regarding the chemical and physical nature of the adsorbate on various kinds of substrates.

Unfortunately, the application of conventional Raman scattering and IR absorption techniques are rather limited because of the associated weak Raman scattering (10^{-25}-10^{-30} cm^2) and IR absorption cross section (~10^{-21} cm^2/molecule) of various bio and organic molecules compared to other spectroscopic techniques like UV–visible (~10^{-18} cm^2/molecule) and fluorescence (~10^{-24} - 10^{-14} cm^2/molecule) [9-12]. Hence, both these methods often fail to provide the substantial intensity of vibrational spectral features of samples, particularly from the systems where the number of molecules which participate in interaction with EM radiation are very less. However, the intensity of vibrational spectral features of molecules can be significantly enhanced if molecules are placed close to the surfaces of plasmonic metallic nanostructures. The first observation of the enhancement in Raman signal of molecule (pyridine) adsorbed on roughened silver was made in 1974 [13]. However, at that

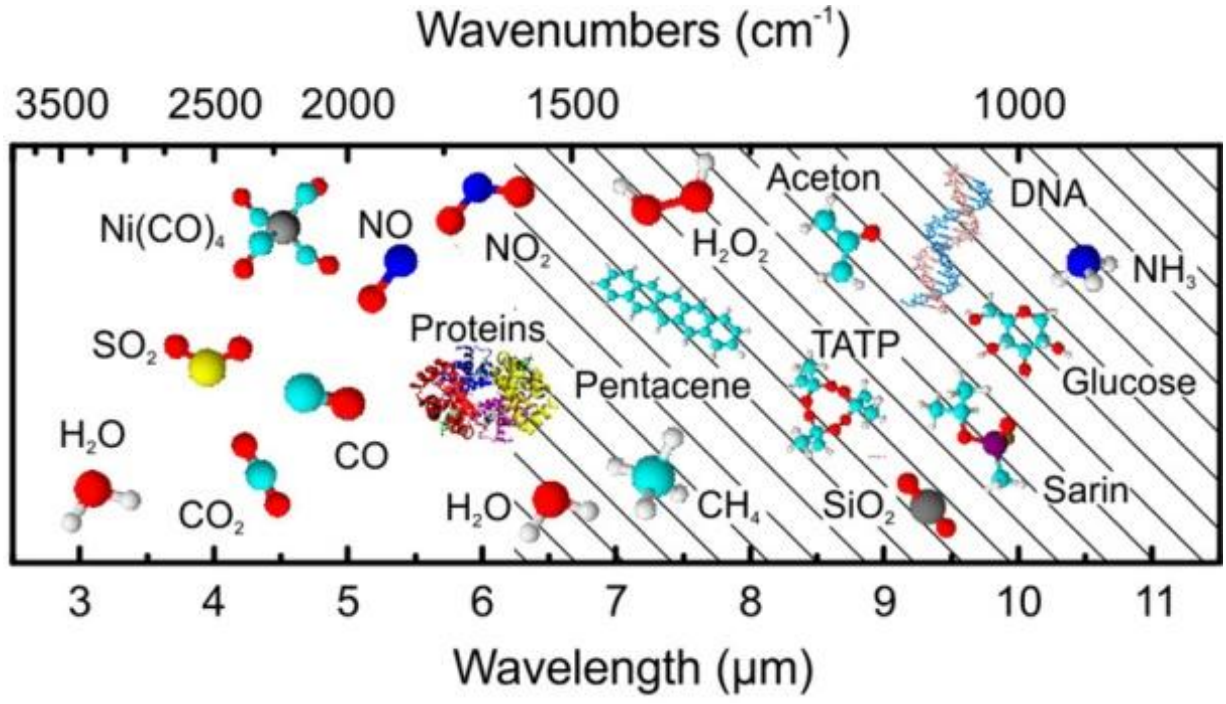

Figure 1.1. Characteristic infrared vibrations of selected molecular species (reproduced with the permission from Ref. [8]).

time the authors did not recognize that enhancement in Raman signal was due to the enhanced EM field around rough silver electrode. It was explained that the enhanced Raman signal was due to the large number of molecules from the increased surface area on the rough silver electrode. In 1977, two groups independently confirmed that enhanced Raman signal of pyridine with rough silver metal electrode cannot be explained by an increase in surface area alone [14, 15]. The amplification of the Raman scattering intensities was then attributed to EM field enhancement [14] and to chemical enhancement [14, 15]. Following the discovery of the enhanced Raman signal, the search of enhancement in IR signal was pursued and subsequently the enhancement in IR absorption signal of molecular monolayers adsorbed on metal thin film was also observed [16], and enhancement in IR signal was also attributed to EM field enhancement. It is now generally established that enhancement in the vibrational signal is mainly attributed to amplification of the EM field near the metal surface due to the resonant excitation of localized surface plasmon resonances (LSPR). LSPR is the coherent oscillation of conduction electrons confined in the metal NP when excited by EM radiation, and is preferentially found in plasmonic materials, which are usually coinage metals (e.g., silver (Ag), gold (Au)) with nanoscale dimension. In general, Ag and Au nanoparticles (NP) and their films on dielectric substrate are most often used metals for the above applications [17-22]. The attractive optical property of metal NP stems from their LSPR which gives rise to a strong EM field near the metal NP surface and forms the basis of all surface-enhanced spectroscopy including surface-enhanced Raman scattering (SERS) and surface-enhanced infrared absorption (SEIRA) spectroscopy as depicted in Figure 1.2 [20, 23, 24]. Since their discoveries, due to their high sensitivity and selectivity, both the SERS and SEIRA spectroscopy are gaining considerable attention from various fields such as physics, chemistry, biology and medical sciences.

In general, SERS entails higher order of enhancement factors than observed in SEIRA, since the SERS intensity is proportional to the fourth power of the incident electric field, whereas for SEIRA the enhancement is proportional to the square of the local electric field [25]. Although the enhancement factor of SEIRA is smaller than that of SERS, however due to higher IR absorption cross-section than the corresponding Raman cross-section, SIERA technique has also played an equally important role in the various research applications [25-27]. Taking into consideration the difference in excitation mechanisms, and molecular absorption/scattering cross sections, SERS and SEIRA should be considered complementary techniques in term of deriving the vibrational information of target molecules for various scientific applications [28]. Both these techniques have the ability to acquire vibrational spectrum of various molecular systems including biological molecules with unprecedented sensitivity and molecular specificity and remains as the most widely used optical methods for molecular sensing of biomolecules.

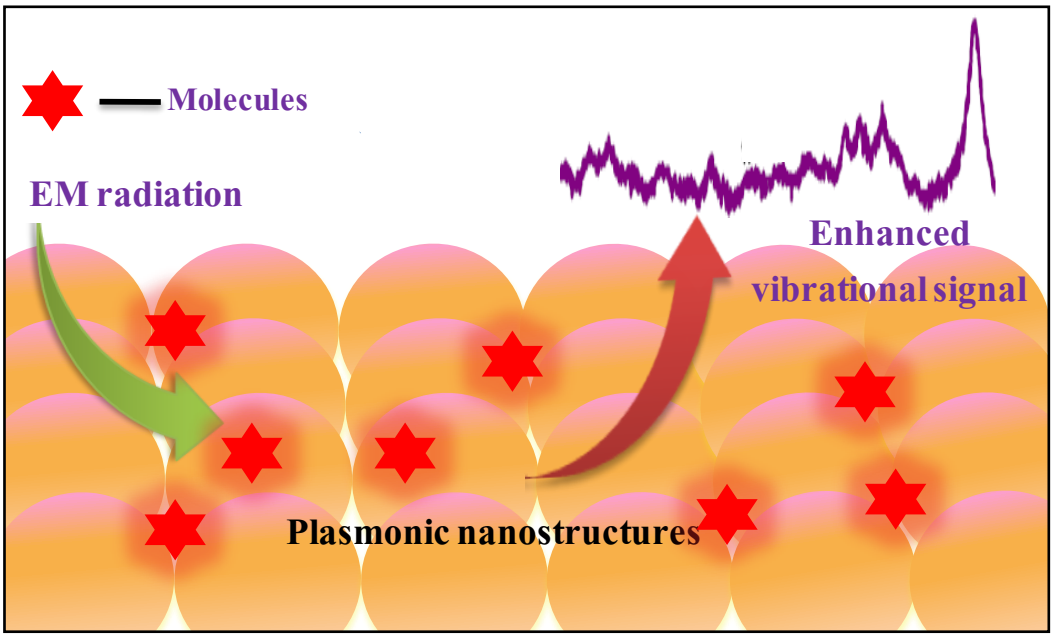

Figure 1.2. Scheme depicting the SEVS spectroscopy using plasmonic nanostructures.

1.1.1. SURFACE ENHANCED RAMAN SCATTERING (SERS) SPECTROSCOPY

SERS study requires the molecules to be in the vicinity of plasmonic nanostructure and thus, enhancement in the intensity of Raman mode can be obtained with the SERS method. Since the discovery of SERS, it has become a powerful spectroscopic technique, which has attracted widespread interest from various scientific disciplines including material, chemistry, physics, medical, biological and surface sciences [26, 29-31] due to its ultrahigh sensitivity and molecular specificity [10, 11]. It has been exploited to investigate the various types of bio-molecules such as amino acids, folic acid, glucose and nucleic acids for the medical as well as diagnostic applications and also used to generate the finger print spectra for the identification of various types of molecules present in aqueous environment at ultralow level concentration [29, 32-40]. Recently, SERS has been used to identify and characterize the biological and chemical analytes with concentrations as low as femtogram [41]. It has been applied as diagnostic and imaging tool for medical applications and for research focused on to interaction of metallic NP with cells [26, 31, 42]. It was also to investigate food additives contaminations [43] and to detect environmental pollutions [44, 45]. The research fields that are explored from SERS are not limited to signal enhancement but also used as a highly sensitive surface tool for probing the orientation, type of conformers for various applications and in elucidating the metal-adsorbate interaction [27, 29, 31, 46-54]. The orientation of molecules and type of conformers adsorbed on the metal substrate are probed by SERS with invocation of “surface selection rules” [55-59]. The knowledge about interactions/orientation of biomolecules with noble metal surfaces is significantly important to development of functional materials. Metallic NP of noble metals dispersed in water (colloid) are most frequently used substrates for SERS studies, because of their LSPR properties, high enhancement, excellent biocompatibility and controlled size and shape. In particular, the biocompatibility and interesting optical properties of noble metal NP have allowed to

development of many biomolecule-nanoparticles complexes for biomedical applications [17, 60, 61].

1.1.1.1. ENHANCEMENT MECHANISMS

Various experimental and theoretical works have been performed to understand the enhancement mechanisms of SERS. Although, the exact nature of enhancement involved in SERS is not fully understood but it is well accepted that the electromagnetic and chemical mechanisms contribute to total enhancement in SERS signal.

(A) ELECTROMAGNETIC ENHANCEMENT

The Electromagnetic enhancement mechanism is based on the amplification of the EM field around the metal NP generated by coupling of the radiation with the localized surface plasmon. Metal that possess negative real and small positive imaginary dielectric constants is capable of supporting LSPR phenomenon. Both Au and Ag metals have a negative real and small positive imaginary dielectric constant and known to exhibit LSPR phenomenon. The dielectric constants of Au and Ag metals are shown in Figure 1.3 [62]. When the metal NP are exposed to EM radiation, the surface electrons of metal gets polarized, and they accumulate alternatively on opposite ends of the metal NP as shown in Figure 1.4. This oscillating polarization of surface charges under the resonance condition (the collective oscillation frequency of valence electrons matches with the frequency of incident light) creates an enormous electric field around the metallic surface. This phenomenon is called as LSPR. The LSPR associated with noble metal nanostructures create sharp spectral absorption in visible range and strong EM field enhancement near the metal surface as shown in Figure 1.5. These enhanced fields are responsible for the remarkable enhancement of Raman signal of molecules located in close proximity to the metal surface.

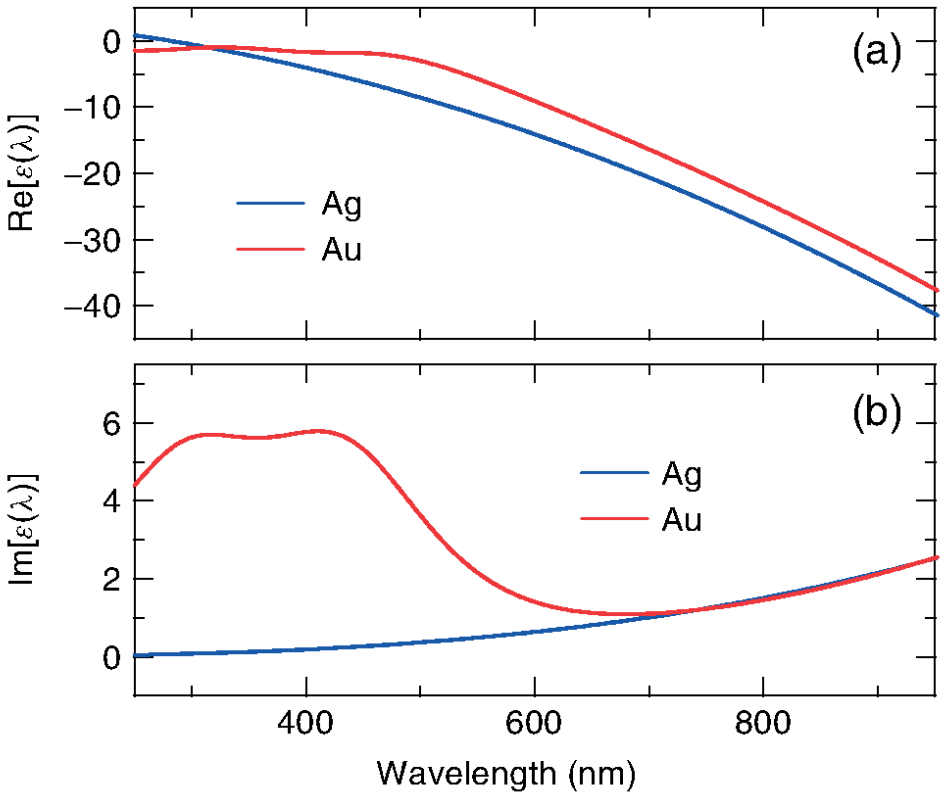

Figure 1.3. Dielectric functions of Ag and Au (reproduced with permission from Ref. [62]).

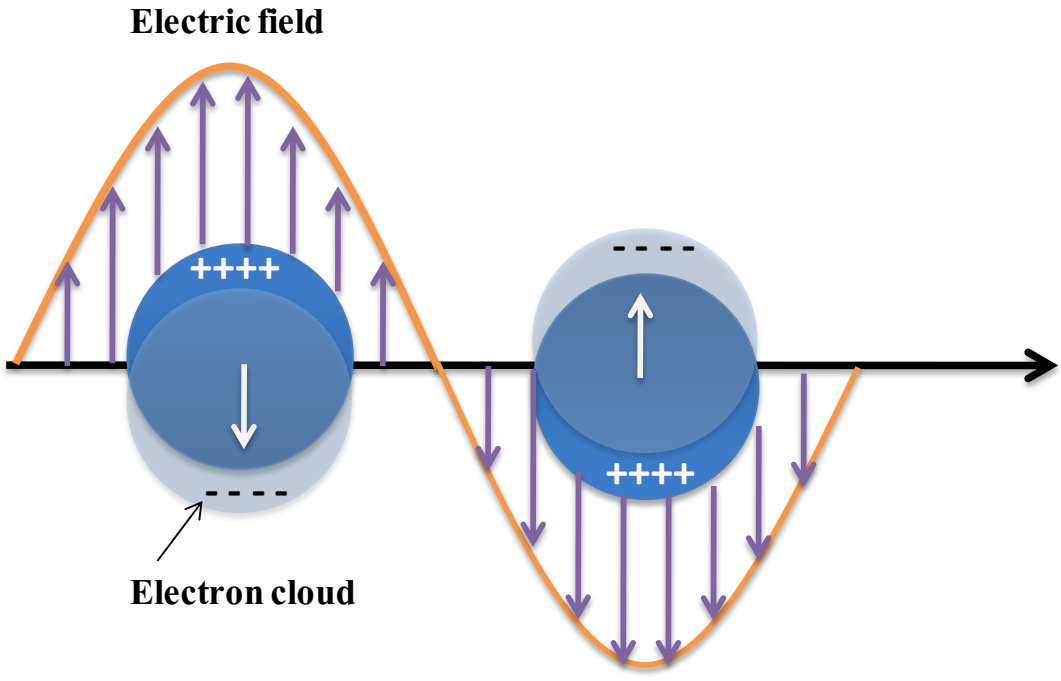

Figure 1.4. Illustration of localized surface plasmon.

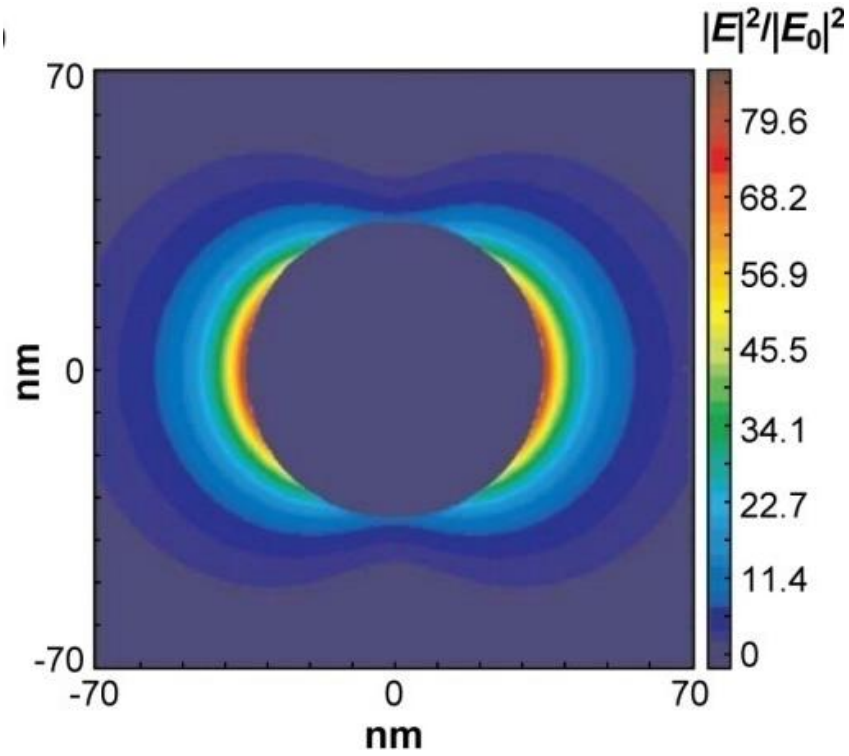

Figure 1.5. Extinction efficiency (ratio of cross section to effective area) of a spherical silver nanoparticle of 35 nm radius at wavelength corresponding to the plasmon extinction maximum (reproduced with permission from Ref. [63]).

To relate the LSPR frequency of a metal NP to the dielectric constant, the interaction of light with a spherical particle whose size is much smaller than the wavelength of light is considered. Under this circumstance, the electric field of the light can be taken to be constant, and the interaction is governed by electrostatics rather than electrodynamics. This is often called the quasistatic approximation (also called as dipole approximation) [23]. Let us consider ϵ_i and ϵ_m are the dielectric functions of metal and surrounding medium respectively and $E_0\hat{z}$ denote incident EM field vector in Z direction, where $\hat{z}$ is unit vector along Z direction. The electric field surrounding the particle can be obtained by solving the LaPlace's equation,$\nabla^2\emptyset = 0$, where $\emptyset$ is electric potential and the corresponding electric field (E) is obtained using the relation $E = -\nabla\emptyset$ by applying the following boundary conditions: (a) $\hat{E}$ is continuous at the sphere surface and (b) the normal component of the electric displacement D

is also continuous. The resulting solution of electromagnetic field outside sphere, E_{out} [63] is given by,

$$E_{out}(x,y,z) = E_0\hat{z} - \alpha E_0\left[\frac{\hat{z}}{r^3} - \frac{3z}{r^5}(x\hat{x} + y\hat{y} + z\widehat{z})\right] \quad \textbf{(1.1)}$$

Where *x, y,* and *z* are cartesian coordinates; r is the radial distance; $\hat{x}$, $\hat{y}$ and $\hat{z}$ are unit vectors; and α is metal sphere polarizabilty defined as $\alpha = ga^3$, where a is the radius of the sphere. The value of g is expressed as $g = \frac{\varepsilon_i - \varepsilon_m}{\varepsilon_i + 2\varepsilon_m}$. From the expression of g, it is clear that maximum enhancement will occur when denominator of g approaches to zero. This implies that $\varepsilon_i + 2\varepsilon_m$ should tend to zero value. In case of NP dispersed in water, the dielectric function of water, $\varepsilon_m = 1.77$, and from $\varepsilon_i + 2\varepsilon_m$=0 relation, the condition become $\varepsilon_i = -2 \times 1.77 = -3.54$. From the plot of dielectric function of Au (Figure 1.3), it is easy to check that this condition leads to plasmon resonance at ~520 nm. Hence in the case of silver and gold NP, this condition is met in the visible region of the spectrum, which has important implications for surface-enhanced spectroscopy. The band position of LSPR strongly depends on the environment close to metal NP surface. In order to calculate the intensity of light being scattered or absorbed by spherical NP upon interaction with light, three cross sections are considered and these three cross sections are linked by simple relation $\sigma_{ext}(extinction) = \sigma_{abs}(absorption) + \sigma_{scatt}(scattering)$ which is applicable for metallic spherical nanoparticles. For small particles, mainly absorption factor plays major role than scattering as shown in Figure 1.6 [64]. From the Figure 1.6, it can be seen that 20 nm size of gold NP has no scattering and particle only absorb the radiation. Hence metal NP of smaller size are more useful for surface enhanced spectroscopy applications.

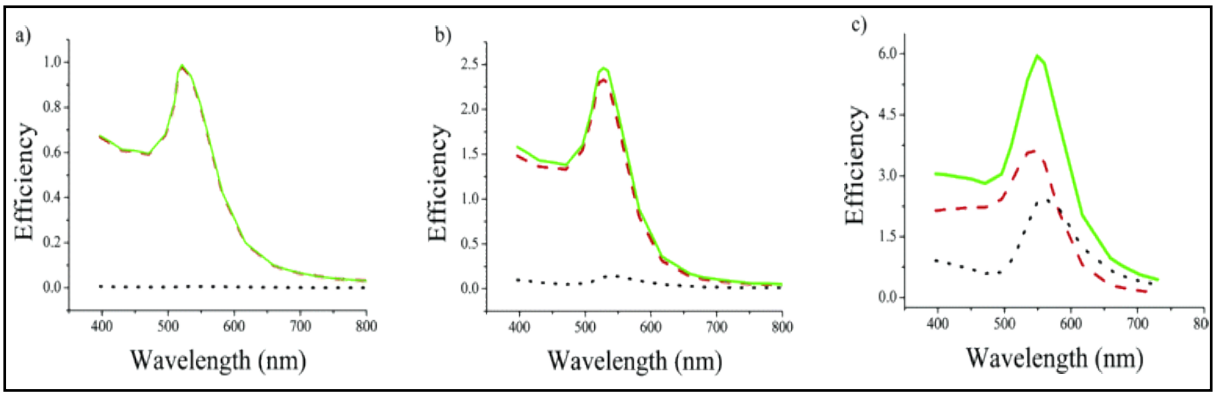

Figure 1.6. Calculated spectra of the efficiency of absorption Q_{abs} (red dashed), scattering Q_{sca}(black dotted), and extinction Q_{ext} (green solid) for gold nanospheres (a) D=20 nm, (b) D= 40 nm, (c) D=80 nm (Reproduced with the permission from Ref. [64]).

The extinction spectrum $\sigma_{ext}(\lambda)$ of metal sphere can be expressed as;

$$\sigma_{ext}(\lambda) = \frac{24\pi a^3 (\epsilon_m)^{3/2}}{\lambda} \frac{Im(\varepsilon_i)}{|\varepsilon_i + 2\varepsilon_m|^2} \qquad \textbf{(1.2)}$$

In comparison to chemical enhancement (discussed in subsequent section), higher electromagnetic SERS enhancements are possible because both the incident electric field ($E_{Laser}(\lambda)$) of the laser light and the scattered Raman $E_{Raman}(\lambda)$ are involved in interaction with the LSPR. The total SERS electromagnetic enhancement factor will be $|E_{Laser}|^2 |E_{Raman}|^2$. Therefore, the SERS enhancement can reach to the factor of approximately $E^4(\lambda)$ [48, 63, 65]. Furthermore, since the electric field strength varies according to relation $E(r) \sim \frac{1}{R^3}$, the SERS intensity will also be defined as $I_{SERS}(R) \sim \frac{1}{R^{12}}$, where R is distance from centre of NP to the adsorbate. Therefore, SERS can be considered as truly surface sensitive effect.

(B) CHEMICAL ENHANCEMENT MECHANISM

Several SERS spectral features could not be explained using electromagnetic theory alone. The chemical mechanism of SERS includes enhancements which are not due to plasmonic

sources. The chemical enhancement includes (a) ground state chemical enhancement that arises from chemical interactions between a molecule and NP, (b) resonance Raman enhancement that results when the excitation energy is in resonance with the molecular HOMO-LUMO transitions energy, (c) charge transfer effects which involves the photo induced transfer of an electron from the metal to an unoccupied molecular orbital of the adsorbate (LUMO) or vice versa as shown in Figure 1.7 [27, 66]. The chemical enhancement contribute up to 2 orders of magnitude in signal enhancement [14, 67] and is a short-range (<2 nm) effect [2, 48]. It is important to emphasize that all these enhancement mechanism are strongly dependent on LSPR excitation wavelength.

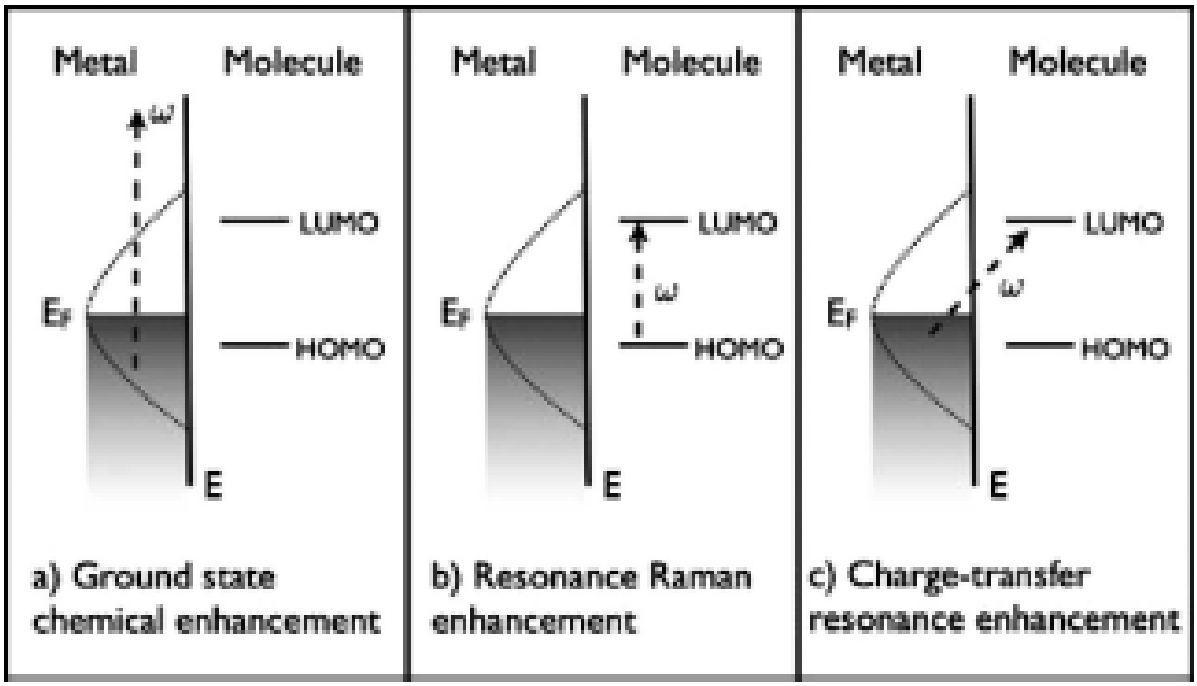

Figure 1.7. Illustration of the different types of chemical enhancement mechanism in SERS (Reproduced with the permission from Ref. [27]).

1.1.1.2. PLASMON-INDUCED CHEMICAL REACTION

In general, excitation of LSPR leads to a large enhancement in the localized EM field around the nanostructure surface which is exploited for the enhancement of Raman and IR signal of

adsorbate. In addition, localized surface plasmon could also initiate several chemical reactions of molecules adsorbed on the surface of metal nanostructures. Such reactions driven by excitation of LSPR are termed as plasmon-induced chemical reactions. The plasmon-driven chemical reactions lead to the formation of new molecules on the metal NP surface. The new molecules thus formed can be detected and identified by SERS from the appearance of its characteristic vibrational features. These plasmon-induced chemical reactions on the metal surfaces can provide a new opportunity for photochemical reactions driven by visible light. Plasmon-induced reactions have gained attention following the discoveries of two reactions. SERS studies of *p*-aminothiophenol (*p*ATP) and *p*-nitrothiophenol (*p*NTP) molecules adsorbed on silver metal NP surface, chemical transformation of the molecules to a new surface species dimercaptoazobenzene (DMAB) was identified by the spectral changes observed during SERS measurements [68, 69]. After this, there are several reports about plasmon-induced surface reactions on metal surface [70-78].

Upon illumination of metal nanostructures, the free electrons of a plasmonic nanostructure oscillate at the frequency of the incident light. When frequency of incident light matches with frequency of oscillation of surface electrons, the giant field is created near the surface. This phenomenon is called resonant excitation of localized surface plasmon resonance as explained in section 1.1.1.1. Following the excitation, localized surface plasmon can decay via radiative re-emission of photons or non-radiative generation of electron-hole pairs [79, 80].

The decay process of localized surface plasmon and the plasmon-induced chemical transformation of molecules adsorbed on metal surface via various excitation mechanisms are illustrated by Kazuma et al. [79] and shown in Figure 1.8 [79]. During the non-radiativley decay by landau damping of localized surface plasmon (1-10 fs), hot carrier (electrons and holes) are generated (Figure 1.8b) on the metal surface and finally heat dissipation to

surrounding medium (Figure 1.8c). The plasmon-induced chemical transformation of molecules is explained by various excitation mechanisms [79, 81-83]. These mechanisms are following: (1) direct intramolecular excitation mechanism, where the direct transition between the highest occupied molecular orbital (HOMO) and the lowest unoccupied molecular orbital (LUMO) of molecules take place resonantly with help of LSP resonance; (2) direct charge transfer mechanism where charge gets transferred from the metal to the LUMO of the molecule; (3) indirect hot-electron transfer mechanism wherein hot electrons

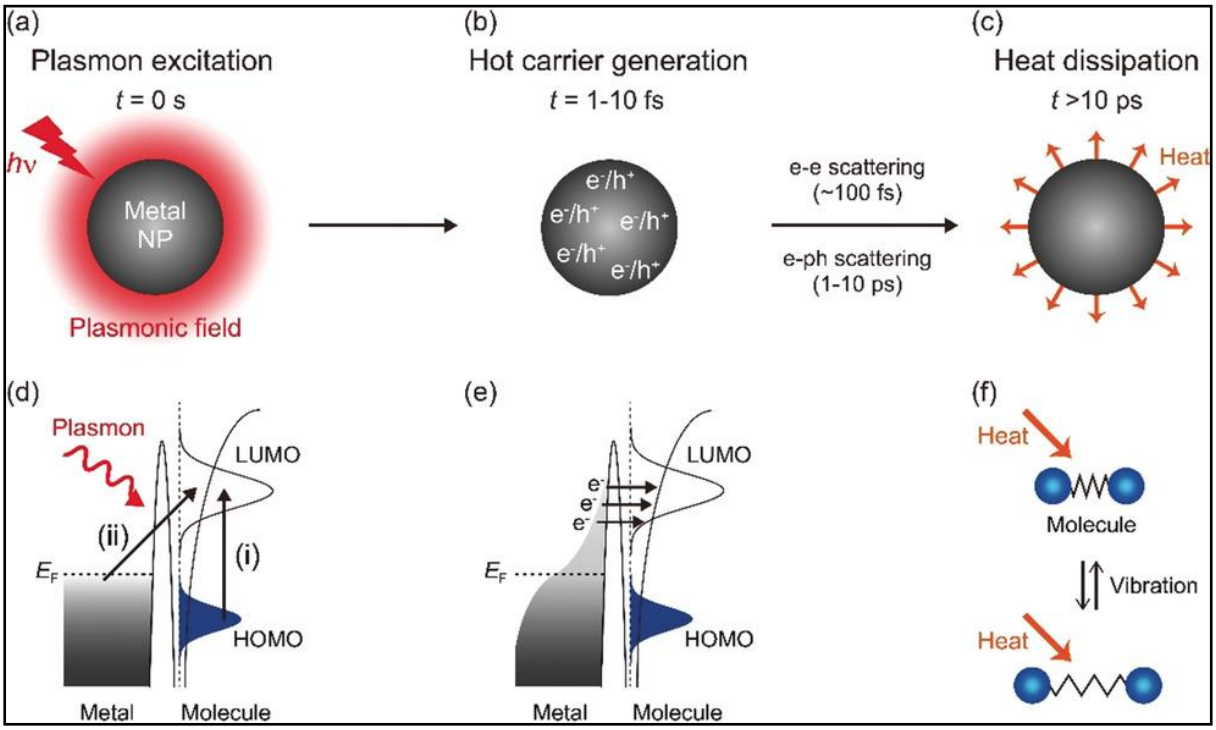

Figure 1.8. a) Excitation and b, c) decay processes of the LSP of a metal nanostructure. d–f) Excitation mechanisms of molecules adsorbed on the metal surfaces during the excitation and decay processes of the plasmon: d (i)) direct intramolecular excitation and (ii) charge transfer; e) indirect hot-electron transfer; f) local heating (Reproduced with permission from Ref. [79]).

are transferred from the metal to the molecule by an inelastic electron tunneling (IET) process, leading to the formation of a transient negative ion (TNI) state of the adsorbed molecule. The hot electron/holes (energetic charge carrier) are generated through non-

radiative decay of LSP resonance. The generated hot electrons lose their energy via electron–electron scattering until the electron gas approaches a nonequilibrium Fermi–Dirac distribution and carry energy ranging between E_f (Fermi level of metal) and $E_f + hv$ (photon energy) [84-87]. Figure 1.9 [84] represents the plot of calculated energy of the hot carriers generated by Ag NP with diameters of 15 nm when illuminated with 3.65 eV photon energy. Thus, high energy hot electrons are produced in the process even when the metal particle is

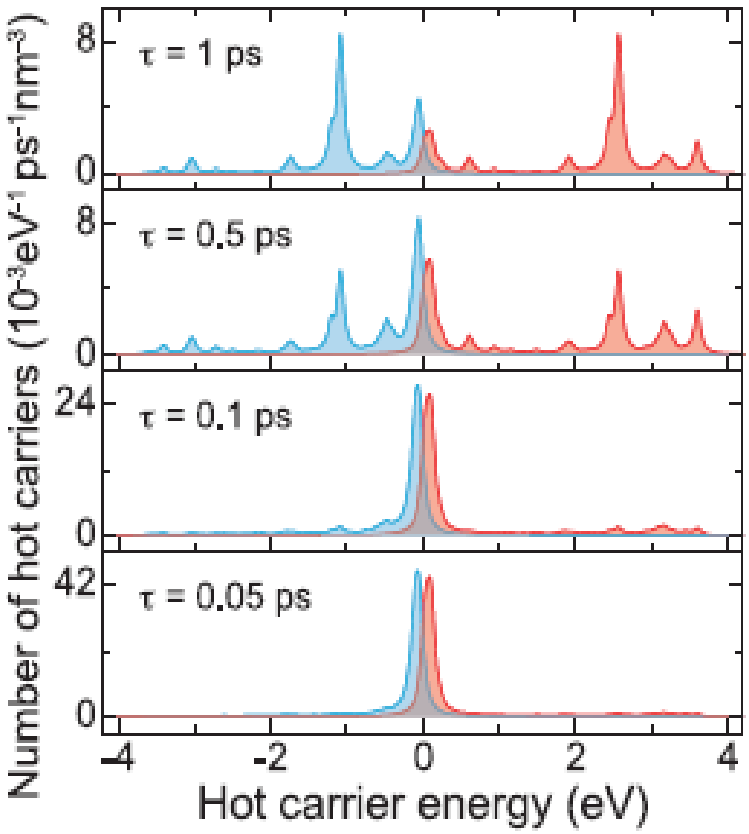

Figure 1.9. Hot carrier distributions per unit time and volume as a function of energy, calculated for a 15 nm diameter Ag nanoparticle. The generated hot-electrons (red line) and hot-holes (blue line) are plotted per unit of time and volume as a function of their energy with the Fermi level set at the zero energy (Reproduced with permission from Ref. [84]).

excited by relatively low energy photons. These hot electrons can trigger various chemical reactions in molecules adsorbed on metal NP by providing the energy to overcome the

reaction barrier. (4) Heat generated due to decay of the LSP resonance can also induce reactions in molecules. The application of plasmon-induced reaction is described in CHAPTER 4.

1.1.1.3. SURFACE SELECTION RULE

While SERS intensities are proportional to the fourth power of electric field, the vibrational mode symmetry and "surface selection rules" must also be taken into account to analyze and interpret and the SERS spectra [88]. "Surface selection rules" were conceptualized to explain why certain vibrational modes of molecule get selectively enhanced in SERS spectrum [55-59]. The observed SERS spectrum can be explained using these rules.

i. Molecules when adsorbed flat with respect to the metal surface, the out of plane bending modes are more enhanced and when adsorbed perpendicular direction, the inplane bending modes are more enhanced.
ii. Vibrations involving atoms that are close to the metal surface are more enhanced.
iii. For each adsorbate, there is optimum concentration at which maximum enhancement is obtained. This belongs to monolayer coverage of adsorbate. For other concentration, multilayer and bulk properties can manifest in the spectrum.

1.1.2. SURFACE ENHANCED INFRARED ABSORPTION (SEIRA) SPECTROSCOPY

After the discovery of SERS, Hartstein and co-workers [16] observed that the IR absorption of molecules get enhanced when they are adsorbed on thin metal surfaces and later the phenomenon was termed as SEIRA spectroscopy [12, 89, 90]. Although SEIRA has less enhancement factor that SERS, the higher IR absorption cross section makes it the promising and potential complementary tool to enhance IR signal of various types of molecules

adsorbed on metal nanostructure surfaces [12, 30, 89-92]. SEIRA based biosensors have been developed to detect various biological materials and antigens having biomedical and environmental importance [93]. The detection of protein monolayers [94] and the investigation of the chemical interaction between proteins with target antibodies [95] were carried out with help of SEIRA studies. It was also used for trace detection of fungicides which remain as contaminant in soil, water, food and applied in the analysis of environmentally hazardous chemicals in waste water [96].

Similar to SERS, electromagnetic along with chemical effects contribute to the total enhancement [91, 97]. In case of non-resonant interaction of light with metal nanostructures, the contribution of two electromagnetic mechanisms such as lightning rod effect and hybridized plasmon have been considered to explain the enhancement in IR absorption signal [25]. For almost all metals, especially in the mid-IR range, the dielectric function has a strong negative real part and its absolute value is larger than that of the imaginary part (Figure 1.3). Hence, in mid-IR range, where metals are essentially perfect conductor, the incident EM field cannot penetrate inside a metal and is instead condensed into the gap between two adjacent metal structures, called as the lightning rod effect. It is mainly associated with geometric factors of metallic structure in the IR regions where metals are perfect conductor [25]. The lighting rod effect phenomenon increases with decrease in frequency and the maximum field enhancement is observed over the IR region [98]. Additionally, the new dimer plasmon band can be formed in mid IR range due to the hybridization of two individual plasmons of two nearby metal nanostructures. Hybridization is occurred due to the coupling of individual plasmons of two very close metal nanostructures [99, 100]. This results in a red-shift of the plasmon band along with the generation of electromagnetic hot spots which depend upon the shape and separation distance of the nanostructures. Hence, the magnitude of the enhancement of SEIRA signal is found to be strongly dependent on the surface morphology

of the metal film that is the result of specific preparation conditions, such as substrate temperature, deposition rate, deposition time and substrate material [101-104].

SEIRA measurements have been carried out using a variety of geometries including attenuated total reflection (ATR) [16, 105-107], transmission [108-111] and external reflection [112, 113]. ATR-SEIRA studies are generally carried out using a thin metal film directly coated on the ATR crystal and the analyte molecules are deposited over the metal film. Physically evaporated metal island films deposited onto dielectric substrates (Silicon, ATR crystal, IR transparent window) have mostly been used as SEIRA active substrate for SEIRA measurements [16, 105, 108-110, 114, 115]. However, the production of metal thin films on dielectric substrates via physical evaporation methods is highly expensive and requires a large amount of target material. To overcome these issues, wet methods, electrochemical and chemical deposition can be taken into consideration for fabrication of metal film on substrates. However, the electrochemical deposition requires conducting substrates, whereas wet chemical deposition is free from this requirement. Hence, wet chemical deposition technique can be an alternate cheaper way to produce good quality metal thin films on transparent as well as non-transparent IR substrate for SEIRA studies. The use of wet chemically prepared Au NP films on dielectric Si substrates have been also explored in SEIRA spectroscopy in transmission mode [116, 117], but ATR-SEIRA studies using Au NP anchored on glass substrate has not been fully explored yet.

1.2. HIGH PRESSURE RAMAN SPECTROSCOPY

High pressure is among the most effective thermodynamical parameter to externally tune inter-atomic/intermolecular separations to study effect of molecular interactions. In particular, molecular solids are found to undergo structural transitions, conformational changes, isomerization and chemical transformations upon applying external pressure [118,

119]. Compression results in the increase in the free energy of the molecular system due to the reduction in the volume and inter-/intra-molecular distances. Consequently, the system becomes thermodynamically unstable and in response to achieve free energy minimum, number of possible processes, such as phase transformation, ionization, polymerization, amorphization, dissociation and metallization can occur [120-125]. The easily tuneable physical and chemical properties of materials on applying external pressure, gives us huge opportunities to exploit them for optical, electronic and biomedical applications purposes. Therefore, pressure serves as an excellent tool to produce novel materials starting from simple molecular solids, in particular molecules having conjugate ring structures or unsaturated bonds [126]. For example, upon compression, benzene, the simplest aromatic compound having conjugate ring structure, undergoes structural changes and polymerizes on release of pressure [122]. The formation of new compounds like crystalline and amorphous graphite materials by pressurizing benzene has been reported [122, 127]. In high pressure Raman studies of pyridine, several reversible phase transitions were observed up to 16 GPa followed by the chemical transformation, which were attributed to the destruction of the ring structure when compressed beyond 22 GPa [128]. Unsaturated hydrocarbons have also been considered for high pressure research due to varying reactivity of the ethylenic bonds under external pressures [121, 125]. Many unsaturated organic molecules with double and triple bonds have been transformed to different molecule by the application of pressure [123, 129]. Recently, owing to the high selectivity and high sensitivity of SERS technique, it has been coupled with high pressure Raman study to investigate the effect of pressure on adsorbates [130, 131], wherein the investigations were mainly focused on the effect of pressure on interaction mechanism such as charge transfer between metal and adsorbate, and also on the adsorbate Raman intensity. Probing and understanding the interaction mechanism between molecules and SERS substrates (metal NP) under high pressure might become complicated

due to combined effect of SERS and high pressure. Therefore, to understand the corresponding mechanisms, the high pressure study of molecules without SERS should be pursued first.

1.3. SCOPE OF THESIS

This thesis focuses on SEVS studies comprising of SERS and SEIRA studies of various biologically important molecules using plasmonic metal NP, particularly Ag and Au and their films deposited on dielectric substrate such as glass. The SERS/SEIRA studies aim to probe and analyze the biomolecules present at low number density with the help of unprecedented field enhancement, which arises due to LSPR excitation, and also to investigate the metal-adsorbate interfacial interaction and orientation of molecules on metal surfaces. This thesis also demonstrates the plasmon-induced chemical transformation of molecule adsorbed on Ag NP surface probed by surface sensitive SERS technique.

Additionally, as a futuristic goal of probing the interaction mechanism between molecule and SERS substrate under high pressure, we have carried out the high pressure Raman study of a selected molecule (also studied using SERS) and presented in this thesis. The molecule has been selected owing to its interesting molecular properties. This independent high pressure Raman study will be useful for SERS studies under high pressure in near future.

The short introductions about our aim of choosing the research problems are described below.

Identification and characterization of skin biomolecules based on vibrational spectral fingerprint is of great importance in dermatological research. Filaggrin protein is major source of amino acids (histidine) which is metabolized into hygroscopic derivatives such as trans-urocanic acid (t-UCA) on skin. The t-UCA, a UV chromophore molecule, is considered

as one of the natural moisturizing factor (NMF) present in the upper most layers (4-34 nM/cm^2) of the human skin and known to play an important role in skin hydration and UV protection [132, 133]. The reduced level of NMF can lead to various skin disorder such as Atopic Dermatitis [134]. Hence, owing to its interesting properties, t-UCA continues to be the subject of intense research. Spectroscopic information of NMF at physiological concentration can be used as a reliable biomarker for skin diagnostics and research purposes. The need of spectroscopic information addressing the above issue has motivated us to do SERS based study of t-UCA at physiological concentration in vitro phase, which is presented and described in this dissertation.

The presence of imidazole ring/acrylic acid in the t-UCA molecular structure and π electrons of acrylic ethylenic bond makes it an interesting compound for studying under compression. Therefore, due to its interesting molecular properties, we have chosen this molecule to carry out the high pressure Raman investigation and presented in this thesis.

The application of giant EM field enhancement due to excitation of LSPR results in detection of extreme low concentration of molecules. However, it may also initiate several chemical reactions on metal surface as discussed in section 1.1.1.2. Thiazolidine-2, 4-dione (TZD) and its derivatives are important pharmacological heterocyclic compounds [135-140]. TZD acts as an inhibitor of corrosion of mild steels in acidic solution and is also used as a brightener in the electroplating industry due to its ability to make chemical coordination with the metal surface [141, 142]. Due to presence of active methylene group, TZD is known to undergo conventional Knoevenagel condensation reactions with aldehydes and ketones, resulting in the formation of unsaturated ketonic products [143]. Hence, we chose to study SERS on TZD to investigate if a similar type of reaction can occur on the surface of Ag NP induced by plasmon, which would be helpful in extending the research related to plasmon-

driven reactions for the development of novel approach in organic synthesis. The thesis also describes the plasmon induced chemical reaction of TZD adsorbed on Ag NP surface.

SEIRA studies of few biologically relevant molecules like taurine (sulphur containing amino acid), sodium benzoate (food preservative) and uracil (RNA base) deposited on wet chemically prepared Au NP films on glass substrate are described in this thesis. As discussed in introduction, physically evaporated metal island films onto dielectric substrates (mostly IR transparent material) have mostly been used for SEIRA spectroscopy [16, 105, 108, 114, 115]. However, the production of thin films via physical evaporation methods is highly expensive and requires a large amount of material target. To overcome these issues, wet chemical deposition methods can be taken into consideration for fabrication of metal film substrates. Hence, SEIRA studies were carried out using wet chemically prepared Au NP film deposited on glass substrate (IR opaque) and presented in this thesis. The morphological impact of Au NP film on SEIRA signal is also studied and described here.

A thorough report of our results and their interpretations are documented in this thesis in various chapters. We believe that the presented results obtained from our studies will be useful to various applications.

1.4. STRUCTURE OF THE THESIS

The Structure and layout of this thesis is as follows:

CHAPTER 2 describes the basic theory of vibrational spectroscopy including IR absorption and Raman scattering together with experimental methodologies employed in SEVS and high pressure Raman studies. In methodologies, basic principles of Raman scattering set up, Fourier transform infrared spectrometer (FTIR), Attenuated total internal (ATR) reflection, UV-visible spectrophotometer, Atomic force microscopy (AFM),

Moissanite anvil cell (MAC), Ruby fluorescence calibration method and density functional theory are described.

The first section (3.1) of CHAPTER 3 deals with the SERS study of skin chromophore molecule, t-UCA adsorbed on Ag NP and its detection below the physiological concentration. This chapter also provides the details about the interaction of t-UCA with Ag NP and its orientation on Ag NP surface as a function of number density of t-UCA molecules. The high pressure Raman investigation of t-UCA is also described in second section (3.2) of this chapter.

In CHAPTER 4, another aspect of LSPR i.e. plasmon induced reaction on metal surface is described. The chapter deals with the plasmon induced formation of TZD dimer from TZD molecules adsorbed on Ag NP as probed by SERS study. The mechanism of dimer formation via plausible transfer of hot-electron on Ag NP is described.

CHAPTER 5 deals with SEIRA studies of few important biomolecules adsorbed on wet-chemically prepared Au NP film immobilized on silanised glass substrate using ATR–FTIR. In the first section of this chapter, the SEIRA studies of sodium benzoate and taurine using ATR-FTIR technique and the presence of both chemisorbed and physisorbed layers of both sodium benzoate and taurine on the Au NP film are described. In the second part, the deposition time dependent evolution of morphological changes in Au NP films and its influence on the SEIRA spectra of uracil (RNA base) is discussed.

Finally, CHAPTER 6 summarizes the general conclusions of the thesis and outlines the future scope.

CHAPTER 2.

THEORY AND EXPERIMENTAL METHODS

2.1. THEORY OF VIBRATIONAL SPECTROSCOPY

Spectroscopy is the study of interaction of matter with EM radiation. In vibrational spectroscopy, molecule is vibrationally excited by the EM radiation which results in the absorption of EM radiation at the infrared range (IR) or gives rise to Raman scattering when illuminated by laser. IR and Raman spectra result from transitions between quantized vibrational energy states. Molecular vibrations can arise from the simple coupled motion of the two atoms of a diatomic molecule to the more complex motion of every atom in a large polyatomic molecule. The N atomic system will have 3N degrees of freedom, three of which represent translational motion and three represent rotational motion about the x, y, and z axes. The remaining 3N-6 (or 3N-5for a linear molecule) degrees of freedom give the number of ways that the atoms in the molecule can vibrate, which will represent the total number of vibrational modes in the molecule. The energy of vibrational levels E_v of a diatomic molecule, considering the harmonic oscillator approximation, are given by

$$E_v = h\nu \left(v + \frac{1}{2}\right) \quad \textbf{(2.1)}$$

Where, v is vibrational quantum number, v = 0, 1, 2, 3….. The classical vibrational frequency ν is related to reduced mass μ ($m_1 \times m_2/m_1+m_2$) of the atoms and force constant of bond by the equation,

$$\nu = \frac{1}{2\pi}\sqrt{\left(\frac{k}{\mu}\right)} \quad \textbf{(2.2)}$$

In terms of wave number, the equation 2.2 can be rewritten as,

$$\frac{E_v}{hc} = G_v = \omega \left(v + \frac{1}{2}\right) \quad \textbf{(2.3)}$$

Figure 2.1 shows the potential function and energy levels for harmonic and anharmonic oscillator.

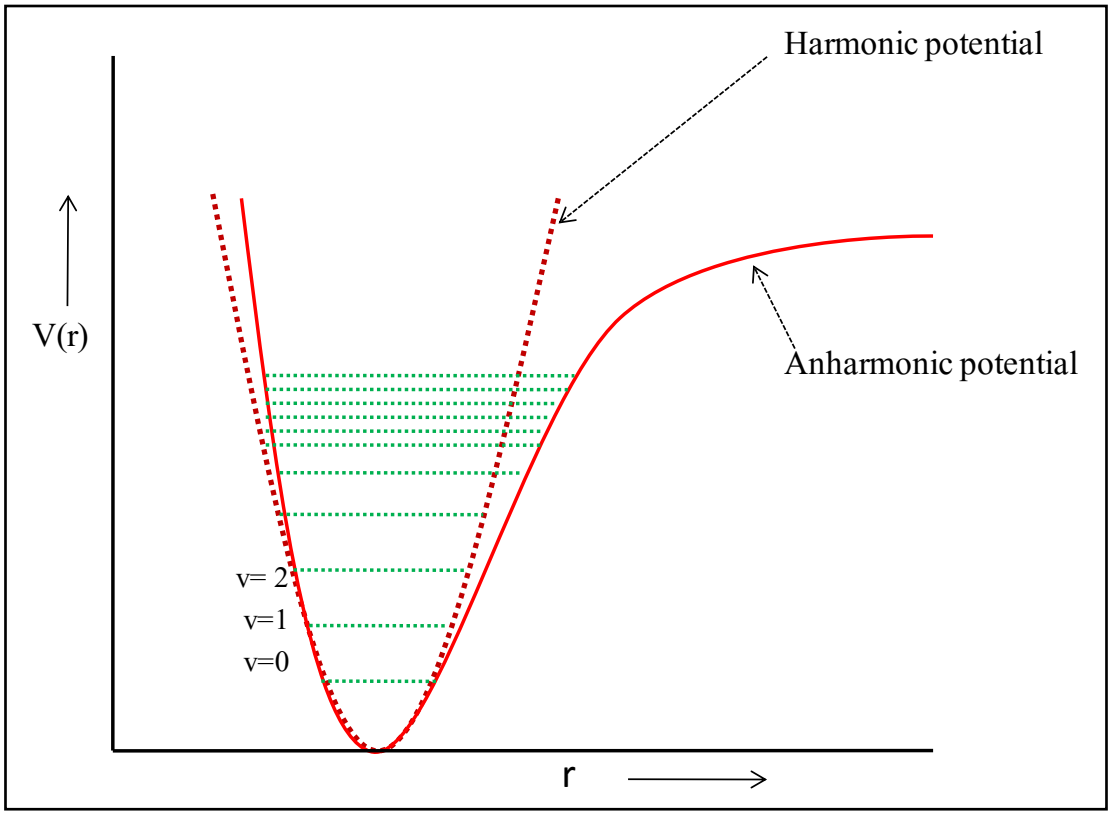

Figure 2.1. Potential energy of a diatomic molecule as a function of the atomic displacement during a vibration of a harmonic oscillator (broken line) and an anharmonic oscillator (solid line).

The parabolic potential well in Figure 2.1 (broken line) is actually a poor representation of the force felt by diatomic molecules. A real molecule has asymmetric potential as inter atomic distance increases the molecule dissociate which can be explained by anharmonic potential Figure 2.1 (solid line) and defined by Morse potential function. The energy level is defined by,

$$G_v = \omega_e \left(v + \frac{1}{2}\right) - \omega_e x_e \left(v + \frac{1}{2}\right)^2 \qquad \textbf{(2.4)}$$

2.2. VIBRATIONAL SPECTROSCOPIC TECHNIQUES

The two main techniques, Raman and IR absorption spectroscopy, are used to acquire vibrational spectra of molecules whose physical mechanisms are discussed below.

2.2.1. INFRARED ABSORPTION

Molecular vibration typically lies in the mid infrared range (200-4000 cm^{-1}) and can be probed using IR absorption spectroscopy. Molecule is excited from lower vibrational to higher vibrational state by IR light and subsequently absorption spectrum can be obtained. The transition moment for a transition between lower and upper state with vibrational wave functions ψ''_v and ψ'_v respectively is given by [3],

$$R_v = \int \psi_v'^{*}\, \mu \psi_v'' dx \qquad \textbf{(2.5)}$$

Where, x is ($r-r_e$), the displacement of the internuclear distance from equilibrium. The dipole moment μ is zero for a homonuclear diatomic molecule, resulting in $R_v = 0$ and all vibrational transitions being forbidden. For a heteronuclear diatomic molecule μ is non-zero and varies with x and the variation in μ can be expressed as a Taylor series expansion,

$$\mu = \mu_e + \left(\frac{d\mu}{dx}\right)_e x + \frac{1}{2!}\left(\frac{d^2\mu}{dx^2}\right)_e x^2 + \cdots \qquad \textbf{(2.6)}$$

where the subscript ‘e’ denotes the equilibrium configuration. The transition moment equation now becomes

$$R_v = \mu_e \int \psi_v'^{*}\, \psi_v'' dx + \left(\frac{d\mu}{dx}\right)_e \int \psi_v'^{*}\, x\, \psi_v'' dx + \cdots \qquad \textbf{(2.7)}$$

$\psi_v^{'}$ and $\psi_v^{''}$ are the orthogonal eigenfunctions of the same Hamiltonian, it means that, when $v^{'} \neq v^{''}$,

$$\int \psi_v^{'*} \psi_v^{''} dx = 0 \qquad \textbf{(2.8)}$$

Equation (2.7) then becomes

$$R_v = \left(\frac{d\mu}{dx}\right)_e \int \psi_v^{'*} x \psi_v^{''} dx + \cdots \qquad \textbf{(2.9)}$$

The first term of this equation is non–zero if $\Delta v = \mp 1$. This constitutes the vibrational selection rule [3] and also the change in dipole moment must be nonzero for vibrational mode to be IR active.

2.2.2. RAMAN SCATTERING

The Raman scattering process between a photon and a molecule is an important and ubiquitous spectroscopic technique for studying the vibrational modes of molecules. In Raman scattering, the sample is irradiated with monochromatic light ($h\nu_0$) in visible or UV range and scattered light are observed. The scattered light consists of two types of scattered photons: one is called Rayleigh scattering having same frequency as incident light (ν_0), and other called as Raman scattering (inelastic scattering) having photons of $\nu_0 \pm \nu_M$ frequencies.

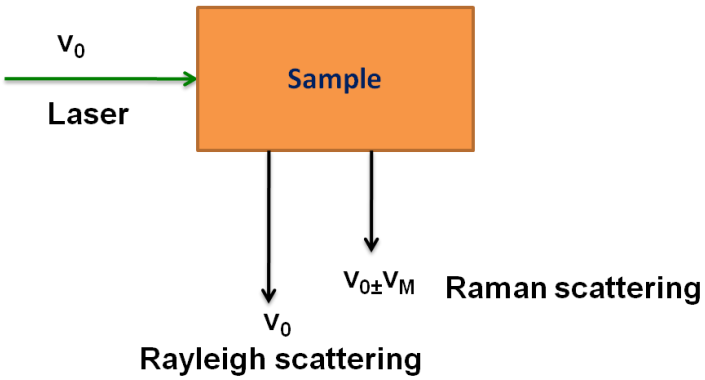

Figure 2.2. Raman scattering process.

Raman scattering is very weak (~10^{-5} of incident photons) phenomenon and scattered photons contain the $\nu_0 \pm \nu_M$ frequencies, where ν_M is vibrational frequency of molecule. The schematic of Raman process is shown in Figure 2.2. The $\nu_0 - \nu_M$ and $\nu_0 + \nu_M$ scattered light are termed as stokes and anti-stokes lines respectively. In Raman spectroscopy, the vibrational frequencies are measured as a shift from the incident laser frequency (ν_0). Raman scattering is illustrated schematically in Figure 2.3.

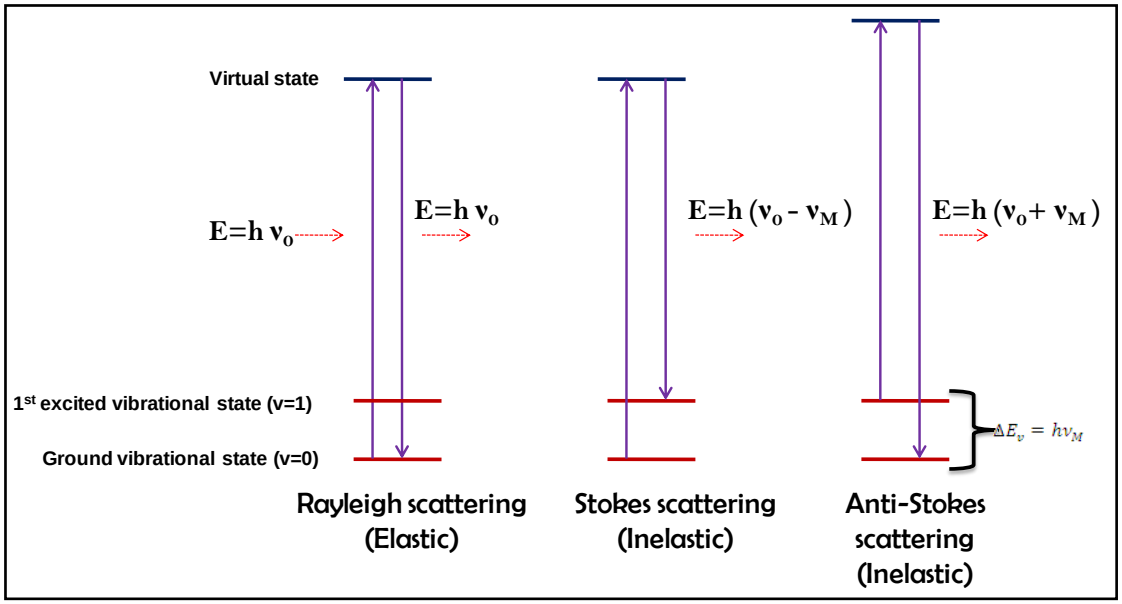

Figure 2.3. Schematic diagram of Raman scattering.

According to classical theory, Raman scattering can be explained as follows: The electric field strength (E) of an electromagnetic wave (laser) of frequency ν_0 is given by,

$$E = E_0 \cos 2\pi\nu_0 t \qquad \textbf{(2.10)}$$

where E_0 is the amplitude of the laser. If a diatomic molecule is irradiated with laser, an electric dipole moment P is induced and given by the equation,

$$P = \alpha E = \alpha E_0 \cos 2\pi\nu_0 t \qquad \textbf{(2.11)}$$

Where, the proportionality constant α, is called polarizability. If the molecule is vibrating with a frequency v_M, the nuclear displacement q can be expressed as,

$$q = q_0 \cos 2\pi v_M t \tag{2.12}$$

Where, q_0 is the vibrational amplitude. For small amplitude of vibration, α is a linear function of q. Thus,

$$\alpha = \alpha_0 + (\partial\alpha/\partial q)_0 q + \cdots \tag{2.13}$$

Here, α_0 is the polarizability at the equilibrium position, combining the equations (2.11), (2.13) and (2.12), we get

$$P = \alpha E_0 \cos 2\pi v_0 t$$

$$= \alpha_0 E_0 \cos 2\pi v_0 t + \left(\frac{\partial\alpha}{\partial q}\right)_0 q E_0 \cos 2\pi v_0 t$$

$$= \alpha_0 E_0 \cos 2\pi v_0 t + \left(\frac{\partial\alpha}{\partial q}\right)_0 q_0 E_0 (\cos 2\pi v_M t)(\cos 2\pi v_0 t)$$

$$= \alpha_0 E_0 \cos 2\pi v_0 t + \frac{1}{2}\left(\frac{\partial\alpha}{\partial q}\right)_0 q_0 E_0 [\cos\{2\pi(v_0 + v_M)t\} + \cos\{2\pi(v_0 - v_M)t\}] \tag{2.14}$$

According to classical theory, the first term is due to oscillating dipole radiating light of frequency v_0 (Rayleigh scattering), second terms correspond to Raman scattering of frequency $v_0 + v_M$ (Anti-stokes) and $v_0 - v_M$ (Stokes). If $\left(\frac{\partial\alpha}{\partial q}\right)_0$ is zero, the vibration will be Raman inactive. Hence, to be Raman active vibrational mode, the rate of change of polarizabilty with the vibration must be nonzero.

2.3. EXPERIMENTAL METHODS FOR SEVS STUDIES

2.3.1. RAMAN INSTRUMENT FOR SERS STUDIES

The schematic representation of the charged coupled device (CCD) based Raman spectrometer employed for SERS studies is given in Figure 2.4. It consists of a diode pumped Nd^{3+}: YAG laser, lens L_1 to focus the laser beam onto the sample, collection optics L_2, a home-built 0.9 m single stage monochromator [144], a super notch filter, and a Peltier-cooled CCD (Andor Technology). Raman spectra were excited using 532 nm line of the solid state laser with power of 15 mW. The scattered light is collected by lens L_2 and analysed using the single stage monochromator coupled with a super-notch filter and detected by a Peltier-cooled CCD (1024×256 pixels). Raman scattered light is collected using back-scattered geometry (180°) and is focused onto the entrance slit of the monochromator.

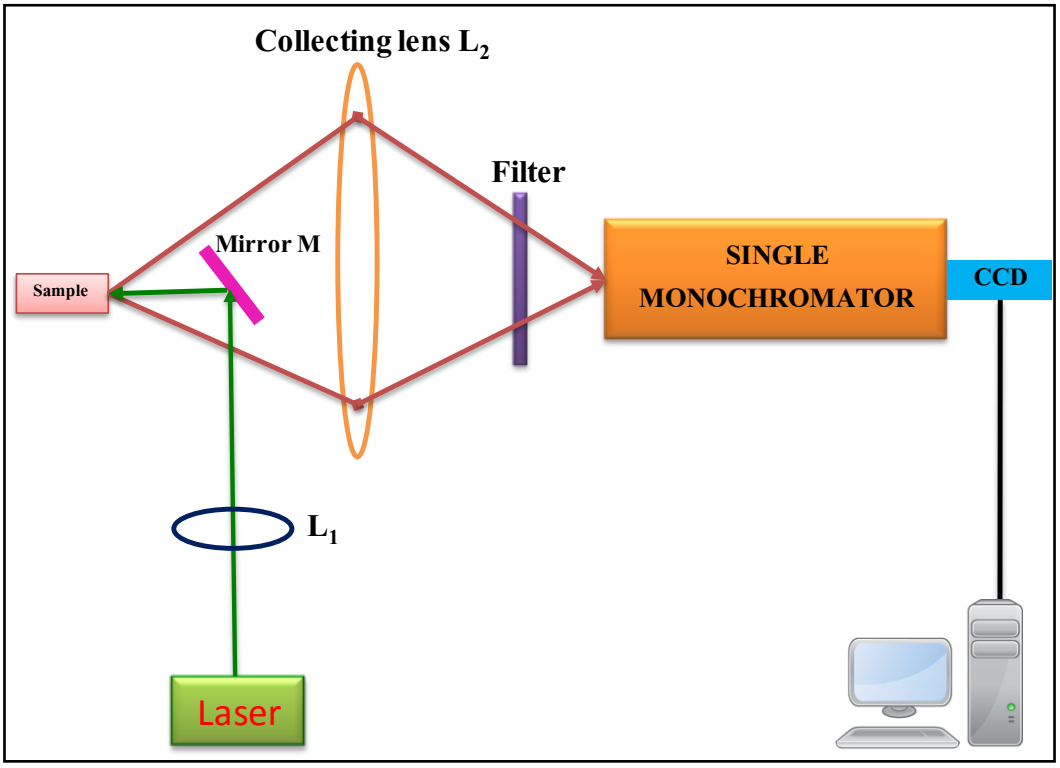

Figure 2.4. Schematic of single stage monochromator Raman set up.

2.3.2. FOURIER TRANSFORM INFRARED SPECTROMETER (FTIR) FOR ATR-SEIRA STUDIES

IR/SEIRA measurements have been carried out by using Bruker vertex 80 V Fourier transform infrared (FTIR) spectrometer. The schematics depicting the optical configuration of the Bruker 80V FTIR is shown in Figure 2.5. In FTIR instrument, two-beam Michelson interferometer is considered to be the heart of the instrument [145]. The purpose of the Michelson interferometer is to divide a beam of radiation into two paths and then recombine these two beams after the path difference that has been introduced. The variation of intensity of the beam coming from the interferometer is recorded as function of path difference by the detector. This is called as an interferogram. The spectrum is obtained by converting the interferogram signal into frequency domain using a mathematical operation, Fourier transformation. The simplest form of the optical diagram of Michelson interferometer used in FTIR is depicted in Figure 2.6. It consists of two mutually perpendicular plane mirrors (M_1 & M_2). At the intersection of these two mirrors, a beamsplitter is placed, which is designed to transmit 50% of the radiation that impinges upon it, and reflect the other 50%. As a result, the light transmitted by the beamsplitter strikes the fixed mirror (M2), and the light reflected by the beamsplitter strikes the moving mirror (M1). After reflecting off their respective mirrors, the two light beams recombine at the beamsplitter, and then leave the interferometer to interact with the sample and strike the detector. In Michelson interferometer an optical path difference (δ) is introduced between the two beams by translating the moving mirror away from the beamsplitter. If the δ between the two mirrors is varied by moving the mirrors, a detector would see alternate maxima and minima of intensity as a function of δ.

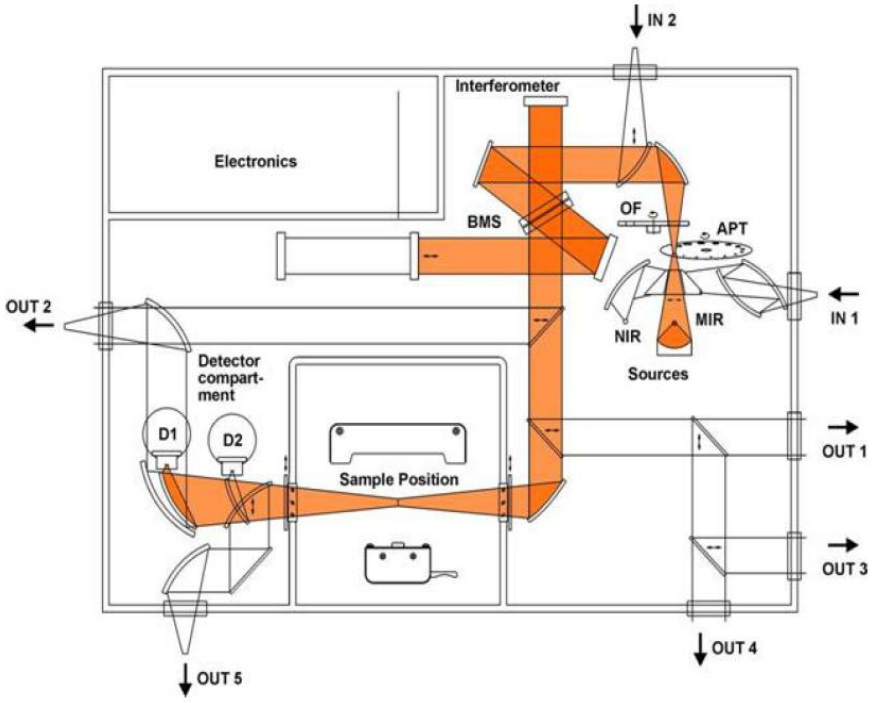

Figure 2.5. Optical layout of commercial Bruker FTIR (Figure taken from https://www.bruker.com/products/infrared-near-infrared-and-raman-spectroscopy/ft-ir-research-spectrometers/vertex-series/vertex-8080v/learn-more.html).

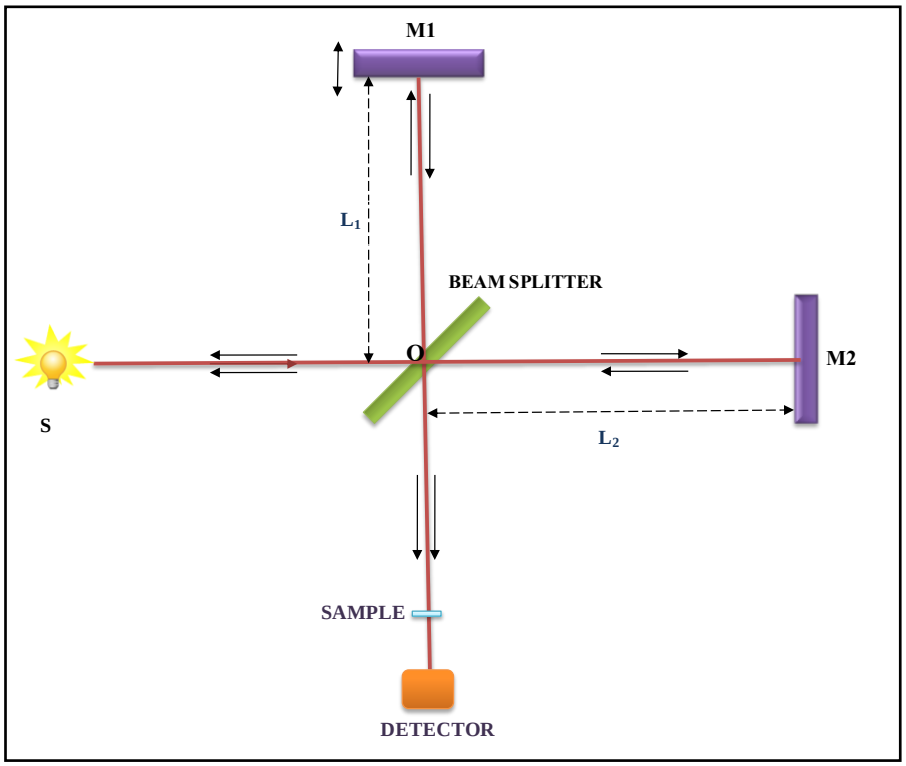

Figure 2.6. Optical layout of Michelson interferometer in FTIR.

In Fourier transform spectroscopy, the fundamental quantity measured is the interferogram [4]. For a continuous broad band source, the measured interferogram turns out to be the Fourier transform of the frequency spectrum. Hence, spectrum can be extracted by performing an inverse Fourier transform on the interferogram and mathematically this can be expressed as,

$$B(\omega) = 2\int_0^{\infty} I(\delta)\, e^{-2\pi i\omega\delta}\, d\delta \qquad \textbf{(2.15)}$$

where $B(\omega)$ is the power spectrum of the source in terms of the wavenumber ω ($incm^{-1}$), $I(\delta)$ is the measured interferogram or signal detected at an optical path difference of $\delta\ (cm) = 2(OM_1 - OM_2)$. The interfreogram of He-Ne laser is used to obtain the optical path difference. The resolution (R) of the FTIR instrument is defined by $R = \frac{1}{\delta_{max}}$, where δ_{max} is the maximum optical path difference. There are various advantages of FTIR over the grating based instruments and these are:

a) Throughput (Jacquinot) advantage: Maximum power reaches to detector (no slit)
b) Multiplexing (Fellgett's) advantage): All wavelengths are recorded simultaneously.
c) Connes advantage: Interferogram is sampled correctly with respect to the laser reference interferogram, hence spectrum is calibrated internally.
d) Stray Light Advantage: The detector is sensitive only to modulated frequency given by$f = 2v\omega$; where f is the modulated frequency, v is the velocity of the moving mirror and ω is the wavenumber.

Various components and parameters used in FTIR measurements in mid IR range (400-4000 cm^{-1}) are given below:

a) Source: Globar (SiC)
b) Detectors: LN_2 cooled HgCdTe and DTGS
c) Beamsplitters: KBr and CaF_2

2.3.3. ATTENUATED TOTAL REFLECTION (ATR)

ATR coupled with FTIR is the most widely used technique in IR absorption spectroscopy. This technique has the ability to record the spectrum of various kinds of samples such as solid, liquid and thin films. Moreover, it is also able to probe the monolayer or multiple layers of adsorbate deposited on to various types of substrates. Its operation is based on basic principle of total internal reflection. Total internal reflection in any optical system occurs when angle of incidence of beam is greater than critical angle (the angle of incidence that provides an angle of refraction of 90^o). The material that exhibits the total internal reflection is known as an internal reflection element (IRE). In ATR technique, sample is placed in contact with IRE element, and absorption spectrum is recorded as a result of that contact. The working principle of ATR crystal is shown in Figure 2.7. As seen from the Figure 2.7, an infrared beam is directed onto an IRE crystal at a certain angle (greater than critical angle) and the internal reflectance creates an evanescent wave that extends beyond the surface of the crystal into the sample held in contact with the crystal. This evanescent wave protrudes only a few microns beyond the crystal surface and into the sample. In spectral regions of the IR spectrum where the sample absorbs energy, the evanescent wave will be attenuated or altered. The attenuated energy from each evanescent wave is passed back to the IR beam, which then exits the opposite end of the crystal and is passed to the detector in the IR spectrometer and consequently IR spectrum is generated. The depth (d_p) to which the sample is probed is defined as the distance required for the electric field amplitude to fall to e^{-1} of its value at the surface of IRE crystal and is further defined by,

$$d_p = \frac{\lambda}{2\pi(n_1^2 sin^2\theta - n_2^2)^{\frac{1}{2}}} \qquad \textbf{(2.16)}$$

Where λ is the wavelength of light, θ is the angle of incidence of the IR beam relative to a perpendicular from the surface of the crystal and n_2, n_1 are the refractive index of the sample

and crystal respectively. Typical depth of penetration in ATR ranges from about 0.5 microns to about 5 microns depending upon the experimental conditions. For ATR-SEIRA studies, ZnSe IRE crystal (650-20000 cm^{-1}) having 1.66 μm penetration depth (d_p) was employed for ATR-FTIR measurements. The image of ATR accessories are shown in Figure 2.8.

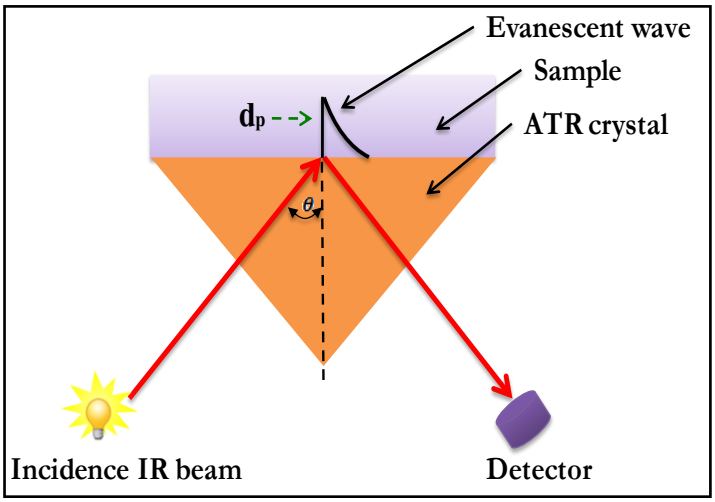

Figure 2.7. ATR working principle.

.

Figure 2.8. ATR accessories.

2.3.4. PREPARATION OF SILVER AND GOLD NANOPARTICLES

2.3.4.1. SILVER NANOPARTICLES

Ag is more frequently and commonly used plasmonic metal for SERS experiments. For SERS studies, the aqueous Ag sol (Ag NP) was prepared by simple reduction of $AgNO_3$ according to method reported by Creighton et. al. [146]. In the typical procedure, $AgNO_3$ was reduced by adding 10 ml of 10^{-3}M $AgNO_3$ drop wise to 30 ml of 2×10^{-3}M $NaBH_4$ solution kept in ice-cold temperature. The mixture was stirred vigorously during preparation to get mono dispersed NP. The resulting Ag NP were characterized by recording the LSPR absorption band using UV-Visible absorption spectroscopy and their size was determined with the help of transmission electron microscopy (details are given in section 4.4.1).

2.3.4.2. GOLD NANOPARTICLES

For the preparation of Au NP films on to glass substrate for SEIRA spectroscopy, an aqueous Au sol (Au NP) prepared by citrate reduction method by Turkevich et. al.[147] was used. This method produces monodisperse spherical Au NP of around 10-20 nm in diameter. In this method, $HAuCL_4$ aqueous solution (chlorauric acid) was heated up to boiling with vigorous stirring. To this 1% of sodium citrate aqueous solution was added. The solution remained clear for 15 seconds then suddenly dark wine red solution of Au NP was obtained which does not change its colour on further boiling. The prepared Au NP sol was used to make Au NP films on glass substrates for SEIRA studies.

2.3.5. CHARACTERIZATION TECHNIQUES

2.3.5.1. UV-VISIBLE ABSORPTION SPECTROSCOPY

Ag NP sol and Ag NP sol mixed with analyte molecules were characterized using a UV-visible absorption spectrophotometer. The schematic of double beam spectrophotometer is shown in Figure 2.9. The basic UV- visible spectrophotometer consists of light sources, sample holders, monochromator to separate the different wavelengths of light, and a detector. In a double-beam spectrophotometer, the light is split into two beams by beam splitter. One beam is used as the reference and the other part of beam is allowed to interact with sample of our interest. The absorption spectrum is calculated by taking the ratio of intensity obtained for sample (I) and reference (I_0).

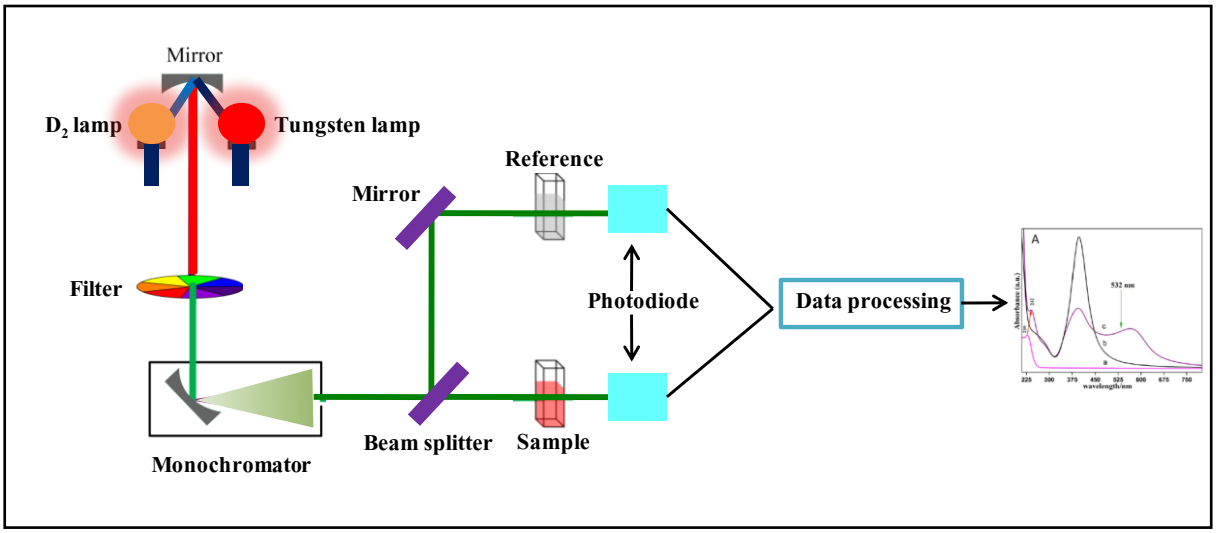

Figure 2.9. Schematic of UV-visible absorption set up.

2.3.5.2. ATOMIC FORCE MICROSCOPY (AFM)

AFM utilizes the Vander Waals forces between probe and test sample to measure surface morphology. It renders morphological images of a rather smooth surface with nano-metric spatial resolution. It is generally used to measure surface roughness, adhesion, viscoelasticity,

spreading resistance, indentation modulus etc. Fabricated Au NP films for SEIRA studies (CHAPTER 5) in present thesis were characterized by NT-MDT make Solver P-47H multimode ambient based AFM. The Si cantilever with spring constant of 6 N/m and resonant frequency of 135 kHz was employed for scanning all the samples to keep parity in the measurement. Figure 2.10 represents the schematic of an AFM.

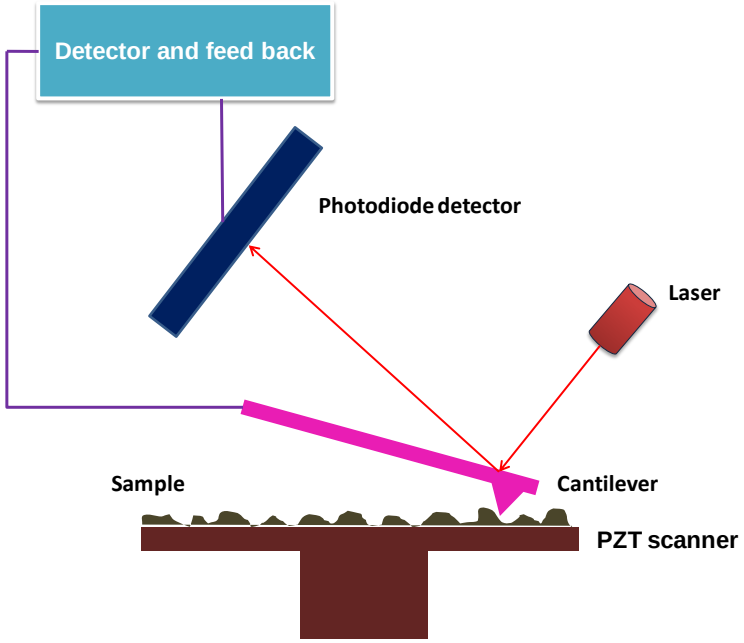

Figure 2.10. Schematic of an AFM instrument.

AFM can be operated in three different modes; contact mode, tapping mode and non-contact mode. Tapping mode being the most versatile and artifact free, was employed for surface scanning of Au NP films. In this mode, cantilever is made oscillating near its resonance frequency excited by suitable piezo-driver. In free resonance condition at suitable oscillating amplitude, the frequency just above the resonance is locked with the help of a lock-in amplifier. As the probe approaches in the close proximity (tens of nanometer) of sample, various forces viz., elastic, adhesion, electrostatic etc., between tip and test surface come into effect. Amplitude of oscillating cantilever as measured by position sensitive photo diode, starts decreasing with the decrease in tip-sample distance. The approach is stopped automatically at a predefined magnitude of oscillation of cantilever and probe is scanned over

the test surface in constant force mode. In constant force mode, tip-sample distance is kept constant. This is achieved by employing a feedback mechanism which generates error data with the help of deflection feedback from position sensitive photo-diode. To maintain distance tip-test surface at different points fixed while scanning, the whole scanner moves up and down depending on the error function. The movement of scanner gives the surface image of the sample.

Various parameters such as average roughness, Root mean square (RMS) roughness, peak to peak height, ten points height of Au NP films used in SEIRA studies have been calculated from AFM images. The average roughness is the arithmetic mean of the absolute values of the height of the surface profile calculated over the entire measured area. RMS roughness is the square root of the distribution of surface height and is considered to be more sensitive than the average roughness. Peak to peak height is the vertical distance between the highest and lowest points in the area and describes the overall roughness of the surface. Ten-points height is the difference in height between the average of five highest peaks and five lowest valleys in the measured surface [148].

2.4. EXPERIMENTAL METHODS FOR HIGH PRESSURE STUDY

2.4.1. CONFOCAL MICRO-RAMAN INSTRUMENT

High pressure Raman studies were carried out using triple stage Raman spectrometer (HORIBA JobinYvon's T64000). The Raman signal is excited using 514.5 nm laser generated from Ar+ laser. The optical layout of the triple stage Raman spectrometer is shown in Figure 2.11. The scattered radiation from the sample is passed through the double pre-monochromator stage acting as tuneable band pass filter. The first monochromator disperses the radiation and the second monochromator converge the radiation which then passes

through the third monochromator and is dispersed again. This mode of collecting the radiation is known as subtractive mode configuration. The advantage of this configuration is that it can measure very low frequencies close to the laser wavelength (< 5 cm^{-1}) regardless of wavelength of the laser used. The dispersed radiation from the third monochromator is collected and detected by the peltier cooled CCD detector.

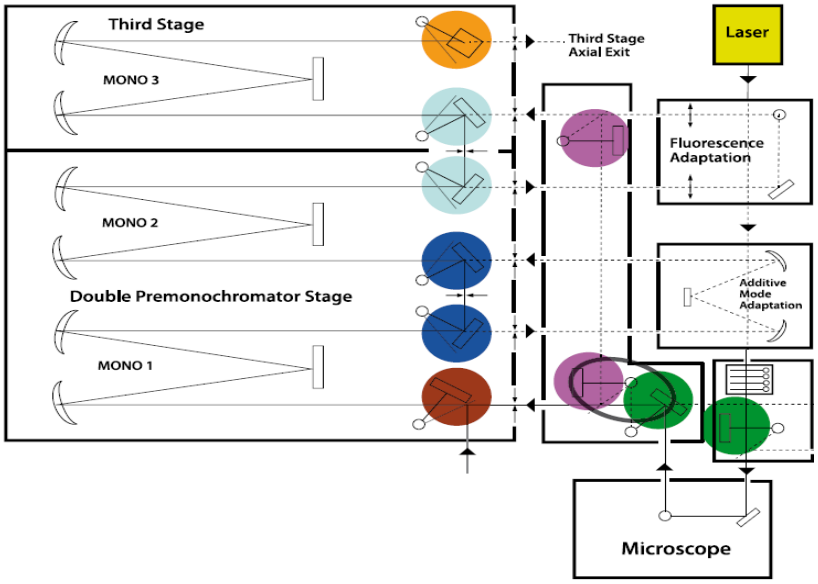

Figure 2.11. Optical layout of confocal Raman instrument (Figure taken from: http://www.horiba.com/fileadmin/uploads/Scientific/Documents/Raman/T64000.pdf).

2.4.2. HIGH PRESSURE TECHNIQUE

The hydrostatic pressure on molecular systems can be applied by employing the anvil cell. Diamond and Moissanite anvil cell are the most frequently used for above application. Moissanite is hexagonal silicon carbide. Since, the vibrational spectroscopy is consider to be the most effective method to probe the behavior of molecular solids under high pressure, optical transparency is the key factor in selecting the materials for generating the pressure. All diamonds have the intense first order Raman line at 1332 cm^{-1} (F_{2g} mode) [149], whereas

the Moissanite is transparent in this spectral region. The studied molecular solid presented in the thesis has Raman band in this spectral region; hence Moissanite anvil cell (MAC) was chosen for high pressure Raman studies. The high pressure is generated by pressing two opposing Moissanite anvil by four screws. The schematic diagram of MAC is shown in Figure 2.12. The sample between two Moissanites is placed in metallic gasket that also provides the lateral support for the tips of anvils. High strength stainless steel is commonly employed as a metallic gasket for high pressure studies. The gasket is made of metallic foil having an initial thickness of 100-250 μm that is preindented to thickness of 30-80 μm by applying pressure to Moissanites and drilled at the centre of the crater left by Moissanites. The formed hole is filled with the sample and pressure marker (Ruby).

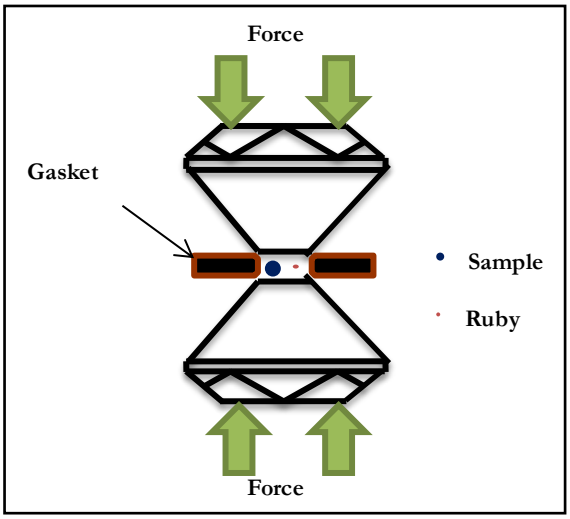

Figure 2.12. High pressure generation using anvil cell.

2.4.3. PRESSURE CALIBRATION

Ruby (Al_2O_3 doped with Cr_{3^+}) fluorescence method is most widely used for measuring the pressure inside the MAC/DAC in high pressure Raman studies [150, 151]. In the high pressure Raman investigation (section 3.2), the pressures were determined using the well established ruby fluorescence method. A few milliwatt power laser was used to excite the fluorescence of a ruby chip placed in the sample chamber. Ruby has two intense fluorescence

peaks R_1 and R_2 when excited by laser. The Figure 2.13 represents the recorded fluorescence spectrum of Ruby. Both these peaks are sensitive to pressure and shift to longer wavelengths as pressure increases. The stronger Ruby fluorescence line R_1 at 694.25 nm (300 K and ambient pressure) was used as pressure marker. This fluorescence line (R_1) shows remarkable pressure shift and is calibrated up to pressure 1Mbar [150]. The empirical formula for correlating the pressure and R_1 line of ruby is given by,

$$P = \frac{A}{B}\left[\left(\frac{\Delta\lambda}{\lambda_0} + 1\right)^{B} - 1\right] \qquad \textbf{(2.17)}$$

Where P is expressed in GPa, A (1904 GPa) and B (7.665) are the parameters for quasi-hydrostatic condition, and λ_0 (694.25 nm) is the wavelength of R_1 line at ambient pressure and room temperature [152]. Using this method, the resolution of the pressure can be achieved to ± 0.05 GPa.

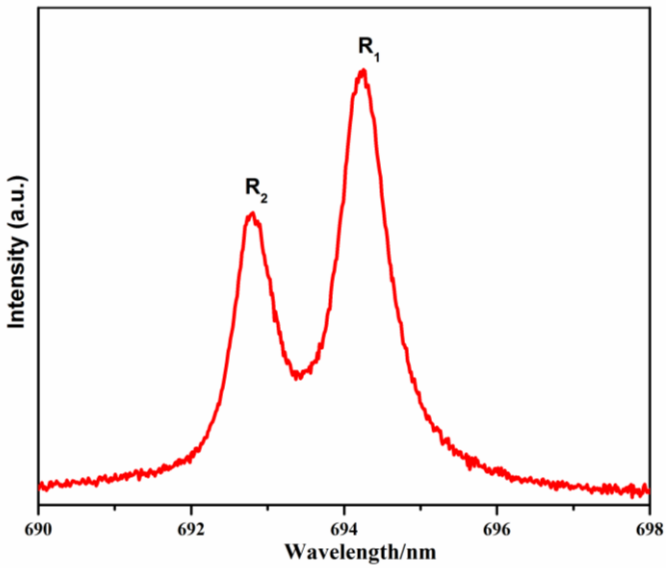

Figure 2.13. Ruby fluorescence lines (R_1 & R_2) measured at ambient pressure.

2.5. DENSITY FUNCTIONAL THEORY (DFT)

In order to get insight into the experimental results, the geometry optimization and vibrational frequencies calculations of some of the molecules were carried out using DFT method. Calculations were performed by Gaussian 03 software package using B3LYP exchange correlation functional and various basis sets. All the input details such as basis sets and exchange correlation functional used in DFT calculations are described in respective chapters (Chapter 3 & 4). The brief description of DFT method is described in Appendix II.

CHAPTER 3.

SERS AND HIGH PRESSURE RAMAN STUDIES OF TRANS-UROCANIC ACID

3.1. SERS STUDIES

3.1.1. INTRODUCTION

Trans-urocanic acid (t-UCA) is an epidermal biomolecule present in the upper most layers (4-34 nM/cm^2) of the human skin (stratum corneum) and considered as a major absorbing component of UV radiation [132, 133]. It is formed naturally from histidine in a deamination reaction catalysed by histidase in the epidermis. On the exposure of UV-B (280-320 nm) radiation, t-UCA gets isomerised into cis-urocanic acid (c-UCA) in vivo as well as vitro form by crossing the energy barrier of 1400 cm^{-1} (0.17 eV or 3.9 Kcal/mol) [153]. The chromophoric properties of t-UCA and its isomerization to c-UCA have been extensively studied by several groups [154-158]. Neutral form of t-UCA molecule can exist in various possible protonated states and have been considered for the various photo-physical and photo-chemical studies [157, 159, 160]. The photo-protectant property of t-UCA against UV induced damage of skin lead to its incorporation in commercial sunscreens and cosmetics products. However, later studies revealed that the c-UCA formed on exposure to UV radiation has immunosuppressive properties linked to skin cancer [158] and consequently the use of t-UCA in cosmetic products has been banned. Apart from its chromophoric properties, t-UCA is also considered as one of the natural moisturizing factor (NMF) present in the epidermis, and known to play an important role in skin hydration [132, 133]. Decrease in concentration of NMF components in the skin is an indicator of malfunction of filaggrin protein which leads to various skin disorders such as Atopic Dermatitis [134].

Owing to the above properties, t-UCA continues to be the subject of intense research of biomedical field. The spectroscopic information of NMF at physiological concentration can be used as a biomarker for diagnostics and research purposes. The unprecedented sensitivity of SERS has motivated us to probe the t-UCA at physiological concentration in

vitro phase based on its vibrational spectrum, and also to understand its interaction/adsorption behaviour with metal NP. The present SERS studies will be useful in the chemical analysis of the skin and help in understanding the relation between t-UCA concentration in skin and its associated disorders. The low level detection of t-UCA using SERS would be helpful to keep a check on the misuse of t-UCA in cosmetic products.

In the present SERS study, Ag NP sol is used because of the easy preparation method, and provides greater SERS enhancement. Also, the metal NP finds several applications in biology and medical field due to their biocompatible nature [161-164]. The SERS spectra along with normal Raman scattering (NRS) spectrum and their detailed interpretations about metal-molecule interaction/orientation on the Ag NP surface supported by DFT calculations are discussed and presented here.

3.1.2. EXPERIMENTS

Ag NP sol was prepared by the reduction of silver nitrate with sodium borohydride using the method of Creighton et. al.[146] as described in section 2.3.4. All the chemicals were of AR grade and obtained from Sigma and used without further purification. Ag NP sol and t-UCA functionalized Ag NP sol was characterized using Jasco UV-visible absorption spectrophotometer. NRS spectrum of t-UCA solid, its aqueous solution (10^{-1} M) and SERS spectra were recorded using the 532 nm output from a solid state laser of power ~15 mW. For the Raman measurements, the sample solutions were taken in a standard 1 × 1 cm^2 quartz cuvette and the Raman scattered light was collected in a backscattered geometry and detected using a CCD based home built monochromator [144]. The entrance slit was kept at 50 μm, which gives a spectral band pass of 3 cm^{-1}. The FTIR absorption spectrum of t-UCA solid in the spectral range 400-4000 cm^{-1} was measured using Bruker 80 V FTIR spectrometer equipped with KBr beamsplitter, DTGS detector, and globar source at spectral resolution of 2

cm^{-1}. For the SERS measurements, solutions of different concentrations of t-UCA were mixed with Ag NPs. (1:1 volume ratio of aqueous solution of t-UCA to Ag NPs). The measurements were repeated to ensure reproducibility.

3.1.3. COMPUTATIONAL DETAILS

In order to get insight into the experimental results, geometry optimization was carried out using DFT calculations for the zwitterion and the anions as well as their possible silver complexes, t-UCA-Ag and t-UCA-Ag_4 using B3LYP functional [165] and 6-31+G* (for t-UCA) and LANL2DZ (for Ag) basis set using Gaussian 03 program [166]. No symmetry restriction was applied during geometry optimization. On the basis of theoretical studies carried out by several groups [167, 168], two possible protonated states (N3-H & N1-H) of the t-UCA anion exist and were considered for the DFT calculation. The optimized structures of the zwitterionic and the two anionic tautomers of t-UCA are shown in Figure 3.1 and their positional coordinates are given in Appendix I. Among the optimized geometries of zwitterion and the two anionic tautomers, the anion forms are planar, while in the zwitterion the carboxylate group is 3^o out of the molecular plane. Of the two anionic tautomers (N3-H and N1-H) as shown in Figure 3.1 (b & c), the latter is slightly more stable by 8.16 kcal/mol. The optimized parameters of the zwitterion and the anion (N3-H) form of this study are compared with the reported values of Page et. al.[169] and are given in Appendix I. As seen in the Table AI.2, the calculated bond distances and bond angles show a reasonable match with the reported values. The vibrational frequencies for the three forms of t-UCA were computed at their optimized geometries to ensure that they correspond to local minimum on the potential energy surface and not to saddle points. The computed vibrations at the optimized geometries of the zwitterion and the two anionic tautomers of t-UCA were then compared with the NRS spectrum of solid and aqueous solution, respectively. The optimized

geometry of the possible t-UCA-Ag complexes for both anionic tautomers was computed. From a comparison of the optimized energies of the most stable t-UCA-Ag complex (Ag binding through the carboxylate group) of the two anionic tautomers, it was found that the N3-H-Ag complex was more stable than N1-H-Ag by 20.51 kcal/mol. Thus, the optimized geometries of all possible Ag complexes of the N3-H form of t-UCA are shown in Figure 3.2 (I, II and III), while the optimized structures for the Ag-complexes of N1-H form are shown in Figure 3.3. Figure 3.2 shows the possible Ag complexes of the N3-H form of t-UCA with Ag interacting through (i) the carboxylate group, (ii) both the carboxylate and the ethylenic π-bond and (iii) the imidazole ring N atom. The optimized energies for the three possible structures (I), (II) and (III) in the order of increasing energy are 0, 1.63 and 10.98 kcal/mol with the least stable structure being the one where the molecule interacts with Ag through the imidazole ring N-atom. The vibrational frequencies for the silver complexes of t-UCA were computed at the optimized geometry and compared with the SERS spectrum. For a better understanding of the molecular orientation on the Ag NP surface, the Ag_4 complexes of t-UCA (N3-H anion) were optimized and the computed structures are shown in Figure 3.2 (IV) and (V). Two probable optimized structures (IV) and (V) were obtained (i) with the t-UCA interacting with the Ag_4 through the carboxylate group and the ethylenic π-bond and (ii) with t-UCA interacting with Ag_4 through the carboxylate group, the imidazole ring N-atom and also through the ethylenic π-bond. The optimized energies of the structures showed that the structure (V) with t-UCA interacting with the carboxylate, imidazole ring N atom and through the ethylenic π-bond is relatively more stable by 2.45 kcal/mol in energy in comparison to the structure (IV) where the molecule interacts with the Ag surface only through carboxylate and the ethylenic π-bond. The positional coordinates of t-UCA Ag complexes for both the tautomers (N3-H & N1-H) are given in Appendix I.

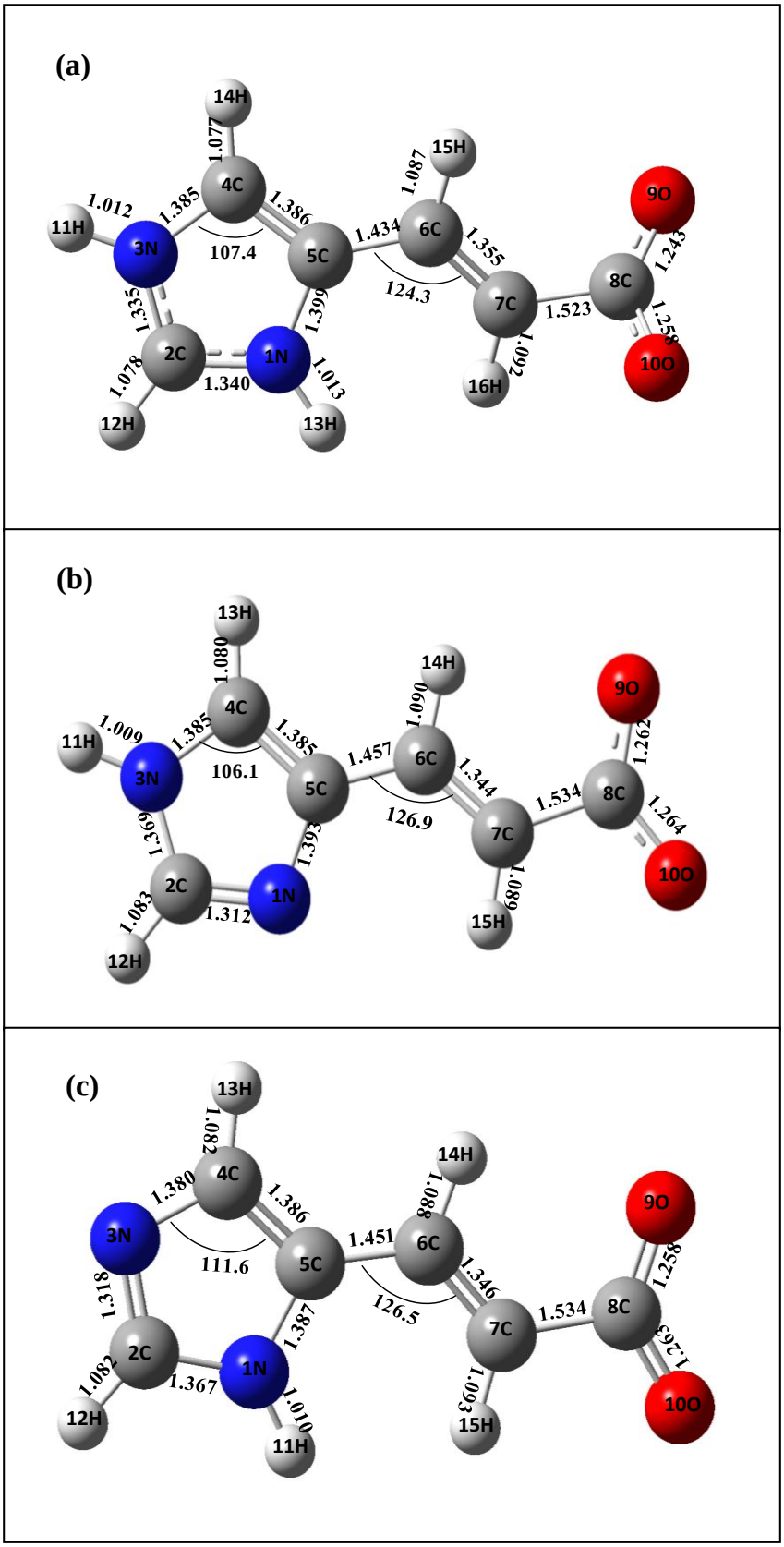

Figure 3.1. Optimized structures of (a) zwitterion, (b) N3-H tautomer of t-UCA anion and (c) N1-H tautomer of t-UCA anion.

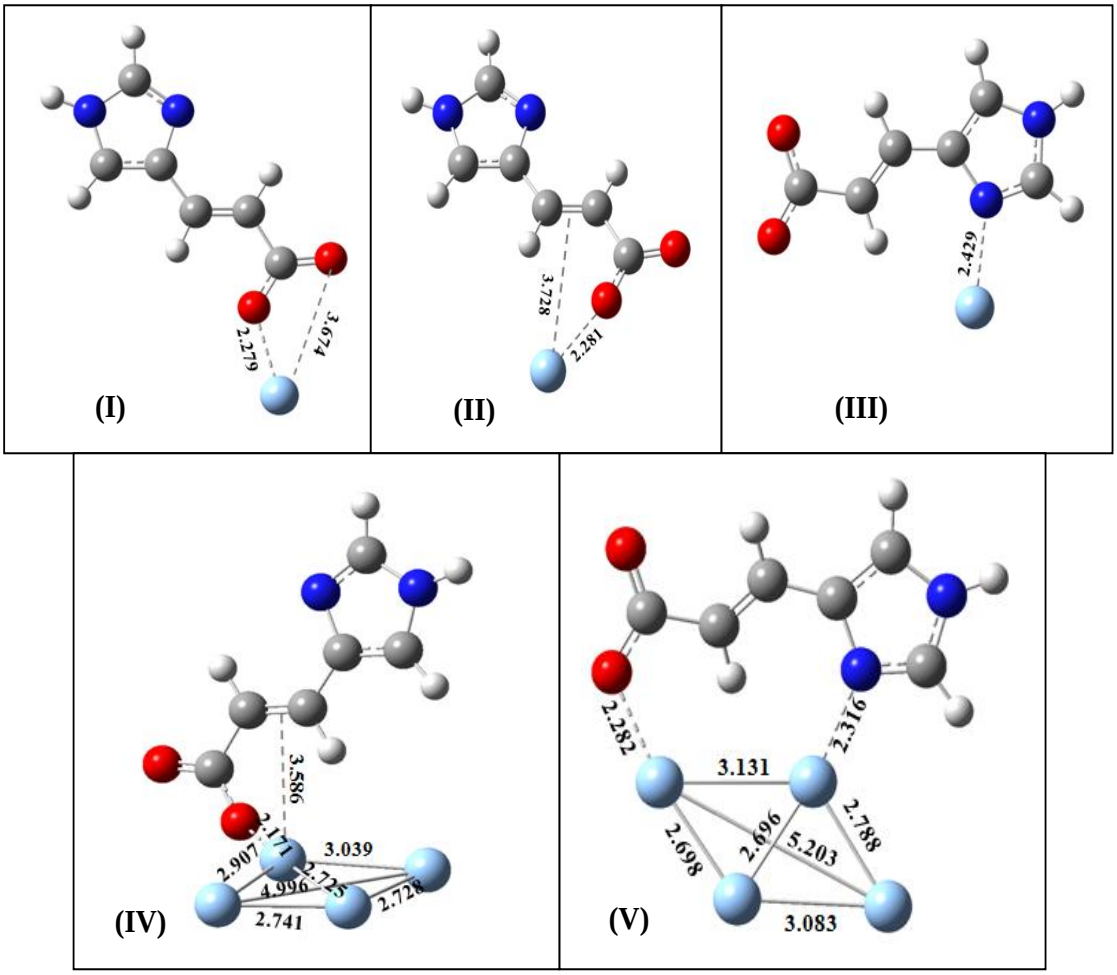

Figure 3.2. Optimized structures of various possible t-UCA-Ag and t-UCA-Ag_4 complexes of N3-H form of t-UCA.

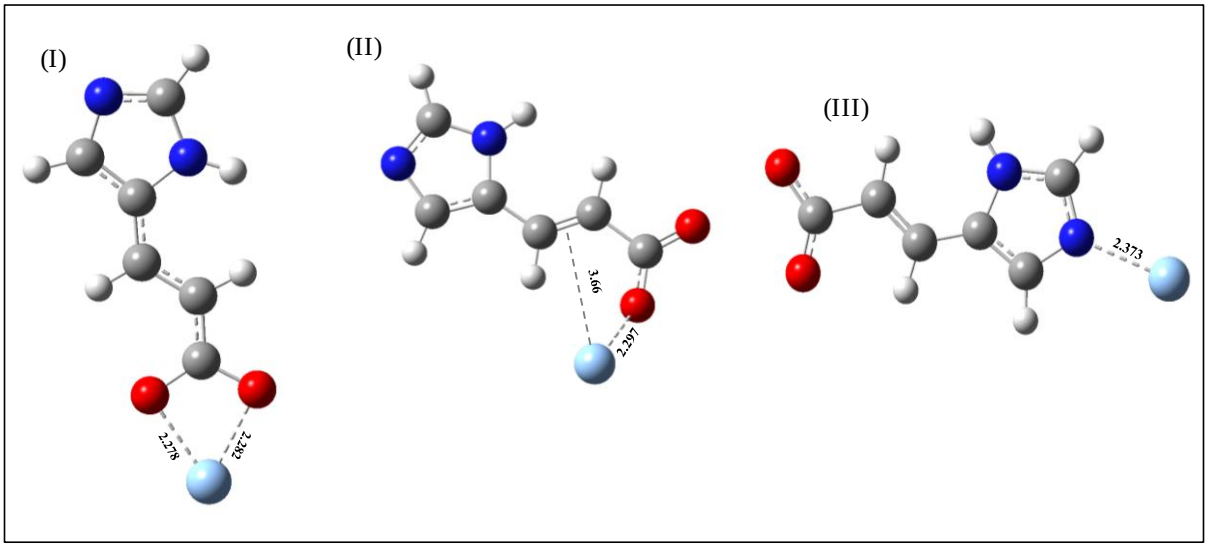

Figure 3.3. Optimized structures of various possible t-UCA-Ag complex of N1-H form of t-UCA.

3.1.4. RESULTS AND DISCUSSION

3.1.4.1. UV-VISIBLE ABSORPTION MEASUREMENTS

The absorption spectrum for the Ag NPs and the concentration-dependent (5×10^{-3} M to 5×10^{-9} M) t-UCA functionalized Ag NPs is shown in Figure 3.4. The figure shows the LSPR absorption band of Ag NPs at 395 nm. The absorption spectrum for different concentrations of t-UCA added to Ag NPs resulted in the emergence of a shoulder at 450 nm with decrease in intensity of the SPR band at 395 nm. The appearance of the shoulder is attributed to aggregate band [146, 170-172] induced by the adsorption of t-UCA on the silver surface.

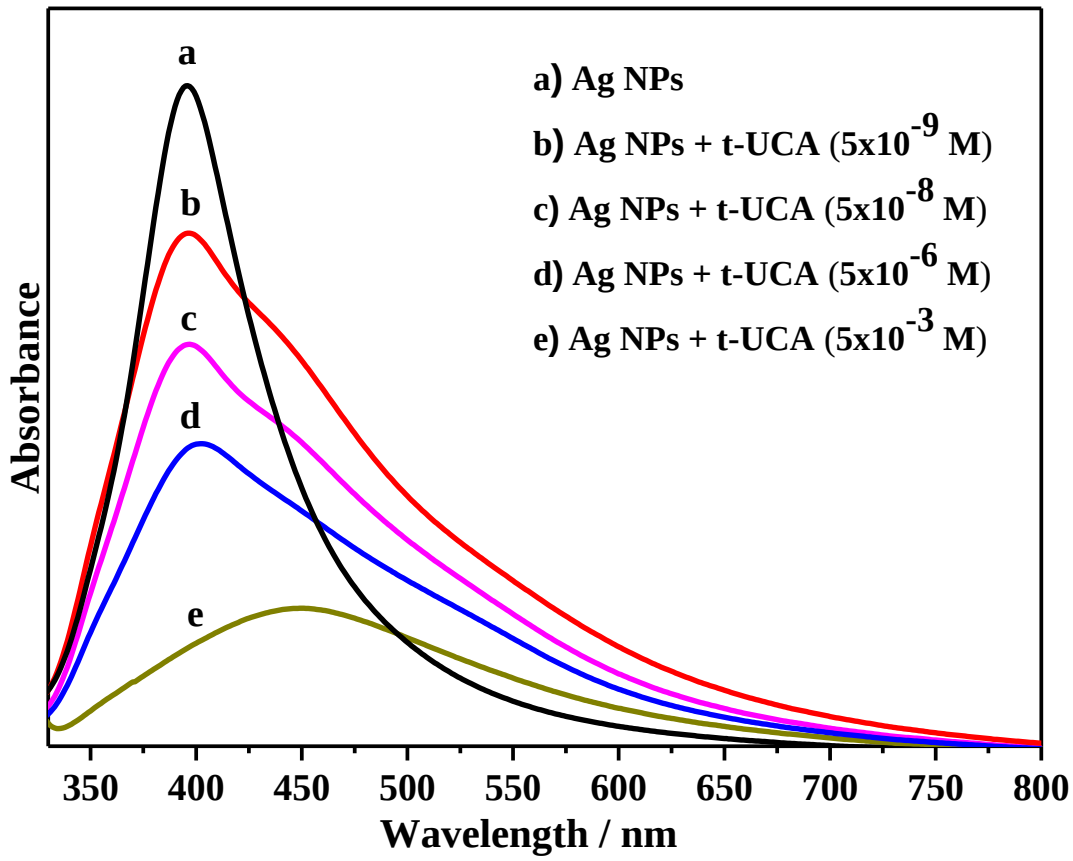

Figure 3.4. UV-visible absorption spectra of Ag NP sol and different concentrations of t-UCA mixed with Ag NP.

3.1.4.2. IR ABSORPTION AND NRS SPECTRA OF SOLID t-UCA AND AQUEOUS SOLUTION

t-UCA exists in zwitterionic form in the crystalline state [173]. In zwitterionic form, imidazole ring is positively charged and the negative charge is distributed over the carboxylate group. t-UCA exists as neutral, zwitterion, carboxylate anion and di-anions in the solution phase at pH < 3.5, 3.5-5.8, 5.8-13 and >13 respectively [174]. In the present study, pH of the aqueous solution of t-UCA was found to be ~8 and at this pH, the carboxylate anions are the predominant species. There are two tautomers of the carboxylate anion, namely N3-H and N1-H forms as shown in Figure 3.1(b) and (c). The optimized energies for the tautomers as seen in computational section are comparable and both the forms could possibly co-exist in aqueous solution. The IR, NRS spectrum of t-UCA solid and NRS spectrum of aqueous solution of t-UCA (10^{-1} M) are shown in Figure 3.5 a, b and c, respectively and the observed frequencies and their assignments are tabulated in Table 3.1 and Table 3.2 based on the calculated frequencies of zwitterion and anionic tautomers of t-UCA respectively. In the IR spectrum of solid t-UCA (Figure 3.5 (a)), strong bands observed at 1343 (1256) and 860 cm^{-1} are assigned to ethylenic C-H bend along with imidazole ring C-H in-plane (ip) bend and ethylenic C-H out of plane (oop) bend along with ethylenic C=C twist. Few medium intense bands are observed at 1665, 1587, 1476, 1166, 1045, 966, 943, 785, 679 and 629 cm^{-1}. Of these modes, 1665, 1587 and 1491 cm^{-1} are assigned to ethylenic C=C stretch/asymmetric (asym) CO_2^- stretch, ring C-N stretch/ring C-H, NH bends and ring N-H, CH bends/C-N stretch, respectively. The band at 1166 and 1045 cm^{-1} are attributed to ring NH, CH ip bends. The bands at 966 and 943 cm^{-1} are assigned to ip ring bend. The band at 785 cm^{-1} is attributed to C=C-CO_2^- ip bend. The bands at 679 and 629 cm^{-1} are assigned to CO_2^-ip bend and NH oop bend/ring torsion. In addition, several weak vibrational bands are observed at 1536 (ring stretches), 1391 (sym CO_2^- stretch), 1320 (ring breathing), 1296, 1232

Table 3.1. Assignments of Infrared and Raman vibrations of t-UCA solid.

Infrared (Solid)	**Raman (Solid)**	**Calc. (Zwitterion)**	**Assignment**
1665 m	1664 s	1653	ν C6=C7, ν_{asym} CO_2^-
1587 m	1584 w	1601	ν C2-N3, ν C6=C7, δ C-H, δ N-H
1536 sh	1536 w	1555	ν C2-N3, ν C2-N1
1476 m	1491 m	1503	δ N3-H, δ C2-H, ν C4-N3
1391 sh	1392 w	1350	ν_{sym} CO_2^-
1343 s	1337 w	1317	δ C6-H, δ C4-H
1320 sh 1296 w	1322 w	1300	Rg breathing
1256 s	1261 m	1292	δ C7-H, δ C6-H, δ C4-H
1232 sh	1241 m	1235	δ C6-H, δ C7-H, δ C4-H
	1192 w	1198	δ N3-H, δ C2-H
1166 m	1161 w	1158	δ N1-H, δ C4-H, δ C2-H
1103 w 1045 m	1104 w	1091	δ C4-H, δ C2-H, δ N3-H
966 m	963 w	985	δ N3-C2-N1
943 m	948 w	935	δ C2-N3-C4
		955	γ C6-H, γ C7-H
872 sh	872 w	926	ν C7-CO_2^-
860 s	850 w	859	tw C6-C7, γ C6-H, γ C7-H
785 m	786 w	794	δ C6=C7-CO_2^-
738 w	738 w	758	γ C2-H, γ C4-H, γN3-H, τRg
679 m	676 w	658	δ CO_2^-
629 m	626 w	626	τRg, γ N3-H, γ N1-H
538 w	535 w	595	τRg, γ N3-H, γ C2-H
	355 w	369	ρskel.

ν: stretch; sym: symmetric; asym: asymmetric; δ: in plane bend; γ: out of plane bend; τ : torsion; tw: twist; ρ: rock; s: strong; m: medium; w: weak; sh: shoulder; Rg: ring; skel: skeletal.

Table 3.2. Assignments of Raman vibrations of t-UCA in aqueous solution and on Ag NP.

Raman (Aqueous solution)	**Calc. (Anion) N3-H**	**Calc. (Anion) N1-H**	**SERS**	**Calc. (t-UCA-Ag)**	**Assignment**
1650 s	1697	1693	1638 s	1706	νC6=C7, ν_{asym}
1555 w	1647	1586	1557 w	1564	νC4=C5
			1521 w	1541	νC4=C5, δ C4-H
			1488 w	1497	ν C2-N1, δ N-H, δ C2-H
1456 w	1457	1496	1454 w	1420	νC2-N3, δ N-H
1384 m	1355	1343	1374 m	1285	ν_{sym}
1350 w	1345	1381	1349sh	1347	νN1-C5, δ C6-H
			1321 sh	1302	Rg breathing
1285 m	1251	1282	1272 m	1256	δ C7-H, δ C6-H
1252 w	1193	1216	1231 m	1203	δ C6-H, δ C7-H
			1187 w 1164* w	1132	δ N-H
			1121 w	1082	δ C4-H, δ C2-H
			1038 w	1024	γ C7-H, γ C6-H
			965 w	958	δ C2-N1-C5
			945 w	944	δ N3-C2-N1
			920* w	934	tw C6-C7, γ C6-H , γ C7-H
			803 w	788	δ C=C-CO_2^-
			740 w	728	γ C4-H, γ C2-H, τRg
			692 w	675	τskel.
			667 w	646	δ CO_2^-
			652 w	642	τRg, γ N-H
			550 w	530	ρethylenic
			410 w	358	ρskel.
			359 w	347	τskel.

ν: stretch; sym: symmetric; asym: asymmetric;δ: in plane bend; γ: out of plane bend;τ: torsion;tw: twist;ρ: rock; s: strong; m: medium; w: weak; sh: shoulder; Rg: ring;skel: skeletal; *corresponds to the peak appearing at concentrations ($\leq 5 \times 10^{-7}$ M) of t-UCA.

(ethylenic and ring CH ip bend), 1103 (ring CH, NH ip bends), 872 (C-CO_2^- stretch), 738 (CH, NH oop bend and ring torsion) and 538 cm^{-1} (ring NH, CH oop bend and ring torsion). The absence of C=O stretching vibration around 1700 cm^{-1} in the IR spectrum clearly indicates that the molecule exists in the zwitterionic form in the solid state. Recently, there was a report on the assignment of the vibrational bands of solid t-UCA using DFT calculations by considering the neutral form of solid t-UCA instead of zwitterionic form [175]. In the NRS spectrum of solid t-UCA (Figure 3.5 (b)), a strong band observed at 1664 cm^{-1} is assigned to ethylenic C=C stretch. Few medium intense bands are observed at 1491, 1261 and 1241 cm^{-1}. Of these modes, 1491 cm^{-1} is assigned to ring N-H, C-H ip bend and C-N stretch. The bands at 1261 and 1241 cm-1 are attributed to of ethylenic CH and ring CH ip bend. Weak bands observed at 1392 and 676 cm^{-1} are assigned to sym stretch and ip bend of CO_2^-, respectively. Bands at 963 and 948 cm^{-1} are due to ring ip bend and bands observed at 1161 and 1104 are assigned to ring N-H and C-H ip bend. The band at 1536 is due to ring C-N stretch while band at 1584 is assigned to ring C-N stretch/ethylenic C=C stretch / ring C-H and N-H ip bend. In addition, several weak vibrational modes are observed at 1337 (ethylenic and ring CH ip bend), 1322 (ring breathing), 1192 (ring N-H and C-H ip bend), 872 (C-CO2- stretch), 850 (C=C twist and ethylenic C-H oop bend), 786 (C=C-CO_2^- ip bend), 738 (ring N-H/C-H oop bend and ring torsion), 626 (ring torsion and N-H oop bend), 535 (ring torsion and ring N-H/C-H oop bend) and 355 cm^{-1} (skeletal rock). The NRS spectrum of aqueous t-UCA (10^{-1} M) is shown in Figure 3.5 (c). In the spectrum, ethylenic C=C stretch, ethylenic CH ip bend and CO_2^- sym. stretch were observed as prominent bands at 1650, 1285 and 1384 cm^{-1}, respectively. Few weak bands were observed at 1555, 1456, 1350 and 1252 cm^{-1}. Of these observed modes, the band at 1555 cm^{-1} is due to imidazole ring C=C stretch and the bands at 1456 and 1350 cm^{-1} belongs to ring C-N stretch/N-H ip bend and ring C-N

stretch/ethylenic C-H ip bend, respectively. The band at 1252 cm^{-1} is due to ethylenic CH ip bend. No spectral features are observed in the region below 1200 cm^{-1}.

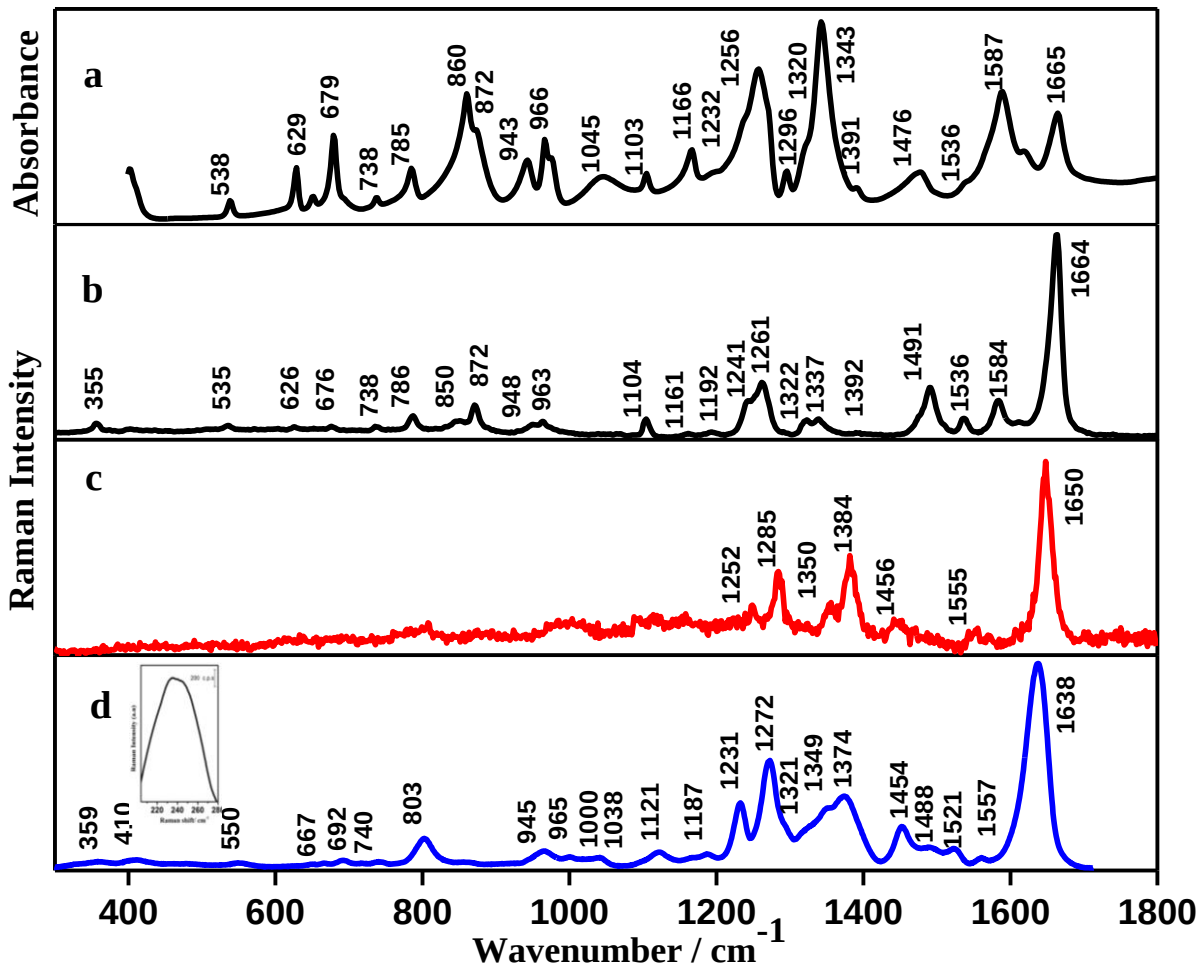

Figure 3.5. (a) Infrared absorption spectrum of t-UCA powder, (b) NRS spectrum of t-UCA powder, (c) NRS spectrum of t-UCA aqueous solution (10^{-1} M) and (d) SERS spectrum of t-UCA (5×10^{-5} M).

3.1.4.3. SERS SPECTRA OF t-UCA AND ITS INTERPRETATION

SERS spectra of t-UCA at different concentrations (5×10^{-3} M to 5×10^{-12} M) were recorded and are presented in Figure 3.6. Maximum enhancement was observed for 5×10^{-5} M concentration of t-UCA. The concentration dependent SERS studies are elaborated in the

subsequent section. In this section, the SERS spectrum obtained for 5×10^{-5} M concentration (Figure 3.5d) is compared with the NRS spectrum of aqueous solution (Figure 3.5c).

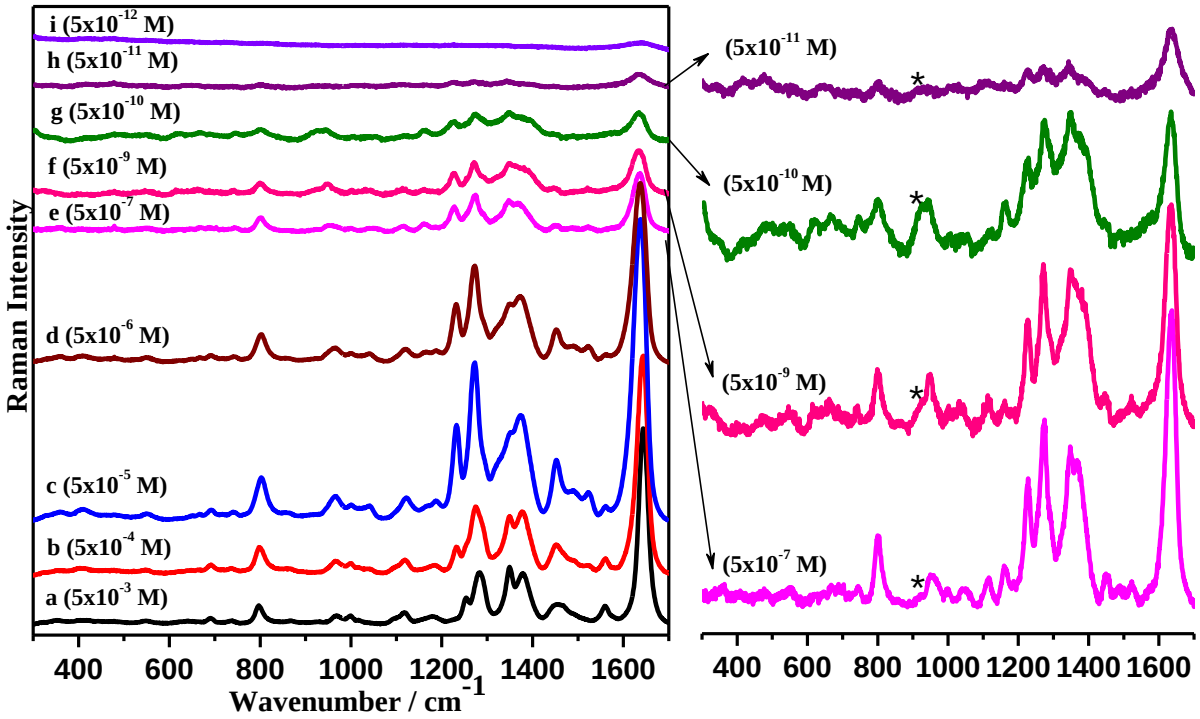

Figure 3.6. SERS spectra of different concentrations (5×10^{-3} M to 5×10^{-12} M) of t-UCA. On the right, the expanded SERS spectrum is shown for 5×10^{-7} M, 5×10^{-9} M, 5×10^{-10} M and 5×10^{-11} M. *corresponds to the 920 cm^{-1} band appearing at concentrations ($\leq 5 \times 10^{-7}$ M) of t-UCA.

The enhanced Raman spectrum showed several prominent bands at 1638 (ethylenic C=C stretch), 1374 (sym. CO_2^- stretch) and 1272/1231 (ethylenic C-H ip bend). Of these vibrations, the ethylenic C=C stretching mode is red shifted by 12 cm^{-1} from the NRS spectrum. Similarly, the bands corresponding to the ethylenic CH ip bend also showed red shift of 13 and 21 cm^{-1} compared to 1285 and 1252 cm^{-1} in NRS spectrum, respectively. The band attributed to the sym. CO_2^- stretch (1374 cm^{-1}) is also red shifted as compared to the 1384 cm^{-1} band observed in the NRS spectrum of aqueous t-UCA solution. While all the prominent bands involving ethylenic C=C stretch/C-H ip bend and sym. CO_2^- stretch showed significant red shift, the imidazole ring stretches (C=C, C-N) appearing at 1557, 1454 and

1349 cm^{-1} showed no noticeable shift when compared to the NRS spectrum of aqueous t-UCA. Also, several weak Raman bands are observed at 1121, 1038, 1000, 965, 945, 803, 740, 692, 667, 652, 550, 410, and 359 cm^{-1}, which are not seen in the NRS spectrum of aqueous t-UCA. Of these modes, the band at 1121 cm^{-1} belongs to ring C-H ip bend, while the bands at 965 and 945 cm^{-1} correspond to ring ip bend. The mode at 1038 cm^{-1} is attributed to the ethylenic CH oop bend while the vibrations observed at 1121 and 740 cm^{-1} are due to the ring CH ip bend and ring CH oop bend, respectively. The bands at 803 and 667 cm^{-1} are attributed to C=C-CO_2^- and CO_2^-ip bends. There are other weak bands observed at 692 (skeletal torsion), 652 (ring torsion/ N-H oop bend), 550 (ethylenic rock), 410 (skeletal rock) and 359 (skeletal torsion) cm^{-1}.

Shifts in the vibrational frequencies, changes in the relative intensities and appearance of new modes in the SERS spectrum of adsorbed molecular species when compared to the NRS spectrum of the molecules provide information of the molecular binding sites, the relative proximity of different parts of the adsorbed molecule and the orientation of the adsorbed molecule on the surface. The orientation of the molecule can be obtained through the application of the "surface selection rules"[55-59] which states that the normal modes of adsorbed molecules involving changes in the molecular polarizability with a component perpendicular to the surface are subject to the greatest enhancement. In the case of t-UCA, red shifts are observed for the vibrational bands associated with ethylenic and CO_2^- groups which gives evidence that both these groups are involved in chemical interaction with the silver surface. The interaction of π electron cloud of ethylenic C=C with the metal reduces the bonding electron density of the double bond and hence lowers the ethylenic C=C stretch. Consequently, there is also a red shift in the CH ip bend of the ethylenic group. Similarly, there is a red shift in the sym. stretch of the CO_2^- group arising due to the interaction with the metal surface. However, the vibrational modes related to the imidazole ring showed

negligible shift which implies that the ring is not directly involved in binding to the surface. The above observation suggests that the imidazole ring is away from the silver surface. A weak shoulder was also observed at ~225 cm^{-1} (shown in inset of Figure 3.5 d), which is due to the Ag-O stretch [50, 176]. The aforementioned observations imply that the molecule remains slightly tilted on the silver surface enabling chemical interactions through ethylenic π bond and CO_2^- group with the imidazole ring lying away from the metal surface. This observation is supported by the optimized geometry of t-UCA-Ag_4 (structure IV in Figure 3.2) where the molecule remains slightly tilted on the silver surface. The ethylenic C=C lies parallel to the surface when the molecule remains slightly tilted on the surface. According to the "surface selection rules" the polarization change of the π electrons of ethylenic C=C in the direction perpendicular to the molecular plane is normal to the silver surface during the vibration and hence results in enhancement of C=C stretch as shown in the inset of Figure 3.7 [57, 177].

3.1.4.4. SERS SPECTRA AT DIFFERENT CONCENTRATIONS

Concentration dependent SERS spectra of t-UCA in the range 5×10^{-3} M to 5×10^{-12} M are shown in Figure 3.6. The SERS spectra of t-UCA showed good signal to noise ratio down to the concentration of 5×10^{-11} M. For 5×10^{-12} M concentration of t-UCA, no discernible spectral features were observed except for the appearance of a broad band at 1640 cm^{-1} which is due to the ip bend of water. With increase in t-UCA concentration, the SERS features started to appear and reached a maximum at 5×10^{-5} M and gradually there was a decrease in the intensities with further increase in the concentration up to 5×10^{-3} M. It is known that SERS signal attains a maximum at monolayer coverage and the 'first layer effect' contributes to the maximum enhancement and with multilayers the signal decreases [178, 179]. This suggests that at 5×10^{-5} M there is monolayer formation of the adsorbed t-UCA on the silver

surface. At higher concentrations (> 5×10^{-5} M), the SERS signal arises from the multilayers present on the surface of the nanoparticles which tends to manifest the bulk properties. For the concentration range 5×10^{-7} to 5×10^{-11} M, zoomed spectra are shown on the right side of Figure 3.6. Apart from an overall decrease in the intensities, there are several changes observed in the SERS spectrum as discussed below. A new band at 920 cm^{-1} assigned to ring C-H oop bend starts appearing at 5×10^{-7} M and gains intensity with lowering of concentration. In addition, the band at 1187 cm^{-1} assigned to NH ip bend observed at higher concentration is shifted to 1164 cm^{-1} at lower concentrations (<5×10^{-5} M). Such a red shift or weakening of the NH ip bend occurs due to interaction of the ring N with the silver surface and such interaction is possible with the imidazole ring being close to the surface. The appearance of the band at 920 cm^{-1} suggests the ring lies flat with respect to the surface according to the "surface selection rules". The band at 1374 cm^{-1} assigned to CO_2^- stretch gets broadened at lower concentration which also indicates that the above group lie flat enabling interaction of the π electrons with the surface. These observations suggest a change in orientation of t-UCA on the silver surface from a slightly tilted to flat geometry at concentrations <5×10^{-5} M with the imidazole ring in proximity to the metal surface as shown in the calculated optimized structure V (Figure 3.2) of t-UCA-Ag_4. The flat geometry with respect to the surface enables the interaction of the molecule through the imidazole ring N in addition to the π electrons of ethylenic double bond and carboxylate group. The structure V also explains the decrease in relative intensity of the ethylenic C=C stretch in comparison to the bands in the range 1200-1400 cm^{-1}. The ethylenic C=C bond lies parallel to the surface in a slightly tilted geometry (5×10^{-5} M) as shown in structure IV (Figure 3.2) resulting in a higher intensity for the C=C stretch as discussed in the previous section. At lower concentrations, the optimized structure V (Figure 3.2) shows the C=C bond becomes slightly tilted relative to the surface leading to a decrease in the intensity for the ethylenic C=C

stretch. The orientation of t-UCA on the Ag NP surface is schematically shown in Figure 3.7. Concentration dependent SERS results show that at low concentrations (sub monolayer coverage), the t-UCA molecules have more freedom to interact through all its potential available sites (COO^-, C=C and ring N) with the nanoparticle surface thereby assuming a flat orientation. With increase in concentration, the molecules get stacked in perpendicular orientation with a slight tilt to accommodate more number of t-UCA molecules with interactions through the carboxylate group and ethylenic C=C bond.

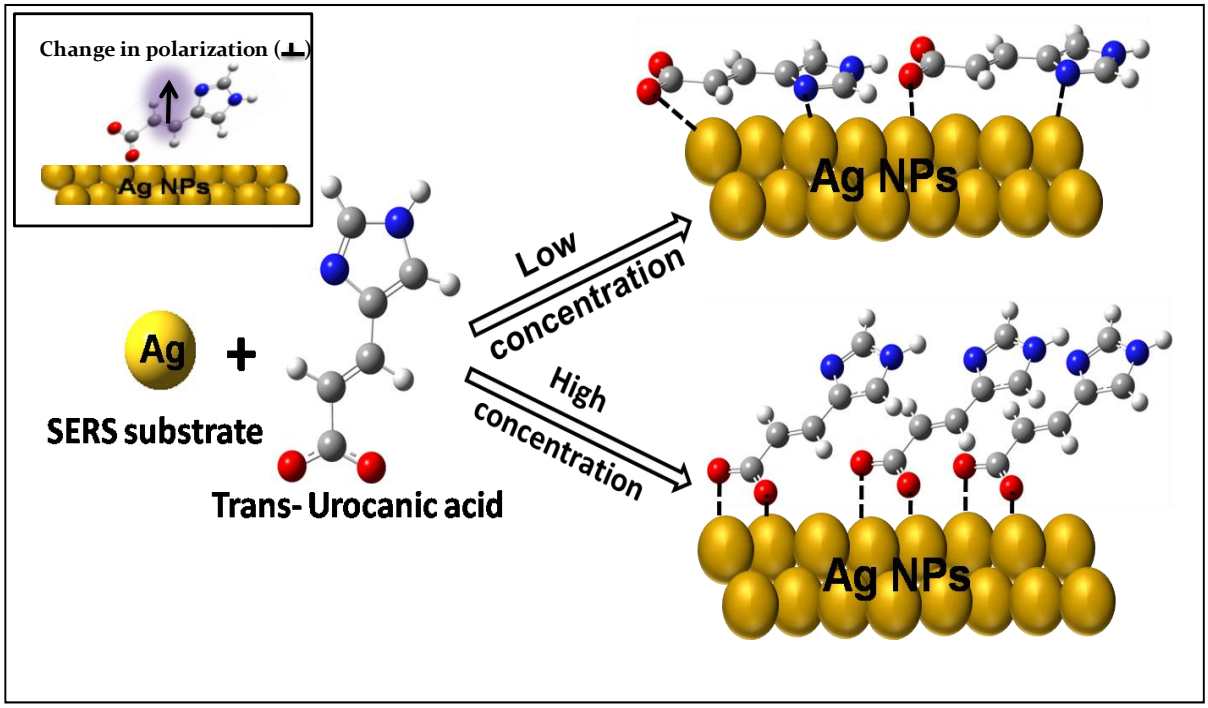

Figure 3.7. Schematic of the possible orientation of t-UCA on the Ag surface. Inset shows the change in polarization normal to silver surface.

3.1.4.5. ANALYTICAL ENHANCEMENT FACTOR (AEF)

The AEF is one of the most important numbers to quantify the SERS effect. This is a significant quantity in the practical application of SERS since it gives an idea of the amount of SERS signal that can be obtained when compared to normal Raman signal under a given experimental condition. Under the same experimental conditions of laser power, wavelength

and preparation method, the AEF is expressed as AEF = $(I_{SERS}/I_{NRS}) \times (C_{NRS}/C_{SERS})$, where C_{NRS} and C_{SERS} are molar concentration of solutions used in NRS and SERS respectively, and I_{SERS} and I_{NRS} are the intensities of the vibrational mode.

The AEF of the SERS bands corresponding to ethylenic C=C and the carboxylate stretches has been estimated. The values of C_{NRS} and C_{SERS} are 10^{-1} M and 5×10^{-10} M. Intensities of SERS and NRS bands of ethylenic C=C and the carboxylate stretches were measured and are as follows: I_{SERS}(C=C) = 7191 counts, ($I_{SERS}(CO_2^-)$ = 5782 counts, I_{NRS}(C=C) = 2073 counts, $I_{NRS}(CO_2^-)$ = 1043 counts. The mentioned total counts were obtained after 50 second of exposure. Subsequently, calculated AEF for the ethylenic C=C and carboxylate stretches were found to be ~ 6.9×10^8 and 5.5×10^8, respectively.

3.1.5. CONCLUSIONS

SERS spectrum of t-UCA down to 50 picomolar concentration was obtained with good signal to noise ratio. Highest SERS intensity due to the "first layer effect" was observed at 50 μM at t-UCA concentration. The analytical enhancement factors were calculated for the ethylenic C=C and carboxylate stretches and were found to be ~ 10^8. The Raman vibrations of t-UCA were interpreted with the help of DFT calculations. The SERS features strongly suggest chemical interaction of the molecule through the π electrons of the ethylenic bond and the carboxylate group with the molecule assuming a slightly tilted geometry on the silver surface. At concentrations of t-UCA lower than 50 μM, the molecule assumes a flat geometry orientation on the Ag surface.

3.2. HIGH PRESSURE RAMAN STUDIES

3.2.1. INTRODUCTION

We have carried out the high pressure Raman studies of t-UCA to understand the effect of pressure in the π ethylenic bond and the molecular structure. In this section, we describe the high pressure Raman investigation on t-UCA biomolecule. The presence of imidazole ring and acrylic acid in its molecular structure and strong activity associated with π electrons of acrylic ethylenic bond makes it an interesting compound to investigate under pressure, since both the imidazole and acrylic acid under pressure have shown interesting structural changes leading to the onset of polymerization [120, 180].

It is worth mentioning here that various unsaturated hydrocarbons containing ethylenic bonds show varying behaviour under pressure [121, 125]. Many of the unsaturated organic molecules with double and triple bonds are reported to be transformed to new compound, in particular polymeric form by the application of a pressure [121, 123, 129]. In the case of butadiene, pressure-induced dimerization is found to occur at pressures above 0.7 GPa and dimerization is completely suppressed by the rapid formation of pure trans polybutadiene upon irradiating the high-pressure sample with 488 nm Ar+ laser [121]. Unsaturated hydrazine derivatives, azobenzene and hydrazobenzene were investigated under high pressure [126] and both compounds are reported to exhibit a pressure induced phase transition at 10 GPa. Further compression of azobenzene to 18 GPa resulted in an destruction of molecular structure; in contrast the molecular structure of hydrazobenzene was found to be stable up to 28 GPa. While acrylic acid, unsaturated organic compound, shows onset of polymerization beyond 8GPa [180] and crotonic acid is found to undergo first order phase transition at 6 GPa [181]. Carnosine, a dipeptide of L-histidine and β-alanine shows onset of polymerization at 2.8 GPa, and substantial fraction of the monomer is converted to polymer

at pressure above 12GPa [120]. Apart from the above changes, pressure induced isomerization for unsaturated hydrocarbons are also reported [121, 182-187]. For instance, maleic acid is reported to undergo isomerization to form fumaric acid (trans) at ~2 GPa [182]. Hence, it would be interesting to study the behaviour of various types of unsaturated molecules under pressure in order to look for new products formed at high pressures. Clearly, any irreversible structural changes under such conditions can be exploited for various applications in optics, electronics and biomedical field [125, 127].

The present high pressure Raman studies are aimed to shed light on the pressure effect on the molecular conformations and the stability of t-UCA molecules at high hydrostatic pressure, which can be useful for biomedical research applications. The studies will be also helpful for carrying out SERS studies under high pressure in near future. Here, we describe the vibrational spectroscopic studies of t-UCA under high pressure upto ~14 GPa using in-situ Raman spectroscopy.

3.2.2. EXPERIMENTS

High pressure Raman scattering spectra of t-UCA were acquired with a triple stage confocal micro Raman spectrograph (JobinYvon T64000). The high pressure cell used in this experiment was symmetric moissanite anvil cell with culet size of ~400 μm. Sample was loaded in a tungsten gasket hole of ~120 μm diameter, drilled after pre-indenting it to a thickness of ~50 μm and the Raman scattering was excited using 514.5 nm laser obtained from Ar^+ laser. The scattered light was collected using backscattering geometry using 20 x microscope objectives. The typical accumulation time for each spectrum was 8 s and 10 scans were coadded in order to improve the signal to noise ratio. The pressure calibration was done by using ruby fluorescence. High pressure spectra are recorded without pressure transmitting

medium in order to avoid any possible cross contamination of t-UCA sample. Moreover, t-UCA is soft molecular solid which provides a quasi-hydrostatic condition

3.2.3. RESULTS

The Raman spectra of t-UCA upon compression in the frequency regions 180-960 cm^{-1}, 970-1800 cm^{-1} and 2800-3400 cm^{-1} at various pressures up to 13.8 GPa, along with the Raman pattern after decompression, are presented in Figure 3.8 (a), Figure 3.9 (a) and Figure 3.10 (a) respectively. Apparent variations, for example emergence of new modes, splitting of modes and disappearance of original modes that occur in the Raman spectra are indicative of a pressure-induced structural modification across 1.4 & 7.5 GPa. In order to find the pressure induced variations in the Raman modes, the pressure dependence of the corresponding Raman modes (frequency versus pressure) have been plotted in Figure 3.8 (b), Figure 3.9 (b), and Figure 3.10 (b).

t-UCA exists in zwitterionic form in the crystalline state and structurally it comprises of two parts, imidazole and acrylic part as shown in Scheme 3.1. In the zwitterionic form, the imidazole ring is positively charged and the negative charge is distributed over the carboxylate group of acrylic part.

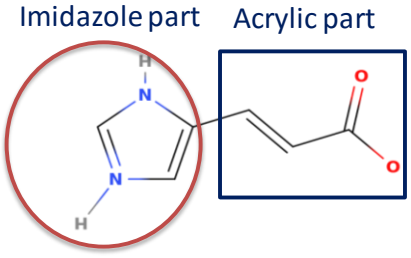

Scheme 3.1. Molecular structure of t-UCA.

3.2.3.1. RAMAN SPECTRUM OF t-UCA AT AMBIENT PRESSURE

The Raman modes of t-UCA were assigned with the help of reported vibrational frequencies [49, 180, 188] and the detailed assignments of the Raman modes at ambient condition are tabulated in Table 3.3. In the Raman spectrum of solid t-UCA at ambient condition, a strong band observed at 1664 cm^{-1} is assigned to ethylenic C=C stretch. Few medium intense bands are observed at 1491, 1261 and 1241 cm^{-1}. Of these modes, 1491 cm^{-1} is assigned to ring ν C-N stretch, δ N-H, δ C-H. The bands at 1261 and 1241 cm^{-1} are assigned to δ CH (ethylenic) and δ CH (Rg) respectively. Weak band observed at 676 cm^{-1} is assigned to δ CO_2^-. Bands observed at 1161 and 1104 cm^{-1} are attributed to δ N-H and δ C-H (Rg) vibrational modes respectively. The band at 1536 cm^{-1} is due to ring ν C-N stretch while band at 1584 cm-1 is assigned to ν C-N, δ C-H (Rg) and δ N-H. In addition, several medium and weak vibrational modes are also observed at 1337 (δ CH (ethylenic), δ CH (Rg)), 1322 (ring breathing), 1192 (δ N-H & δ CH (Rg)), 872 (ν C-CO_2^-), 850 (tw C=C & γ C-H (ethylenic), 737 (γ C-H (Rg), γ N-H, τ Rg), 626 (τ Rg, γ N-H), 535 (τ Rg, γ N-H, γ C-H (Rg)) and 355 cm^{-1} (ρ skel.). The weak mode at 1614 cm^{-1} is attributed to ν C=C (Rg), ν C-N & δ C-H (Rg). The modes pertaining to stretching vibrations of C-H are also observed in 2800-3400 cm^{-1} spectral region. The modes observed at 3165, 3087, 3043 and 3027 cm^{-1} are attributed to the stretching vibrations of ν C-H (Rg) and ν C-H (ethylenic) respectively.

Table 3.3. Assignments of Raman mode of t-UCA powder sample.

Raman (Solid) Ambient	Assignment
3165 w	ν C-H (Rg)
3087 w	ν C-H (Rg)
3043 w	ν C-H (ethylenic)
3027 m	ν C-H (ethylenic)
1664 s	ν C=C (ethylenic)
1614 w	ν C=C (Rg), ν C-N, δ C-H (Rg)
1584 w	ν C-N, δ C-H (Rg)
1536 w	ν C-N
1491 m	δ N-H, δ C-H (Rg), ν C-N
1337 w	δ C-H (ethylenic), δ C-H (Rg)
1322 w	Rg breathing
1261 m	δ C-H (Ethylenic))
1241 m	δ C-H (Rg)
1192 w	δ N-H, δ C-H (Rg)
1161 w	δ N-H, δ C-H (Rg)
1104 w	δ C-H (Rg), δ N-H
872 w	ν C-CO_2^-
850 w	tw C=C (Ehtylenic), γ C-H (Ehtylenic)
786 w	δ C=C-CO_2^-
737 w	γ C-H (Rg),γN-H, τRg
676 w	δ CO_2^-
626 w	τRg, γ N-H
535 w	τRg, γ N-H, γ C-H (Rg)
402 w	τRg, γ N-H
355 w	ρskel.
268 vw	ρRg.
209 vw	τ(C–C)
ν: stretch; sym: symmetric; asym: asymmetric; δ: in-plane bend; γ: outof-plane bend; τ: torsion; tw: twist; ρ: rock; s: strong; m: medium; w: weak;sh: shoulder; Rg: ring; skel: skeletal.	

3.2.3.2. RAMAN SPECTRA OF t-UCA ON COMPRESSION AND DECOMPRESSION

LOW FREQUENCY REGION 180-960 cm^{-1}

Figure 3.8 (a) represents the Raman spectra of t-UCA upon compression in the frequency region 180-960 cm^{-1} at various pressures up to 13.8 GPa followed by the spectrum at final decompression. The change in frequency of Raman modes with the application of pressure are plotted and shown in Figure 3.8 (b).

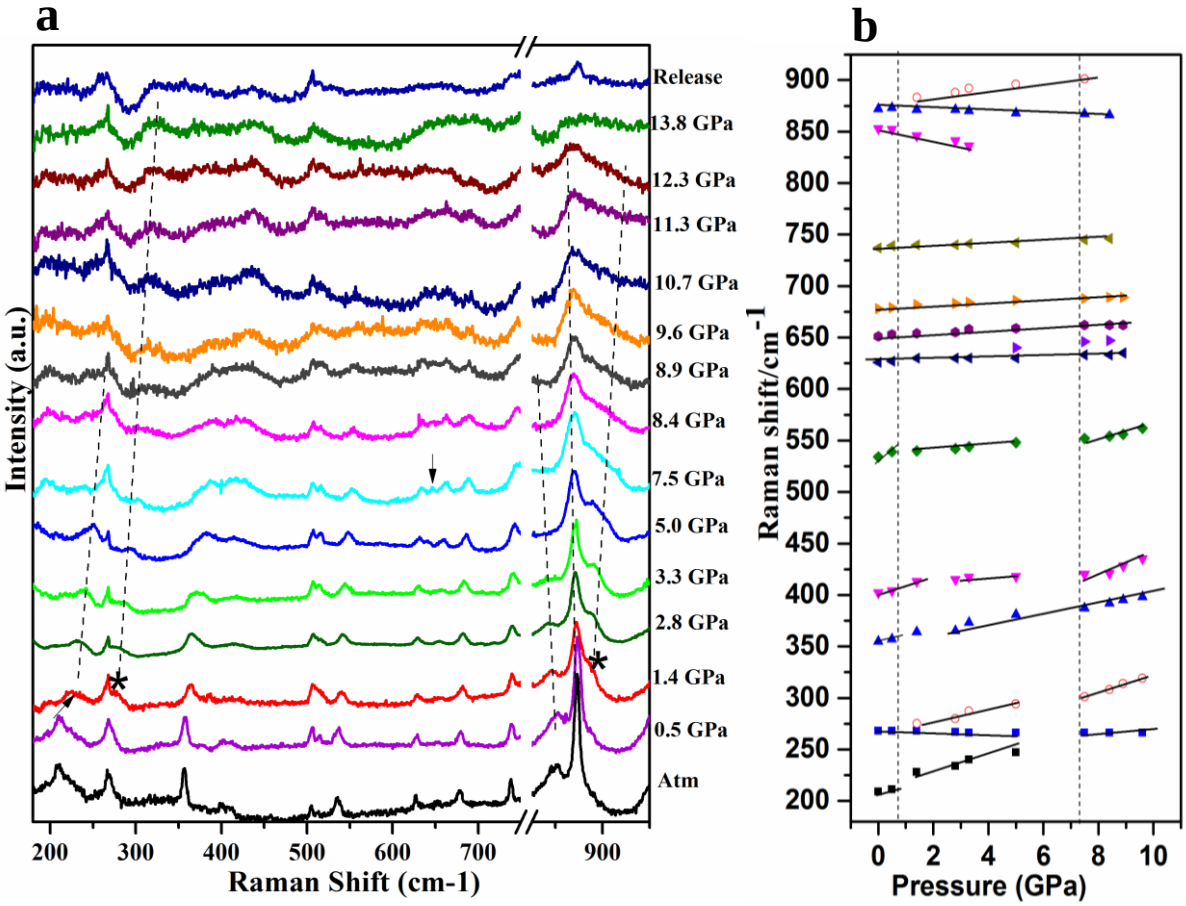

Figure 3.8. (a) Raman spectra of t-UCA in the pressure range atm to 13.8 GPa in spectral region 180-960 cm^{-1}, (b) Variation of Raman shift with pressure.

In this spectral region, several changes like discontinuous change in frequencies, appearance of new modes, broadening and disappearance of several modes are observed. As pressure is

increased, several Raman bands shift progressively towards higher frequencies accompanied by peak broadening. At 1.4 GPa, two new modes at 275 and 883 cm^{-1} appear and show blue shift upon further compression. Beyond 7.5 GPa, these modes show broadening and reduction in intensity. The Raman mode at 676 cm^{-1} due to δ CO_2^- (bending) is blue shifted and disappeared upon compression above 10.7 GPa. In addition to this, we have also observed a new mode at 640 cm^{-1}(marked as ↓) above 5 GPa. In contrast, two modes at 872 and 850 cm^{-1} attributed to ν C-CO_2^- and twist C=C (ethylenic) show red-shift (softening) upon increasing the pressure up to 13.8 GPa. The 850 cm^{-1} mode could not be traced beyond a certain pressure due to the merging of this mode with Moissanite band. On release to ambient pressure, new Raman modes along with the modes of the ambient phase were observed in the Raman spectrum.

SPECTRAL REGION 970-1800 cm^{-1}

Figure 3.9 (a) represents the pressure induced evolution of Raman spectra of t-UCA up to 13.8 GPa in 970-1800 cm^{-1} spectral region. The pressure dependence of selected Raman modes of t-UCA in this frequency range is depicted in Figure 3.9 (b). It is observed that the strong Raman mode at 1664 cm^{-1} due to ν C=C (ethylenic) at ambient pressure shows stiffening and continuously shifted toward higher frequencies on compression. At 7.5 GPa, this mode is blue-shifted to 1693 cm^{-1}, and simultaneously a new mode starts appearing at 1667 cm^{-1} (marked as * and shown in the inset A of Figure 3.9). This new mode also shifts progressively towards higher frequency (shown with dotted line) along with increase in the intensity. At 7.5 GPa, a new weak mode at 1492 cm^{-1} appears whose intensity increases with pressure, similar to the new mode that appeared at 1667 cm^{-1}. The various modes associated with imidazole ring showed stiffening and a considerable decrease in intensity compared to acrylic modes which then disappeared after certain pressure.

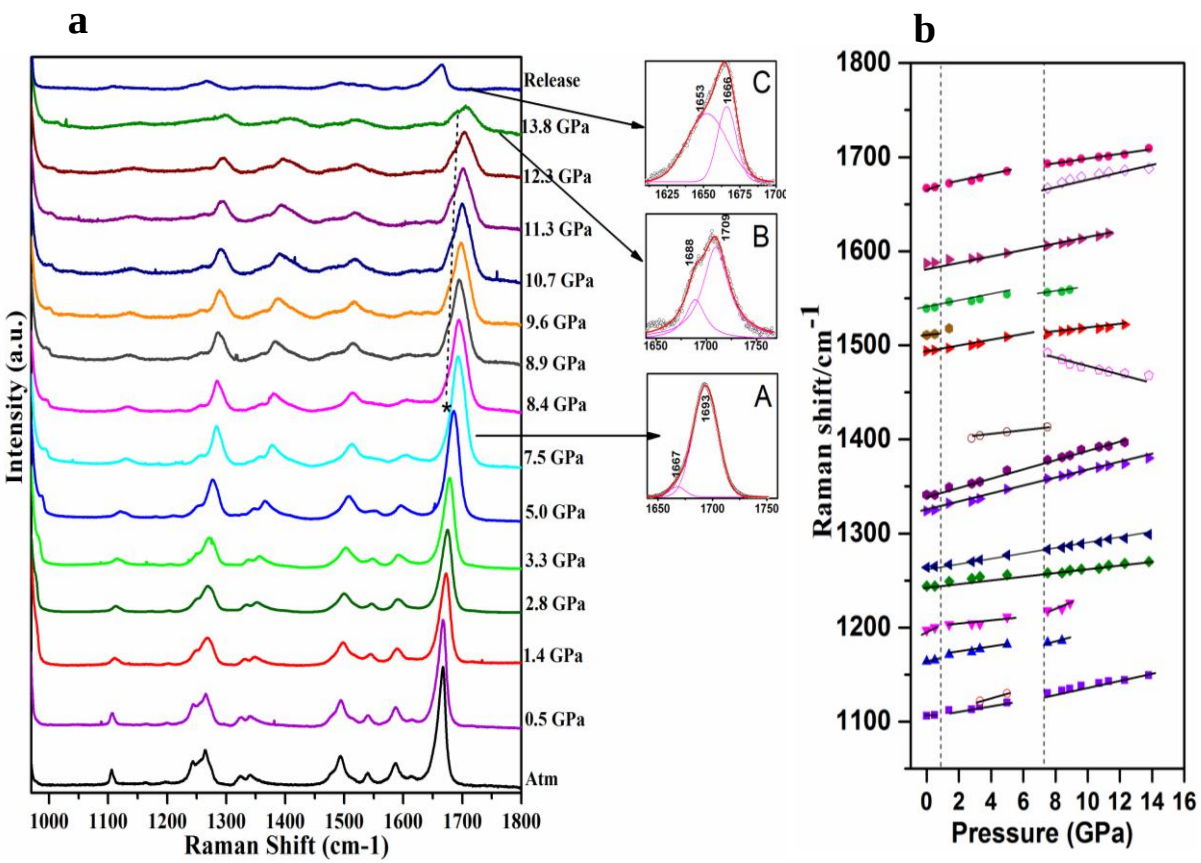

Figure 3.9. (a) Raman spectra of t-UCA in the pressure range atm to 13.8 GPa in spectral region 970-1800 cm^{-1}(inset shows the deconvoluted peaks at 7.5, 13.8 GPa and release), (b) Variation of Raman shift with pressure.

For example, mode at 1536 cm^{-1} due to ν C-N (stretch) showed stiffening and decrease in intensity with pressure followed by disappearance of the band beyond 8.4 GPa. Similar behaviour was also observed for the mode at 1584 cm^{-1} (ν C-N, δ C-H (Rg), δ N-H). Furthermore, the mode at 1322 cm^{-1} due to Rg breathing and δ C-H (Rg) gets stiffened upon compression. Beyond 8.4 GPa, a drastic reduction in the intensity followed by broadening are observed. The weak mode observed at 1104 cm^{-1} due to δ C-H (Rg) & δ N-H stiffen with the pressure. Modes due to in-plane bending (δ) C-H (1261 & 1337 cm^{-1}) of acrylic part of t-UCA continue to show their presence up to 13.8 GPa but with a decrease in their peak intensity. Both these modes also stiffen with pressure.

STECHING REGION 2850-3400 cm^{-1}

Figure 3.10 (a) depicts the pressure induced evolution of Raman spectra of t-UCA up to 8.9 GPa in 2850-3400 cm-1 spectral region and Figure 3.10 (b) shows the pressure dependence of the Raman modes. Since the C-H stretching modes of t-UCA were discernible only up to 8.4 GPa, high pressure Raman spectra in this region above 8.9 GPa are not included in the analysis.

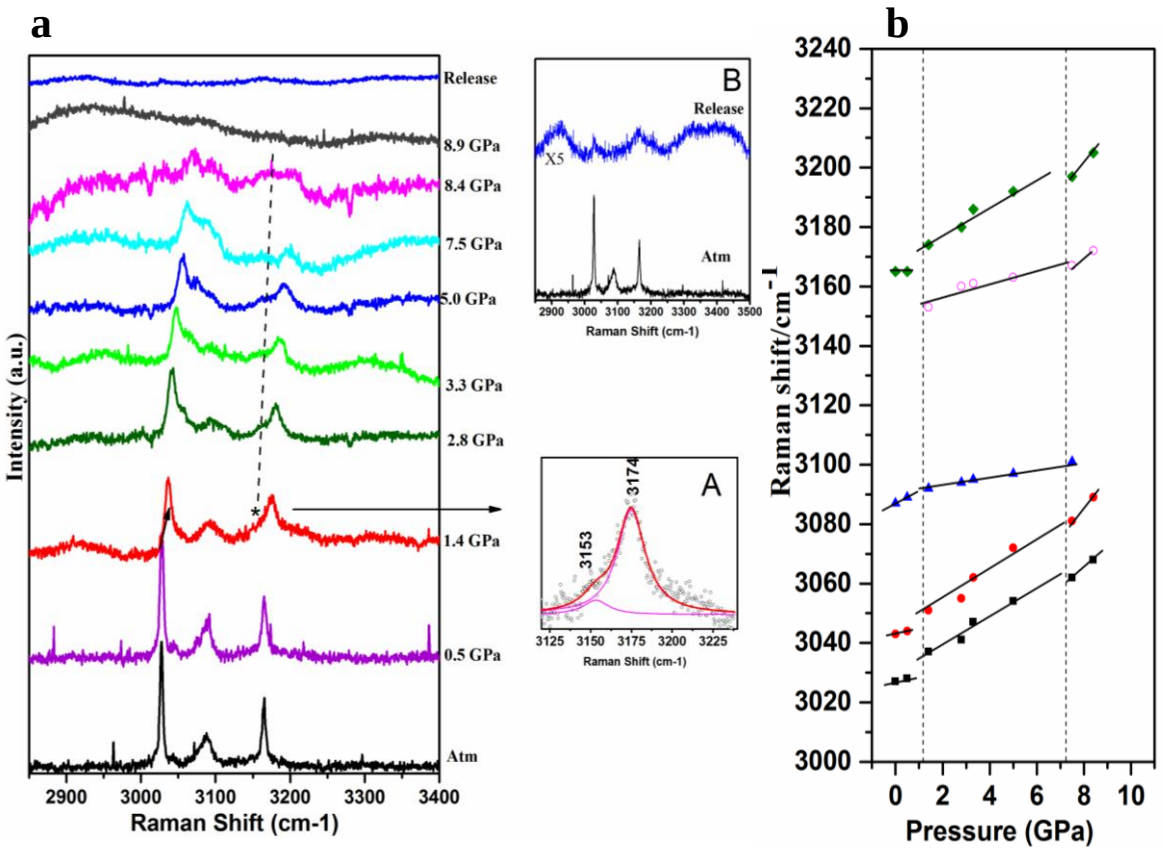

Figure 3.10. (a) Raman spectra of t-UCA in the pressure range atm to 8.9 GPa in spectral region 2850-3400 cm^{-1} (inset shows the deconvoluted peaks at 1.4 GPa and release), (b) Variation of Raman shift with pressure.

All the modes in this spectral region showed stiffening with increasing pressure and a discontinuous change in the frequency across 1.4 & 7.5 GPa. At 1.4 GPa, emergence of a new mode at 3153 cm^{-1} (shown in inset A of Figure 3.10) was observed. Beyond 1.4 GPa, the

intensity of Rg stretching modes (3165 & 3087 cm^{-1}) showed stiffening along with decrease in intensities which then led to broadening of the peaks. Beyond 8.4 GPa, none of the modes were observed except for a broad feature.

3.2.4. DISCUSSIONS

With increase in pressure, the relative intensity of C-H stretch modes of imidazole ring at 3087 & 3165 cm^{-1} is significantly reduced. Similar behaviour was also observed in the ring vibrations in the 970-1800 cm^{-1} spectral region. There was also a drastic reduction in the relative intensity of the ring C=C stretch (1614 cm^{-1}) and other ring modes (1241, 1322, 1491 & 1584 cm^{-1}). In addition, two new modes are observed at 3153 cm^{-1} (C-H stretch region) and 883 cm^{-1} at pressures above 1.4 GPa.

The above observations are signature of structural modification in imidazole ring of t-UCA across 1.4 GPa. The emergence of new mode in C-H stretching region is one of the key spectroscopic signatures of the onset of a possible solid state polymerization. The pressure induced polymerization of several molecular systems has been reported earlier [120-124]. For example, in the high pressure Raman studies of carnosine, a dipeptide of L-Histidine and β-alanine, pressure induced imidazole ring opening polymerization was reported based on the emergence of new C-H stretching mode accompanied by drastic reduction in the intensity of ring C=C mode and several other spectral changes across 11.7 GPa [120]. Benzene is also reported to polymerize at 21 GPa, which involved the opening of benzene ring leading to a highly cross-linked polymer [122].

In our study, a new Raman mode observed at 890 cm^{-1} can be attributed to C-C stretch arising due to the opening of imidazole ring. This is similar to the vibrational analysis of glycolide in solution phase, the glycolide ring opening leading to polymerization was confirmed from the emergence of a new Raman mode at 890 cm^{-1} attributed to C-C stretching

vibration, characteristic of glycolide ring-opening [189]. The peculiar spectral changes observed in the present study across 1.4 GPa, viz the discontinuous change in frequencies (Figure 3.10 (b)), emergence of new modes at 3153 cm^{-1} (C-H stretch) and 890 cm^{-1} (C-C stretch), reduction in the intensity of characteristic imidazole ring modes etc. can be associated to structural modifications linked to onset of ring opening polymerization of imidazole in t-UCA. On further compression beyond 8.4 GPa, the spectrum showed a broad feature in the CH region. On release from 13.8 GPa to ambient pressure, the spectrum of the retrieved sample contains the Raman modes of ambient as well as the polymeric phase which indicates that polymerization is not complete up to 13.8 GPa, in addition to the irreversible nature of the polymeric phase transition.

Simultaneously another interesting observation was noted in the 970-1800 cm^{-1} spectral region at 7.5 GPa, wherein a new mode at 1667 cm^{-1} appeared as a shoulder (inset A of Figure 3.9 (a)) of 1693 cm^{-1} band. Upon further compression, this above new mode is blue-shifted and gains intensity (Inset B of Figure 3.9). On release to ambient pressure, its peak position is observed at 1653 cm^{-1} (Inset C of Figure 3.9). The emergence of the new mode across 7.5 GPa can be attributed to the formation of new conformer, i.e cis form of UCA. The UCA molecule is known to have both trans and cis isomeric forms. Because of the strong, highly polarized nature of C=C acrylic bond, the Raman mode due to C=C stretch is considered as an important characteristic spectroscopic feature to identify the type of conformers [190]. The C=C stretch of cis conformers is known to be appeared at lower frequency when compared to the trans form. Bourguel et. al. [191] empirically established that the vibrational frequency associated with the C=C stretching mode in the Raman spectrum is lower (~15 cm^{-1}) in the cis than in the trans-form. For instance, Raman mode appeared at 1658 cm^{-1} in the spectrum of olefins, was assigned to C=C stretching mode of cis olefins, whereas the mode at 1670 cm^{-1} is assigned to trans-olefins [192, 193]. The

infrared band due to C=C stretching mode of trans and cis butadiene were observed at 1663 cm^{-1} and 1654 cm^{-1} respectively [194]. Indeed, two different Raman modes are also reported at 1658 and 1669 cm^{-1} for cis and trans forms of UCA respectively [195, 196]. Furthermore, the infrared spectra (low resolution) of trans and cis UCA showed bands due to C=C stretch at 1675 and 1663 cm^{-1} respectively [197].

In addition, we have also observed a new mode at 640 cm^{-1} (marked as arrow) above 5 GPa. This mode is assigned to δ CO_2^- of cis form of acrylic acid [198]. The above observations suggest that compression results in the conformational change of t-UCA into cis-UCA across 7.5 GPa. Pressure induced isomerization of various unsaturated compounds is also reported earlier [121, 182-185, 199-201]. At high pressure and room temperature, acetylene was transformed into trans-polyacetylene as a predominant product at around 3.5 GPa [201], whereas at high pressure and liquid nitrogen temperature, acetylene was transformed into cis-polyacetylene at around 12 GPa, which gets converted into trans form on warming up to room temperature [200]. In the high pressure Raman study of butadiene, the formation of pure trans-polybutadiene from butadiene was observed under the irradiation of 488 nm Ar^+ laser line. Maleic acid (cis form) is also reported to undergo isomerization to form fumaric acid (trans) at ~2 GPa [182]. Therefore, we suggest that across 7.5 GPa, the t-UCA is possibly transformed into the cis conformer, evidenced by the appearance of the above new modes (C=C stretch and δ CO_2) characteristics to cis-UCA. On release to ambient, the presence of C=C stretch mode due to cis-UCA in Raman spectrum suggest that the conformational transformation is irreversible.

Various mechanisms have been proposed through which a molecular system can undergo isomerization [202]. In some cases, the double bond character is reduced through resonance which facilitates the rotation around the double bond leading to isomerisation. In highly conjugated molecular systems, there is a dramatic decrease in the rotational energy

barrier which favours isomerisation. It is also observed that overcrowded systems are subjected to isomerism due to stereoelectronic effect [202]. Similarly, in the case of t-UCA under pressure, we believe that both increased conjugation of double bond due to the presence of imidazole ring and stereoelectronic effect facilitates the conversion of trans to cis isomer.

3.2.5. CONCLUSION

High pressure Raman Studies were carried on trans-urocanic acid (t-UCA) from ambient to 14GPa. The molecule comprises of imidazole ring and acrylic acid in the molecular structure. Our studies indicate that pressure initiates transformations of t-UCA to a polymeric state above 1.4 GPa and conversion of trans isomeric form to the cis form at further higher pressures above 5 GPa. Interestingly, these transformations have been found to be irreversible. The onset of ring opening polymerization of t-UCA involves the imidazole ring, which was inferred from the appearance of new Raman modes characteristic to ring opening and polymer form, and disappearance of characteristic ring modes. On release to ambient conditions, the presence of Raman modes of both the ambient t-UCA and polymer in the quenched sample indicate that the polymerization is irreversible and not completed up to ~14 GPa and the quenched sample contains the composite mixture of monomer and polymer.

On compression above 5 GPa, and emergence of a well discernible characteristic mode of cis-UCA (C=C stretch) at pressures near 7.5 GPa, indicate that some of t-UCA monomers undergoes conformational transformation and get converted into the cis form of UCA. The presence of C=C stretching mode, attributed to cis-UCA, in the Raman spectrum of retrieved sample implies that the conformational transformation is also irreversible.

CHAPTER 4.

PLASMON-INDUCED DIMERIZATION OF THIAZOLIDINE-2, 4-DIONE ON SILVER NANOPARTICLES

4.1. INTRODUCTION

As discussed in the section 1.1.1.2, besides the enhanced localized EM field present near the surface of metal NP which forms the basis of SERS, these metal NP can also initiate several chemical reactions on the surface of metal NP when illuminated with light of frequency of LSPR absorption band. Such reactions driven by excitation of LSPR are termed as plasmon-induced chemical reactions. The plasmon-driven chemical reactions lead to the formation of new molecules on the metal NP surface and the new molecules thus formed can be detected and identified by SERS from the appearance of its characteristic vibrational features.

Plasmon-driven surface catalyzed reactions have been gaining considerable attention following the discoveries of several reactions occurring on metal NP. In two separate SERS studies of *p*-aminothiophenol (*p* ATP) and p-nitrothiophenol (*p* NTP) molecules adsorbed on silver metal NP surface, chemical transformation of the molecules to a new surface species dimercaptoazobenzene (DMAB) was identified by the spectral changes observed during SERS measurement [68, 69, 203]. Similarly, studies on surface-catalyzed oxidation of 3-hydroxyanthranilic acid into an azo derivative and surface-catalyzed di-selenide formation from the selenol tautomer of selenourea were observed recently [204, 205]. Several plasmon-induced surface reactions including the dissociation of H_2, methylene blue and dimethyl disulfide molecules on metal NP surface have been reported [70-75, 77, 78, 206-217]. Recently, plasmon-induced reaction of *p*NTP adsorbed on Au NP showed the dissociation of *p*NTP to thiophenol at lower concentrations and dimerization of *p*NTP to DMAB (via N-N coupling) at higher concentrations [218]. Apart from the plasmon-induced N-N coupling reactions, surface-induced dimerization of rhodanine (Rd) involving C-C coupling (analogous to the Knovenagel reaction) on Ag NP surface was also reported [219].

The plasmon-induced chemical transformation of molecules can be explained by various excitation mechanisms [79, 81-83]. These mechanisms are the following: (1) Direct

intramolecular excitation mechanism, (2) Direct charge transfer mechanism, (3) Indirect hot-electron transfer mechanism wherein hot electrons generated from nonradiative decay of LSPR can trigger various chemical reactions in molecules adsorbed on metal NP [84-87], (4) Heat generated due to decay of the LSP resonance can also induce reactions in molecules. The detailed descriptions about the mechanism are provided in the section 1.1.1.2.

In this chapter, the SERS studies of thiazolidine-2, 4-dione (TZD) (structure shown in Scheme 4.1) using Ag NP sol as SERS substrate are described. TZD and its derivatives form a significant class of heterocyclic compounds having a wide range of pharmacological applications [135-140]. It acts as an inhibitor of corrosion of mild steels in acidic solution and also used as a brightener in the electroplating industry due to its ability to make chemical coordination with the metal surface [141, 142]. It is also known to undergo conventional Knoevenagel condensation reactions with aldehydes and ketones in the presence of a base catalyst resulting in the formation of unsaturated (C=C) ketonic products [143, 220]. We chose to study SERS on TZD to investigate if a similar type of condensation reaction can occur on the surface of Ag NP induced by plasmon. Interestingly, the results indicate dimer formation of TZD on Ag NP surface at higher concentrations of TZD ($>10^{-3}$M), supported by DFT calculations. However, at concentrations ranging from 10^{-4} to 10^{-6} M, the studies showed that TZD molecules get deprotonated and adsorbed on Ag NP surface without producing dimer. The proposed reaction mechanism is discussed and illustrated here. The NRS spectra of TZD solid and aqueous saturated solution and SERS spectra at different concentrations are presented and discussed. DFT calculations have aided in the assignment of both NRS and SERS spectra. The present SERS study is expected to pave the way to extend the research related to plasmon-driven reactions for the development of novel approach in organic synthesis.

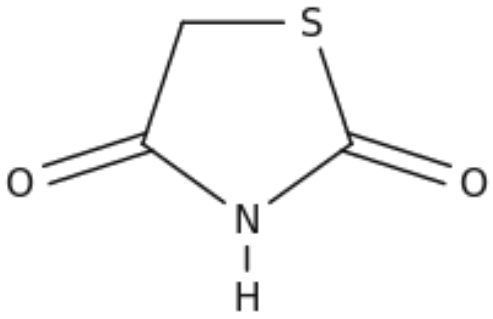

Scheme 4.1. Molecular structure of TZD.

4.2. EXPERIMENTS

The aqueous Ag NP sol was prepared according to Creighton et. al [146] as described in the section 2.3.4. The NRS spectrum of TZD in solid/aqueous solution/alkaline solution and SERS spectra were recorded using the 532 nm output from a solid state laser of ~15 mW power. For the Raman measurements, the sample solutions were taken in a standard 1×1 cm^2 quartz cuvette and the Raman scattered light was collected in a backscattered geometry and detected using a CCD based home built monochromator [144]. The entrance slit was kept at 50 μm, which gives a spectral band pass of 3 cm^{-1}. For the SERS measurements, solutions of different concentrations of TZD were mixed with Ag NP. A 1:1 volume ratio of Ag NP to aqueous solution of TZD was taken for SERS measurements. The SERS measurements were repeated to ensure reproducibility. Ag NP sol was characterized using a UV−visible absorption spectrophotometer (Shimadzu), and the size of Ag NP was determined using a JEOL 2000FX transmission electron microscope (TEM) operated at 160 kV.

4.3. COMPUTATIONAL DETAILS

In order to get insight into the experimental results, geometry optimization was carried out using DFT calculations for the tautomers of TZD, dimers of TZD and the silver complexes of

TZD and TZD dimer (E). The tautomers of TZD were optimized using the B3LYP functional and the aug-cc-pvdz basis set [165, 166]. For the E and Z tautomers of TZD dimer, the structural optimization was carried out using the 6-31+G* basis set. The Ag complexes of TZD and TZD dimer (E-form) were optimized using the DGDZVP basis set. All the calculations were carried out using Gaussian 03 program. No symmetry restriction was applied during geometry optimization. The vibrational frequencies were computed at the optimized geometries for the tautomers of TZD, dimers of TZD and the Ag complexes of TZD and its dimer (E-form) to ensure that they correspond to local minima on the potential energy surface and not to saddle points. The computed vibrations of optimized geometries of TZD and its Ag complex were multiplied by 0.98 and compared with the experimental frequencies. The computed vibrations of the optimized geometries of dimer were multiplied by a scaling factor of 0.94 and then compared with the SERS spectra.

TZD exists in fives tautomeric forms: thiazolidine (diketo) , thiazoline (oxo-enol), and thiazole (dienol) [221, 222]. The optimised geometries of all the tautomeric forms were calculated and are shown in Figure 4.1(a)-(e). The diketo form shown in (Figure 4.1 (a)), is the most stable form and the relative stabilities of the tautomers are given in Table 4.1. Both the crystallographic study and the theoretical investigation showed that the most stable and predominant form of TZD is diketo form [221, 223]. The calculated optimized geometrical parameters for the diketo form in the present study compares well with the available crystallographic experimental data and is shown in Table 4.2. The HOMO-LUMO transition energy of TZD was calculated with TD-DFT method using the B3LYP functional with aug-cc-pvdz basis set. In order to study the influence of Ag on the HOMO-LUMO transition energy, TD-DFT calculations were carried out for the Ag complexes of TZD with LANL2DZ basis set for Ag.

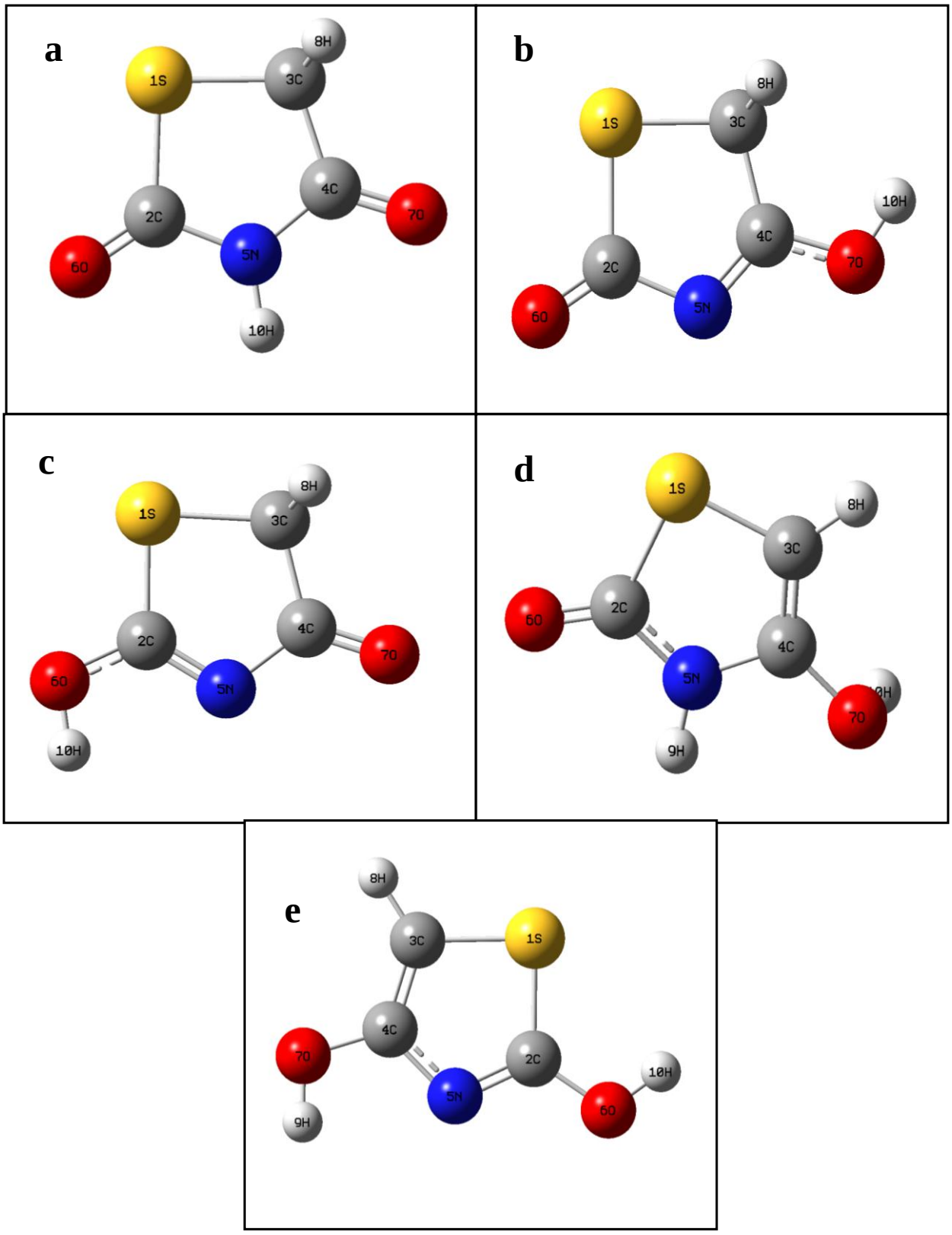

Figure 4.1. Optimized structure of (a) diketo (b), (c), (d) oxo-enol (e) di-enol forms of TZD.

Table 4.1. Calculated Relative stabilities (kcal/mol) of TZD tautomers.

Tautomeric forms				
a	b	c	d	e
0.0	19.06	17.30	31.85	29.82

Table 4.2. Comparison of molecular parameters of TZD molecule with available crystallographic data.

Calculated ***Bond length (Å)***		**Ref [221, 223]**
S(1)-C(2)	1.798	1.751
S(1)-C(3)	1.858	1.845
O(6)-C(2)	1.207	1.209
O(7)-C(4)	1.213	1.219
N(5)-C(2)	1.394	1.372
N(5)-C(4)	1.383	1.373
C(4)-C(3)	1.526	1.547
Calculated ***Bond Angle (Degree)***		
C(3)-S(1)-C(2)	92.2	94.2
C(4)-N(5)-C(2)	119.7	117.5
S(1)-C(2)-O(6)	125.4	124.9
S(1)-C(2)-N(5)	109.5	111.2
O(6)-C(2)-N(5)	125.1	123.9
O(7)-C(4)-N(5)	124.7	122.7
O(7)-C(4)-C(3)	124.6	123.7

4.4. RESULTS AND DISCUSSION

4.4.1. UV-VISIBLE ABSORPTION AND TEM MEASUREMENT

UV−visible absorption spectra of the aqueous solution of TZD, Ag NP sol and Ag NP sol mixed with TZD are shown in Figure 4.2A. The absorption spectrum of aqueous solution of TZD (Figure 4.2A (a)) showed a band at 230 nm (5.39 eV) due to HOMO-LUMO transition of TZD. The TD-DFT calculation also showed the HOMO-LUMO transition band at 229 nm (~5.39 eV) and is similar to reported values [224]. The absorption spectrum of Ag NP sol (Figure 4.2A (b)) showed a single sharp molar extinction maximum at 395 nm due to LSPR absorption. On addition of TZD to the Ag NP sol, the absorption spectrum (Figure 4.2A (c)) showed a second band at about 560 nm with a decrease in the absorbance of the 390 nm band.

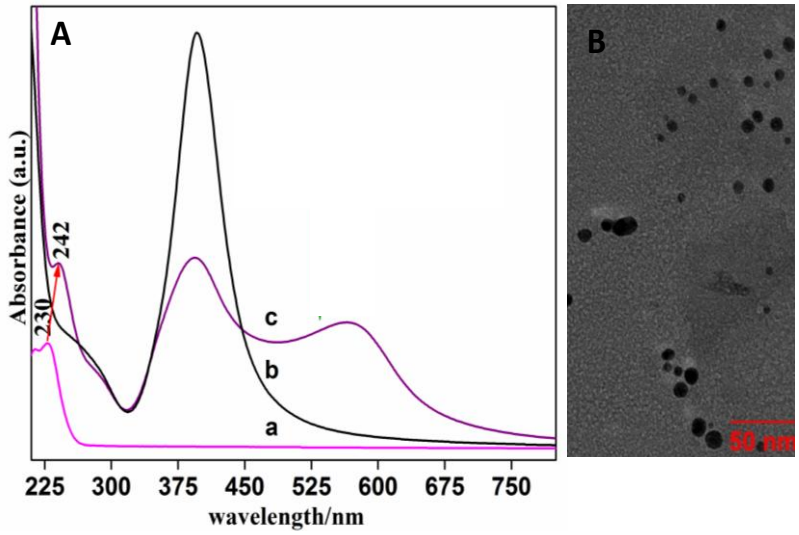

Figure 4.2. (A) UV-visible absorption spectra (a) aqueous solution of TZD, (b) Ag NP sol, and (c) TZD mixed with Ag NP sol, (B) TEM image of Ag NP.

The appearance of the red shifted LSPR band at 560 nm has been attributed to the aggregation of Ag NP induced by the molecules of TZD. Aggregation of Ag NP sol in the presence of adsorbate is reported earlier [146, 172]. The absorption band at 230 nm (Figure

4.2A (a)) due to the HOMO-LUMO transition of TZD is red-shifted to 242 nm (5.12 eV) (Figure 4.2A (c)) which indicates a weak chemical interaction of TZD with metal. TEM analysis of Ag NP shows an average diameter of 10 nm and is shown in Figure 4.2B.

4.4.2. NRS SPECTRA OF TZD

The NRS spectra of TZD powder and its aqueous solution (0.1M) are shown in Figure 4.3 (a) & (b) respectively. The observed Raman bands in the NRS spectra are assigned on the basis of the calculated spectra of diketo form of TZD, the predominant form, as discussed under computational details and the assignments are tabulated in Table 4.3. From Figure 4.3 (a) & (b), it can be seen that the spectra of TZD powder and its saturated solution are almost similar except for the few changes in the position of some Raman bands.

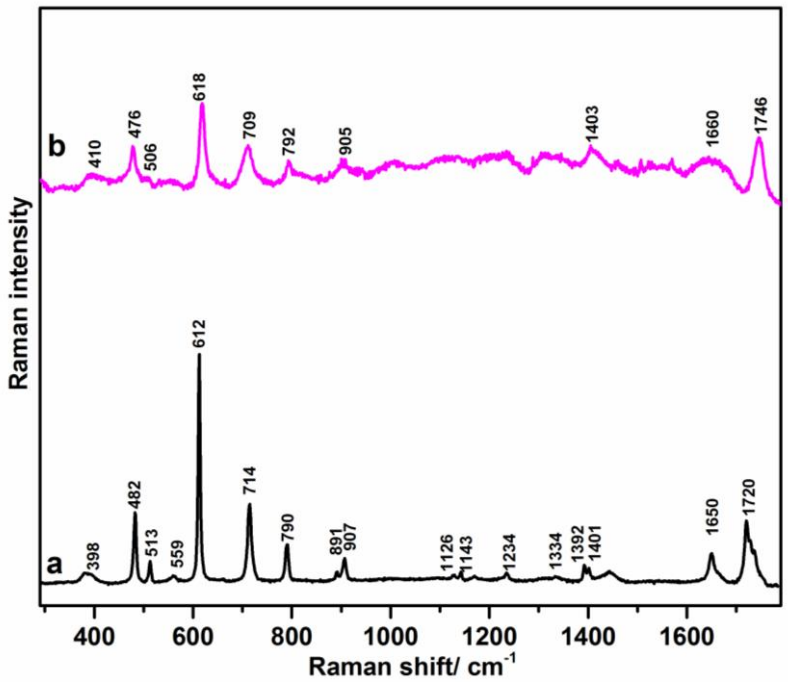

Figure 4.3. (a) NRS spectrum of TZD solid and (b) aqueous solution of TZD (0.1 M).

In the NRS spectra of TZD solid, the strongest band at 612 (618) cm^{-1} is assigned to in phase δ C4-N5-C2. The frequencies of TZD in solution are given in the parentheses. A few medium

Table 4.3. Assignments of Normal Raman (solid and solution) and SERS spectral bands of TZD in cm^{-1}.

Exp. TZD solid	**Exp. TZD Solution (0.1M)**	**Calc. TZD**	**Assignments**	**SERS (10^{-4}M)**	**Calc. TZD anion-Ag**	**Assignment**
1720 m	1746 m	1817	ν C2=O6, ν C4=O7			
1650 m	1660 m	1779	ν C2=O6, ν C4=O7, δ N5-H	1654 w	1782	ν C4=O7
1401 w	1403	1434	Sci CH2	1397 m	1469	Sci CH2
1392 w		1380	δ N5-H			
1334 w		1317	δ C4-N5-C2, δ N5-H, ν C2-N5	1346 m	1325	ν N5=C4
1234 w		1229	ω CH2	1255 m	1242	ω CH2, ν N5=C4
1143 w		1141	ν C2-N5, δ N5-H, ω CH2	1198 w	1207	ν N5=C2, ω CH2,
1126 w		1131	t CH2	1126 w	1134	t CH2
907 w	905 vw	900	r CH2	940 vw	921	r CH2
891 w		885	ν C3-C4	900 vw	886	ν C3-C4
790 m	792 w	772	ν C3-S	790 vw	792	ν C3-S
714 m	709 m	677	ν C2-S	750 s	658	ν C2-S
612 s	618 s	604	δ C4-N5-C2	640 s	626	δ C4-N5-C2
513 w	506 vw	551	γ N5-H, r CH2, γ N5-C4-O7	539 w	584	r CH2, γ N5-C4-O7
482 m	476 m	493	δ C3-S1-C2	486 w	507	δ C3-S1-C2
398 w	410 w	460	δ O7-C4-C3	420 s	440	δ O7-C4-C3

ν: stretch; sci: scissoring; ω: wagging; t: twist; r: rock; δ: in plane bend; γ: out of plane bend; s: strong; m: medium; w: weak

intensity bands are observed at 1720 (1746), 1650 (1660), 790 (792), 714 (709) & 482 (476) cm^{-1}. Of these modes, the modes at 1720 (1746) & 1650 (1660) cm^{-1} are assigned to ν C2=O6 & ν C4=O7 and the bands at 790 (792) & 714 (709) cm^{-1} are attributed to ν C3-S and ν C2-S respectively. Details of few weak observed bands at 1401 (1403), 1392, 1334, 1234, 907 (905), 891, 559, 513 (506) and 398 (410) cm^{-1} and their assignments are presented in Table 4.3. The presence of vibrational modes due to CH_2, N-H and both the C=O groups also confirms that the molecules exist in diketo form in solid/solution phase.

4.4.3. CONCENTRATION-DEPENDENT SERS SPECTRA OF TZD AND INTERPRETATION

SERS spectra of TZD in the concentration range (10^{-6} to 10^{-1}M) are presented in Figure 4.4 and the assignments of vibrational bands are given in Table 4.3 and Table 4.4. The spectral features (peak positions) observed at 10^{-6}M is almost identical up to the concentration of 10^{-4}M and resemble more the NRS spectrum of solid/solution. New peaks start emerging at 10^{-4}M and grow in intensity for concentrations 10^{-3}M and above. The noteworthy feature in the SERS spectrum at concentrations ≥10^{-3}M is the appearance of a strong band at 1566 cm^{-1} which towers over all other bands. At the outset, it is very obvious that appearance of new strong peak is attributed to the formation of new surface species that is different from the one adsorbed at lower concentrations. The results and discussion of the SERS spectra of lower (10^{-4}, 10^{-5} and 10^{-6}M) and higher (10^{-3}, 10^{-2} and 10^{-1}M) concentrations of TZD and the nature of the surface species are discussed below.

Table 4.4. Assignments of SERS spectral bands (TZD dimer) in cm^{-1}.

SERS (0.1M)	**Calc. Dimer**	**Calc. Dimer with Ag**	**Assignment**
1746 w	1712	1710	ν C11=O15, ν C2=O6
1668 w	1702	1701	ν C11=O15, ν C2=O6
1650 w	1643	1643	ν C13=O14, δ N12-H, ν C4=C9
1566 vs	1567	1564	ν C4=C9, δ N5-H, ν C13=O14, ω CH_2
1460 vw	1404	1390	Sci CH_2
1364 vw	1348	1342	δ N5-H, ν C4-N5, Sci CH_2
1312 w	1305	1291	δ N12-H
1266 vw	1274	1265	δ N5-H, δ C9-C4-N5
1231 vw	1252	1248	δ C13-N12-C11, δ N12-H, δ N5-H
1181 vw	1205	1206	ω CH_2
1110 vw	1089	1095	t CH_2
1004 w	982	980	δ C4-C9-C13, δ N12-H, ν C13-N12
960	926	925	ν C3-C4, δ N5-H
905 w	870	863	r CH_2
792 w	776	774	δ C4-C3-S1, δ C4-N5-C2
750w	711	718	γ N5-H, Rg torsion
707 w	710	710	ν C3-S1, δ N12-H
637 w	684	671	γ N5-H, γ C9-C13-O14
617 w	625	626	ν C2-S1, ν C11-S10
557 vw	554	546	γ N12-H
508 w	548	545	Rg bend
450 m	500	505	γ C9=C4, r CH_2, γ N12-H
ν: stretch; sci: scissoring; ω: wagging; t: twist; r: rock; δ: in plane bend; γ: out of plane bend; s: strong; m: medium; w: weak; Rg: ring			

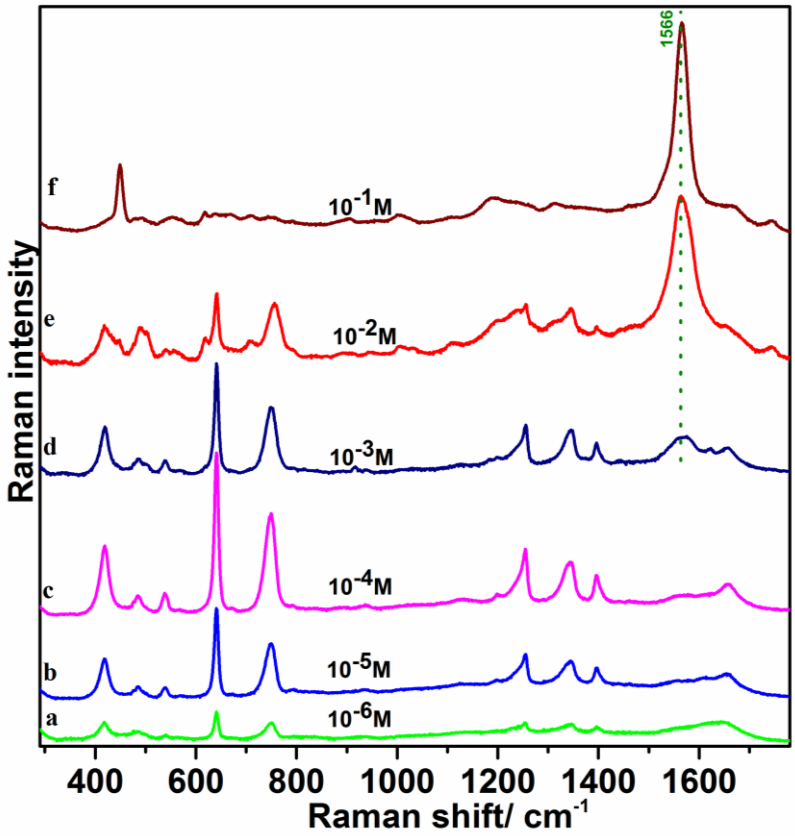

Figure 4.4. SERS spectra of TZD at different concentrations (10^{-6}M - 10^{-1}M).

4.4.3.1. SERS ANALYSIS OF TZD AT LOWER CONCENTRATIONS-EVIDENCE OF DEPROTONATION

The SERS spectrum of TZD at 10^{-4} M concentration is compared with NRS spectrum of TZD solution and shown in Figure 4.5 (a & b). In the NRS spectrum of TZD solution (Figure 4.5 a), the vibrational bands due to ν C=O are observed at 1746 and 1660 cm^{-1}, whereas only one vibrational band at 1654 cm^{-1} is observed in the SERS spectrum (Figure 4.5 b). The band due to γ N-H is seen at 506 cm^{-1} in NRS spectrum of solution, whereas no vibrational mode due to γ N-H is observed at or near the position of 506 cm^{-1} in the SERS spectrum. The presence of only one ν C=O and the absence of γ N-H modes in the SERS spectrum implies that the molecule adsorbed on the surface of Ag NP is not the diketo form of TZD. It is likely that on the Ag NP surface, TZD loses its proton from N-H (deprotonation) and the resulting anion

gets resonance stabilized leading to the formation of enolate forms (B & C) which have only one C=O as shown in Scheme 4.2 [225]. These enolate forms of TZD get adsorbed onto Ag NP surface which explains the absence of γN-H and the presence of only one ν C=O band in the SERS spectrum. In order to ascertain the above observation, NRS spectrum of TZD in alkaline solution, where TZD is known to be present in the deprotonated form (pK_a~ 6.7), was recorded and shown in Figure 4.5 c. The absence of the ν C=O band at 1746 cm^{-1} (marked black dotted line) in the spectrum implies that the TZD is present as enolate anion species formed after the deprotonation as discussed in Scheme 4.2. The above result corroborates the presence of deprotonated TZD in the enolate form on the surface of Ag NP. The calculated NRS spectrum of deprotonated TZD along with the NRS spectrum of TZD is shown in Figure 4.6. The SERS bands are assigned with the help of the calculated Raman spectrum of the optimized geometry of silver complex of TZD anion (B) (Figure 4.7) since form B is found to be more stable than form C [225]. Their assignments are tabulated in Table 4.3. The strong band observed at 618 cm^{-1} assigned to δ C4-N5-C2 in the NRS spectrum of aqueous solution of TZD (Figure 4.5 (a)) is seen at 640 cm^{-1} in both the SERS and NRS spectra of TZD in alkaline solution. The ν C=O band observed at 1654 cm^{-1} in the SERS spectrum is red-shifted by 11 cm^{-1} when compared with NRS spectrum of TZD alkaline solution, which indicates that the C=O group interacts directly with the metal surface. In the SERS spectra, a new low frequency band at 230 cm^{-1}(shown in the inset of Figure 4.5) due to metal adsorbate stretching, was observed which provides strong evidence for the interaction of TZD with the silver surface. The SERS spectrum showed several prominent bands at 420 cm^{-1} (δ O7-C4-C3) & 750 cm^{-1} (ν C2-S). Of these vibrations, the band due to ν C2-S is blue shifted by 38 cm^{-1} when compared with NRS spectra of TZD in alkaline solution. Similarly, the band arising from δ O7-C4-C3 vibration is also blue shifted to 420 cm^{-1} compared to 410 cm^{-1} in the NRS spectrum of solution. Several vibrational

modes, weak in the NRS spectrum became strong and noticeable in SERS spectra and were observed at 1255 (ω CH_2), 1346 (ν N5=C4) & 1397 cm^{-1} (δ CH_2).

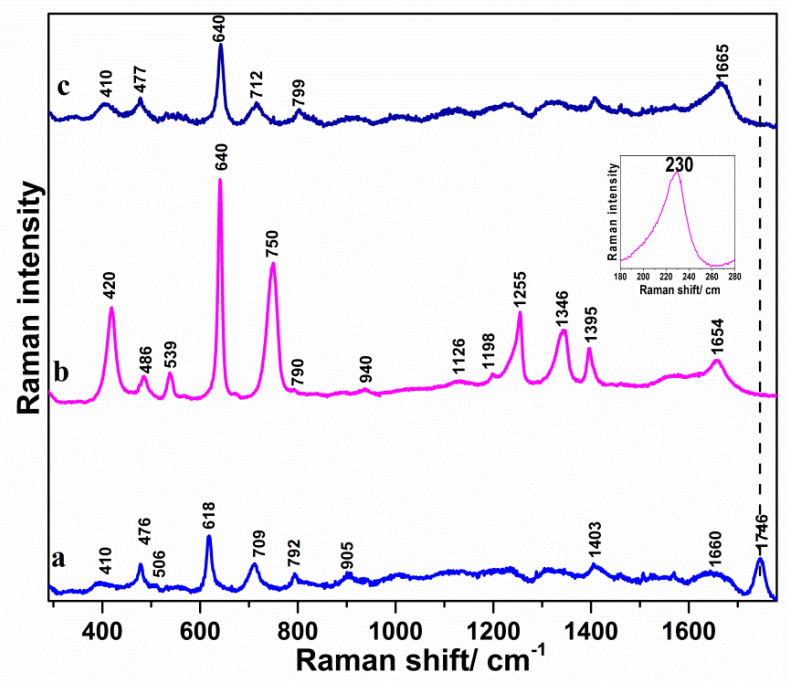

Figure 4.5. (a) NRS spectrum of aqueous solution of TZD (0.1M), (b) SERS spectrum (10^{-4}M) and (c) NRS spectrum of alkaline solution of TZD (0.1M).

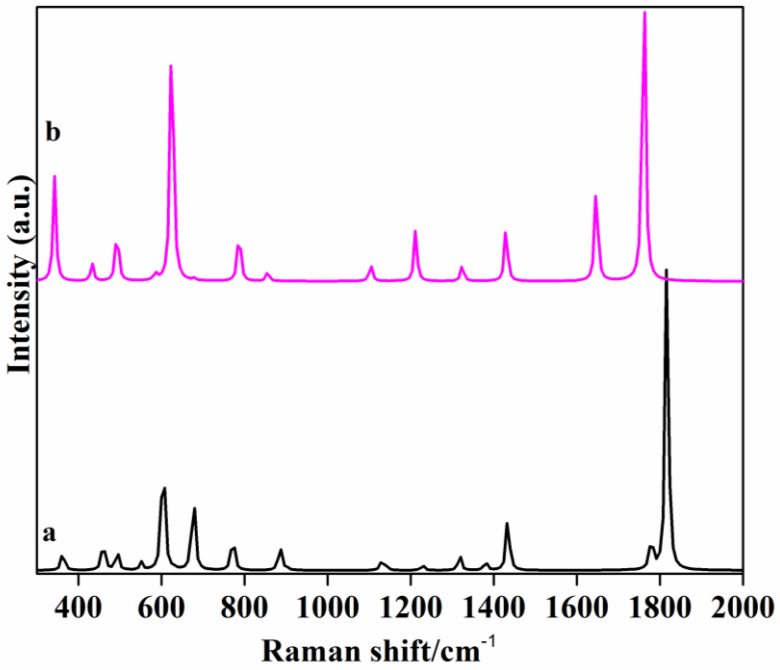

Figure 4.6. (a) Calculated Raman spectra of TZD and (b) calculated Raman spectra of TZD anion.

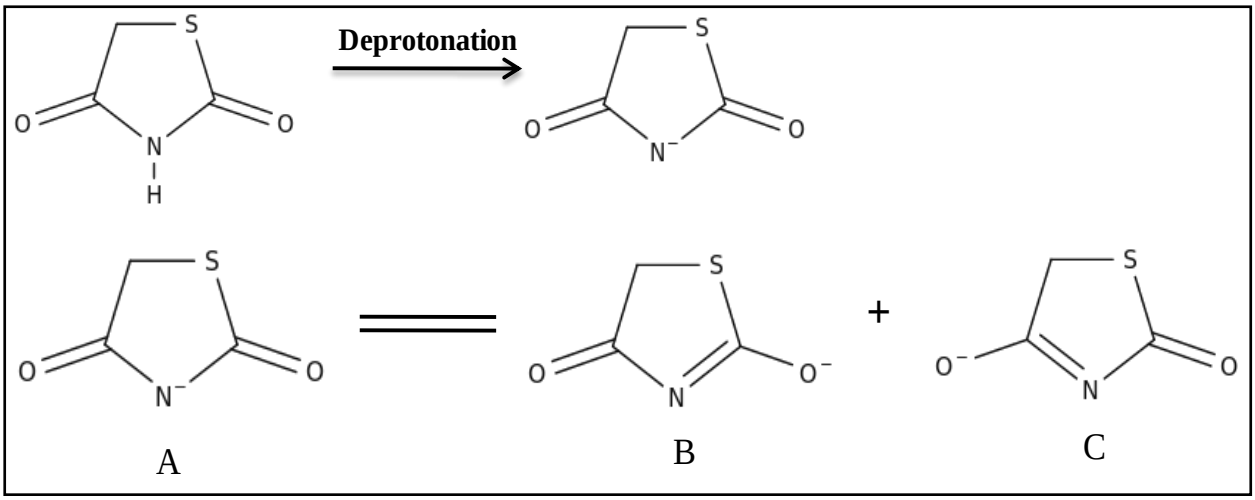

Scheme 4.2. Deprotonation and resonance structures of TZD anion.

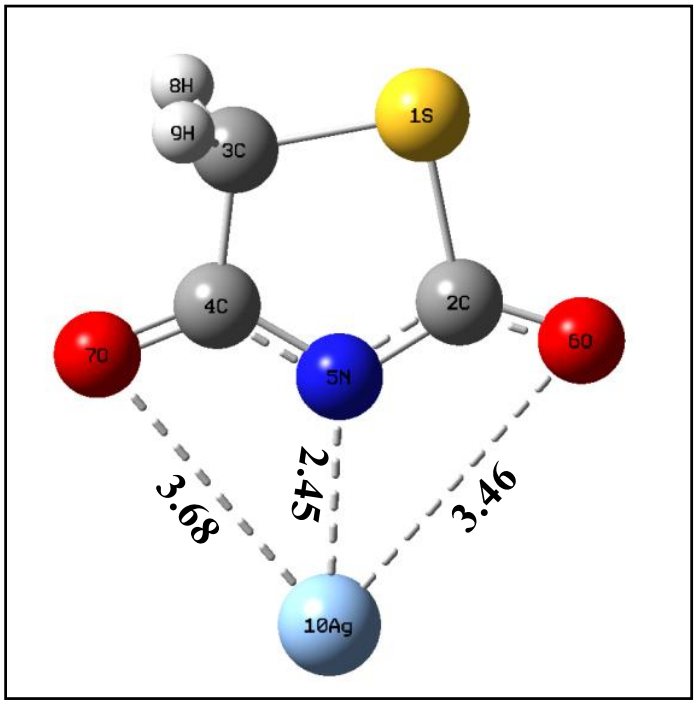

Figure 4.7. Optimized structure of TZD-Ag complex.

The shift and change in relative intensity in the SERS spectrum are known to arise due to both chemical and electromagnetic effects [56]. From the study of SERS spectra of TZD at lower concentrations, it has been inferred that TZD undergoes deprotonation and gets adsorbed predominantly as TZD anion (B) on the Ag NP surface.

4.4.3.2. SERS ANALYSIS OF TZD AT HIGHER CONCENTRATIONS: EVIDENCE OF TZD DIMERIZATION

In the SERS spectra of TZD at higher concentrations (Figure 4.4 d, e, f), among several new peaks, a strong peak at 1566 cm^{-1} (marked as green dotted line) appears and becomes intense at concentration of 0.1M. It is to be noted here that there are no peaks at or near the position of 1566 cm^{-1} in the NRS spectra of TZD solid/solution, and therefore, the above observation indicates that TZD molecules get transformed into new surface species on Ag NP surface. It is known that several TZD derivatives prepared by Knoevenagel reaction have vibrational bands in the spectral range 1560-1580 cm^{-1} which are attributed to ν C=C [226]. The Knoevenagel reaction of malononitrile with *p*-nitrobenzaldehyde was studied using X-ray diffraction and Raman spectroscopy, and a new strong Raman mode observed at 1580 cm^{-1} was assigned to the ν C=C band of the reaction product [227]. In the SERS study of Rd molecules, whose molecular structure is similar to that of TZD (one C=O of Rd is replaced by C=S), Rd is reported to undergo nanoparticle surface-induced self condensation reaction (analogous to the Knoevenagel reaction) resulting in the formation of a dimeric species via the active methylene group [219]. A strong band at 1566 cm^{-1} was reported and assigned to the ν C=C of the Rd dimer. The conventional Knoevenagel reaction is induced by the abstraction of a proton from the active methylene group by a base catalyst, and the nucleophile (carbanion formed) adds on to the carbonyl group of another molecule followed by dehydration to yield the dimer. TZD has an active methylene group bridged between C=O groups and hence a potential molecule to undergo conventional Knoevenagel reaction. Hence, it is possible that the strong band observed at 1566 cm^{-1} in the SERS spectra could be due to ν C=C of the TZD dimer formed via plasmon-induced dimerization.

In order to arrive at the most probable excitation mechanism involved in the plasmon-induced dimerization reaction among the various mechanisms discussed in the literature [79,

81-83], parameters such as the HOMO-LUMO energy of TZD with and without Ag NP, laser wavelength and LSP resonance absorption of Ag NP are considered. From the UV-visible absorption spectrum (Figure 4.2A (a)), a band corresponding to HOMO-LUMO transition energy of TZD molecule was observed at 230 nm (5.39 eV) and the same was also obtained from TD-DFT calculation. However, UV-visible absorption spectrum of TZD mixed with Ag NP sol (Figure 4.2 A (c)) showed a red-shifted band at 242 nm, while the calculated value for HOMO-LUMO transition energy for TZD-Ag_4 cluster was obtained at 797 nm (1.55eV). The possibility of various mechanisms leading to plasmon-induced dimerization is analyzed and discussed below.

Since the HOMO-LUMO energy of TZD is 230 nm (5.39 eV) and the energy of the incident laser used in the study is 532 nm, it is very unlikely that the dimerization reaction proceeds via the intramolecular excitation mechanism because the above mechanism is only favoured when the incident energy of the photon matches the HOMO-LUMO energy gap of the molecule.

The direct charge transfer mechanism requires excitation of LSP resonance with the incident laser wavelength and also an energy match between LSP resonance and the HOMO-LUMO energy gap of hybridized states of metal and molecule so that electrons get resonantly transferred from the metal to molecule hybridized states. Literature reports have shown various chemical reactions driven by direct electron transfer mechanism such as visible light induced oxidation of CO on Pt NP [217] and photodissociation of dimethyl sulphide [72] on metal NP surface. A strong hybridization between molecules and metal reduces the HOMO-LUMO energy gap from UV to the visible region which can match with the LSP resonance of the metal NP. In both cases, the reactions were reported to occur through direct electron excitation from the newly formed hybridized metal and adsorbate states by irradiation with visible light. A new peak at 470 nm in the absorption spectrum was observed which suggests

the formation of newly metal hybridized states of the molecule due to chemisorption of CO on Pt NP. Similarly, the dissociation of dimethyl sulfide without NP was found to occur using 248 nm (~5.0 eV) light, whereas on NP surface the dissociation occurred through visible light (532 nm). Hence, the direct electron transfer mechanism requires the energy match of incident light with transition energy between hybridized states. In the case of TZD, the TD-DFT calculation of TZD-Ag_4 cluster shows HOMO-LUMO energy value of 797 nm (1.55 eV) but the UV-visible spectrum (Figure 4.2 A(c)) of TZD mixed with Ag NP sol shows a band at 242 nm (5.12 eV). The difference in the values suggest that TZD actually interacts weakly with Ag NP, while TD-DFT calculation takes into account a strong chemical interaction between TZD and the Ag cluster to form newly hybridized molecule–metal states having HOMO-LUMO transition energy at 797 nm (1.55 eV). The incident laser wavelength, 532 nm, is away from the HOMO-LUMO gap of TZD in the presence of Ag NP (242 nm) which therefore cannot proceed through the above mechanism.

The role of plasmon heating in the dimerization of TZD is also investigated. It is known that the resonant oscillation of surface electrons can result in heat generation and eventually increase the NP temperature and Baffou et al.[87] have reported an increase in temperature (δT_{NP}) ~ 5K for gold NP (20 nm) dispersed in water when illuminated with 532 nm green laser (1 mW/μm^2). We have used the analytical expression given by Baffou et al. [87] to calculate δT_{NP} of spherical Ag NP dispersed in water when illuminated with 532 nm laser. The laser intensity I (power per unit area~0.75 mW/μm^2), R (radius of Ag NP~5 nm), and conductivity of water κ (0.6 W m^{-1} K^{-1}) was considered and δT_{NP} was found to be ~15 K. In order to investigate if dimerization can be induced due to local heating arising from plasmon, the aqueous solution of TZD (0.1M) was heated to a higher temperature ~70^oC and the NRS spectrum was recorded (shown in the Figure 4.8). The NRS spectrum did not show the dimer peaks but matched well with the NRS spectrum of the TZD solution at room

temperature (Figure 4.3b). Hence, local heating from plasmon alone could not have initiated the dimerization reaction of TZD. Recently, Keller et al.[228] presented the evidence produced by the ultrafast nanoscale Raman thermometry technique that the dimerization of *p*NTP molecule into DMAB is not thermally driven. They showed that the temperature of adsorbate increases only few tens of kelvin and the energy deposited into molecular adsorbates depletes very rapidly within few picoseconds.

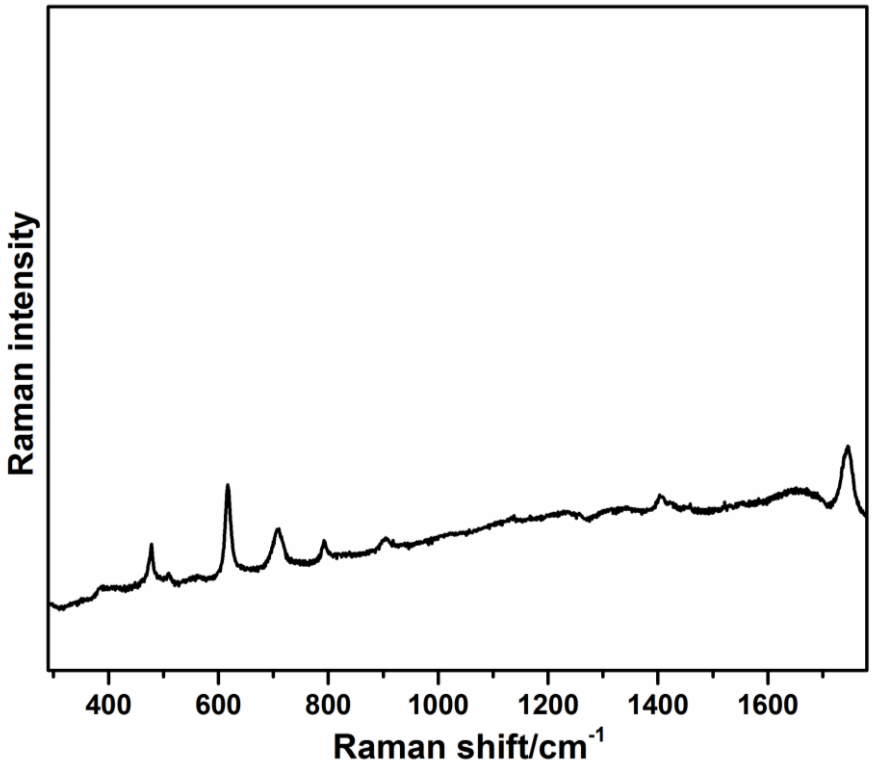

Figure 4.8. NRS spectrum of aqueous solution of TZD (0.1M) heated up to ~70^{o}C.

The indirect hot-electron-transfer mechanism has been used as dominant mechanism to explain several surface plasmon reactions including dimerization of *p*NTP [70, 215, 216, 218]. The above mechanism is favourable when the energy of the incident photon is in resonance with the absorption band of the metal NP and with the HOMO-LUMO transition energy being close to the Fermi energy of metals [81]. As discussed in the introduction, nonradiative decay of the LSPR generates hot electrons and these hot electrons lose their energy via electron–electron scattering until the electron gas approaches a non-equilibrium

Fermi–Dirac distribution with energy ranging between E_f (Fermi level of metal) and $E_f + h\nu$ [84-87]. In the present study, the hot electrons generated from the nonradiative decay of the LSPR of Ag can have energies ranging between the vacuum energy and the Fermi level (~5.5 eV) [84, 218], which is close to HOMO-LUMO transition energy of 230 nm (5.39 eV) of TZD molecule. As a result, there is a greater feasibility of hot electrons getting injected into the LUMO of the molecule by an inelastic electron tunneling (IET) process [81] forming TZD radical anion I as shown in proposed reaction mechanism in Scheme 4.3. TZD radical anion I further dissociates into TZD anion II along with generation of a neutral hydrogen radical (H^0). The formation of adsorbate ion along with the generation of H^0 by hot electrons has been reported [229]. Analogous to the Knovenagel reaction, the TZD anion adds to the carbonyl group of a nearby TZD molecule to produce the dimer after losing water. The local heating from the plasmon decay at the metal surface aids in the removal of water. Therefore, the indirect hot electron transfer can be considered as the one of the plausible mechanisms involved in plasmon-induced dimerization of TZD. Scheme 4.3shows the proposed reaction mechanism leading to TZD dimer.

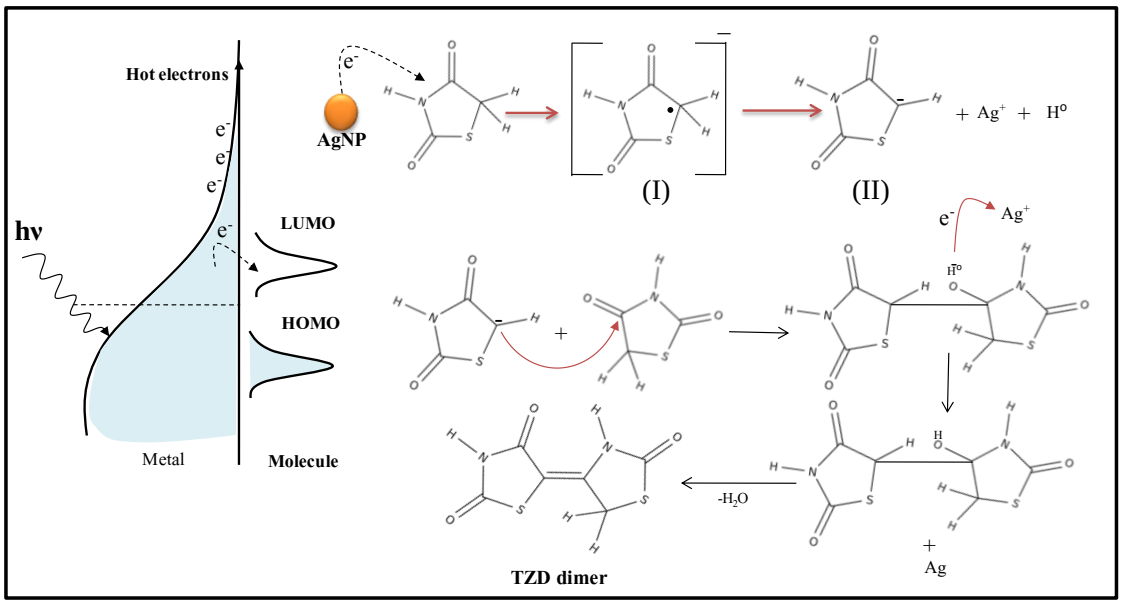

Scheme 4.3. Proposed reaction mechanism of dimerization of TZD induced by hot-electron transfer.

To further confirm and support our findings that the strong band at 1566 cm^{-1} is due to TZD dimer formed on the Ag NP surface, the vibrational frequencies of TZD dimer, and its complex with Ag are calculated. Two possible structures (E and Z) of TZD dimer were considered whose optimized geometries are shown in Figure 4.9. From the geometry optimization, it was found that the structure E (Figure 4.9 (a)) is more stable than Z (Figure 4.9 (b)) by 2.77 kJ/mol. The experimental SERS spectral bands are assigned based on the computed frequencies of the optimized structure of Ag complex of TZD dimer (E) and tabulated in Table 4.4. The observed strong band at 1566 cm^{-1} is assigned to the stretching vibration of C=C (ν C=C) and the medium intensity peak appearing at 450 cm^{-1} is attributed to the out-of-plane bending of C=C (γ C=C). Several weak Raman modes are observed which are also assigned and tabulated in Table 4.4. No low frequency band corresponding to metal adsorbate is seen, which suggests that the TZD dimer formed interacts with the silver surface via π electrons of the ethylenic bond (C=C). Similar type of interaction of π electrons with Ag and the absence of low frequency mode in SERS spectra are reported [177, 230]. The calculated Raman spectra of dimer (E), dimer (E)-Ag and the SERS spectrum (0.1M) are also shown in Figure 4.10 (c), (b) and (a) respectively and it can be seen that the computed spectra also have the strong peak at 1566 cm^{-1} corresponding to ν C=C and compare well with the SERS spectrum.

The nature of surface species present at higher and lower concentrations of TZD on Ag NP based on experimental evidence and DFT calculations has been discussed. The proximity of TZD molecules on the surface of Ag NP seems to be a necessary factor for the dimerization to occur. Recently, two different types of plasmon-induced reaction of *p* NTP molecules adsorbed on gold NP have been realized using SERS [218].

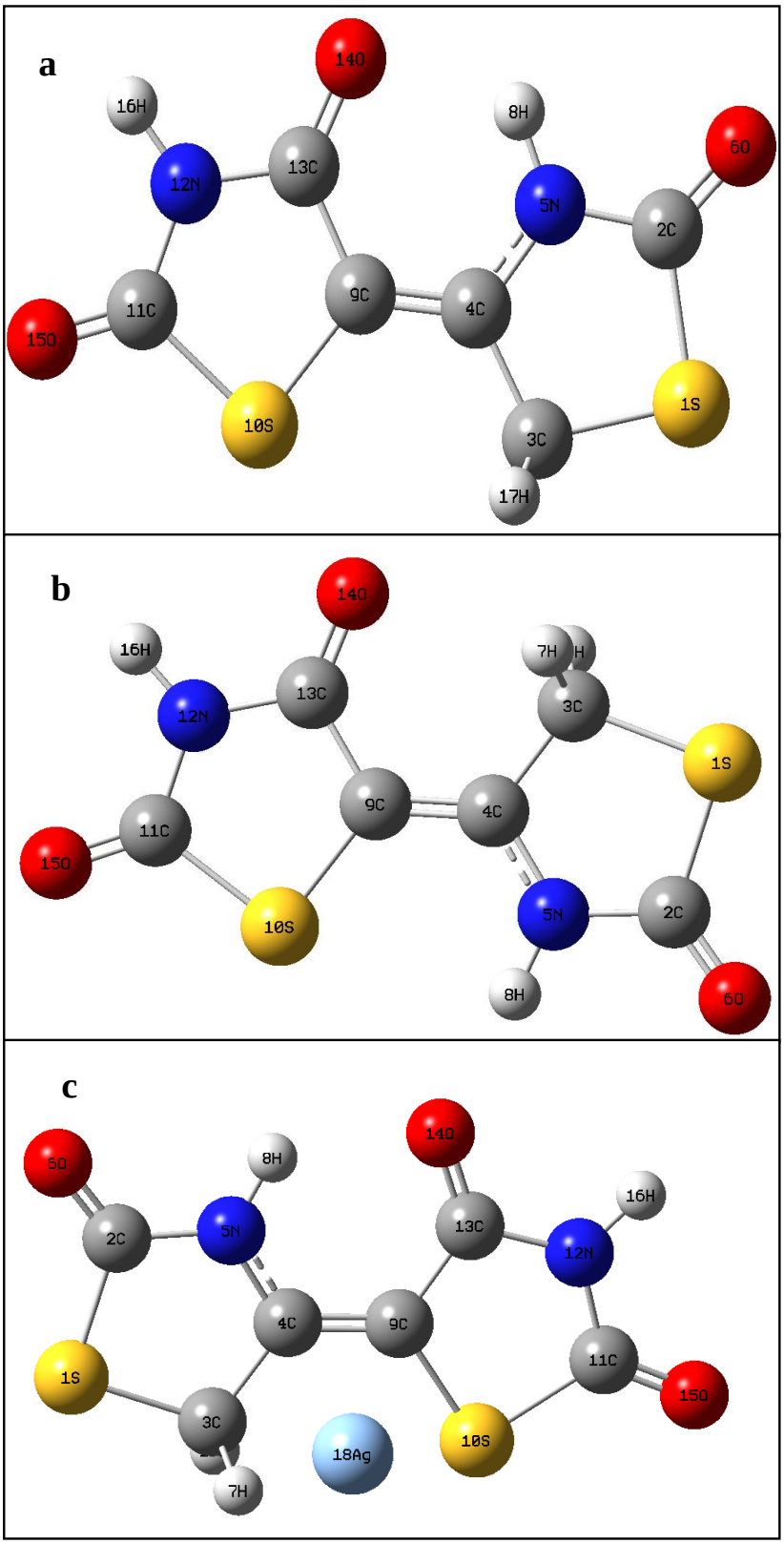

Figure 4.9. Optimized structures of (a) TZD dimer (E) (b) TZD dimer (Z) and (c) Ag-TZD.

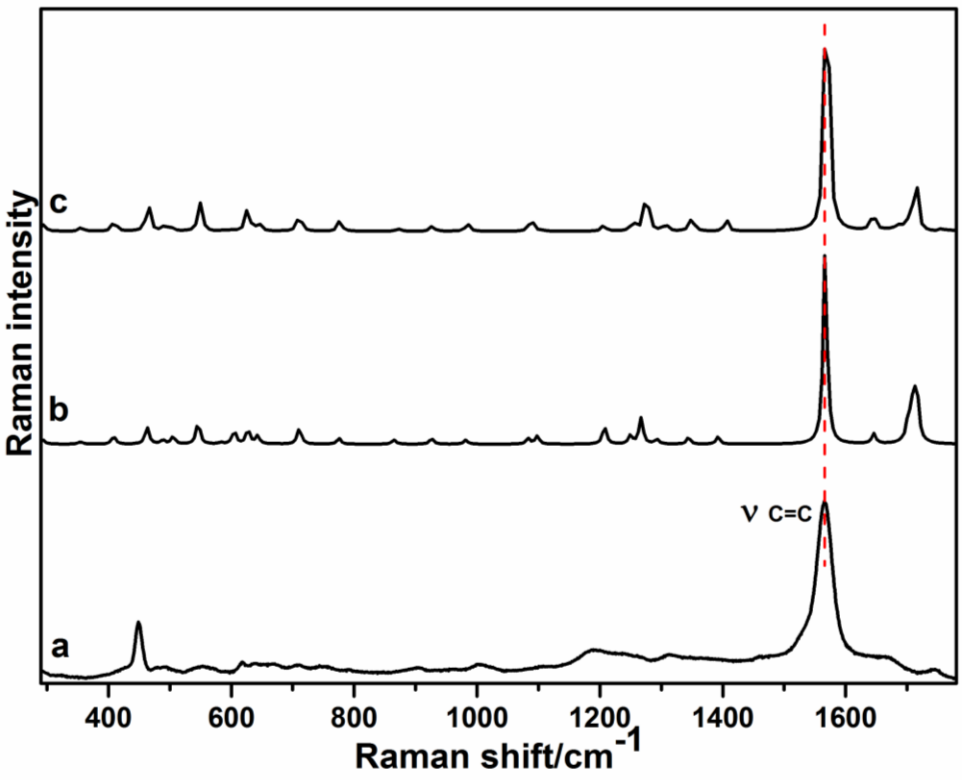

Figure 4.10. (a) SERS spectrum of TZD (10^{-1} M), calculated Raman spectra of (b) Ag−dimer E and (c) TZD dimer E.

The study indicated that *p* NTP at lower concentrations undergoes plasmon-induced intramolecular reaction, whereas at higher concentrations, it undergoes plasmon-induced dimerization to form DMAB molecule. The study reported that the distance between molecules is decisive for any dimerization to occur. If the distance between the adjacent molecules adsorbed on the metal NP surface is large, dimerization reaction will not be favoured and the SERS signal arising at lower concentrations can be related to the signal due to isolated molecules. Similarly, in our present study, TZD molecules at lower concentrations have not undergone dimerization reaction; instead, they get adsorbed on the Ag NP surface through a stable enolate anion.

In order to get the threshold values of TZD surface coverage and distance between TZD molecules on Ag NP for the dimerization reaction to occur on Ag NP surface, the surface coverage of the molecules on Ag NP and the distance between the adjacent molecules

were calculated. The total surface area of Ag NP in 1 mL of Ag NP sol (10^{-3}M) and the surface coverage of TZD was calculated using mass density relation. The diameter of Ag NP is 10 nm obtained from the TEM image (Figure 4.2B). The calculated total number of NP in 1 mL Ag NP solution is ~ 1.94×10^{15} and the total available surface area of Ag NP in 1 mL is ~ 6.09×10^{-1} m^2. The estimated surface coverage of TZD on Ag NP is about 0.137, 0.0137 and 0.00137 Å for concentrations of 10^{-4}, 10^{-5} and 10^{-6} M respectively assuming that all the molecules are adsorbed on the Ag NP surface. The estimated surface coverage obtained at concentration ≤ 10^{-4}M is in submonolayer range, which indicates that the adsorbed molecules are not closely packed on the Ag NP surface. Hence, the submonolayer thickness at lower concentrations of TZD does not favour or allow the dimerization to occur. Additionally, the average distance d between adjacent molecules was also calculated using the equation $d=R\sqrt{(8\pi/n)}$ [218], where n (molecular coverage) = n_M/n_{AgNP} and R is the radius of Ag NP ; n_M , n_{AgNP} are the number densities of TZD molecules and Ag NP in 1 mL solution respectively. The average distance d obtained between adjacent molecules for concentrations, 10^{-4}, 10^{-5} and 10^{-6} M are ~ 4.5, 45, 450 nm respectively. The calculated average distance d (4.5 nm) for 10^{-4}M concentration is 10 times larger than the size of a TZD molecule (~0.45 nm) which indicates that the intermolecular distance between two adjacent molecules are not close enough for dimerization. The calculated average distances between two closest molecules at concentrations 10^{-5} and 10^{-6} M are 45 and 450 nm, respectively, which makes the dimerization reaction impossible. However, at higher concentrations (≥ 10^{-3}), when the distance between adjacent molecules approaches the molecular size of TZD , 0.45 nm or less, the dimerization reaction proceeds at ease leading to the formation of TZD dimer.

4.5. CONCLUSION

In this chapter, we describe the first SERS study of TZD at different concentrations using Ag NP. The results indicate that TZD at higher concentrations ($\geq 10^{-3}$M) undergoes plasmon-induced dimerization reaction producing TZD dimer on the Ag NP surface evidenced by the presence of a prominent SERS peak at 1566 cm^{-1} attributed to the ν C=C band of the dimer. The calculated vibrational spectrum of TZD dimer and TZD dimer-Ag complex using DFT calculation has supported the experimental results. The formation of TZD dimer is due to the self condensation reaction (similar to the Knoevenagel condensation) plausible induced by the hot-electron-transfer mechanism. However, the SERS study at lower concentrations ($\leq 10^{-4}$M) suggests that TZD molecules undergo deprotonation and get adsorbed on the surface of Ag NP as enolate species. The SERS bands were assigned with the help of calculated Raman spectrum of Ag-TZD complex. The proximity of TZD molecules on the surface of Ag NP seems to be a crucial factor for the dimerization reaction to occur. At lower concentrations, most of the molecules lie apart and dimerization is less feasible and the adsorbed molecules remain as monomers, while at higher concentrations the molecules are close enough to each other on Ag NP surface for the dimerization reaction to take place, enabling the formation of TZD dimer.

CHAPTER 5.

SEIRA STUDIES OF SOME IMPORTANT BIOMOLECULES

5.1. INTRODUCTION

The strong near field enhancement created by resonant excitation of LSPR gives rise to the highly sensitive SERS spectroscopy. It is also observed that the strong enhanced local field and generated hot carriers by LSPR can trigger chemical reactions in molecular adsorbates on metal surface; resulting in the formation of new molecule [70-78, 231]. Hence, in such cases, the spectrum generated by SERS will not be from original molecule, but from the transformed molecule. However, in SEIRA spectroscopy, where infrared radiation is used instead of visible laser, the chances of chemical reactions of molecules on the metal NP are negligible, and the spectrum will be from the original molecule. Therefore, SEIRA spectroscopy, an extremely sensitive and molecular specific technique, can also serve as alternative and complementary technique to SERS for studying the various molecular systems. Apart from its sensitivity, it is also capable to provide the information about the interaction in molecule-metal interface. The interaction between biomolecules and noble metal surfaces has recently given rise to a large number of investigations due to challenging technological applications in the field of biomaterials, biosensors and bio-catalysis [17, 60, 232]. The understanding of the interactions of biomolecules with noble metal surfaces is important for the development of functional materials or devices that interface to living systems [233, 234].

As discussed in the section 1.1.2, mostly physically evaporated plasmonic metal island films on dielectric substrates were used for SEIRA spectroscopy [16, 105, 108, 114, 115], but recently wet-chemically prepared Au NP films on dielectric substrate (Si) are also being used as SEIRA active substrates [116, 117]. The main advantage of the wet-chemical preparation of SEIRA substrate is that it does not require costly instruments such as physical evaporator or sputtering unit. Normally, in wet-chemical preparation of SEIRA substrates, the metal NP are anchored on non-conducting dielectric substrate via an intermediate layer of

molecule deposited on dielectric substrate. The intermediate layer of the molecules provides the required electrostatic attraction for the metal NP to get immobilized on the dielectric substrate. Organosilane molecules, in particular aminopropyltriethoxysilane (APTES), are often used as intermediate layer to obtain the Au NP film.

In this chapter, we present the ATR-SEIRA studies of few important biomolecules adsorbed on wet-chemically prepared Au NP film deposited on APTES functionalized (silanised) glass substrate. ATR-SEIRA studies are generally carried out using a thin metal film directly coated on the ATR crystal and the samples are deposited over the metal film [16, 105-107]. However, metal coating on ATR crystal contaminates and sometimes damages the crystal. The present ATR-SEIRA technique, wherein glass substrate coated with Au NP is used as SEIRA substrate, provides an attractive and alternative method of employing non-coated ATR crystal which avoids the damages and contaminations of the ATR crystal.

This chapter is divided into two sections. The first section 5.2 deals with the IR absorption characteristics of taurine and sodium benzoate molecules adsorbed on Au NP film investigated by ATR-FTIR technique and second section 5.3 demonstrate the morphological impact of Au NP film on SEIRA signal of uracil, a RNA nucleobase.

5.2. SEIRA STUDY OF SODIUM BENZOATE AND TAURINE

5.2.1. INTRODUCTION

Sodium benzoate (C_6H_5COONa), a food preservative, is widely used in various products of food and pharmaceutical industry because of its antimicrobial and flavour characteristics. Usage and dosage of food preservative are concern due to their influence in human body [235-237] and their content in food should be controlled accurately. Vibrational spectroscopic

studies of sodium benzoate including infrared absorption, Raman and SERS are reported [238-240].

Taurine ($NH_3^+CH_2CH_2SO_3^-$), a sulphur containing amino acid is found in most mammalian tissues [241, 242]. It is involved in numerous diverse biological and physiological functions and also has antioxidant effects [242, 243]. Its deficiency is associated with various disorders like anxiety, epilepsy, hyperactivity and depression [244]. Apart from the reports on biological studies of taurine, the vibrational spectroscopic analysis using Raman and IR and studies about its interaction with metal ions are reported [245-247]. The biological significance and inclusion of two acidic groups (SO_3^- and NH_3^+ groups) make taurine an interesting compound for the SEIRS studies.

In this work, we demonstrate the first ATR-SEIRA studies of sodium benzoate and taurine using Au NP films on APTES treated glass as SEIRA active substrate. The aim of this work is as follows: (i) to check the applicability of the wet chemically prepared SEIRA active substrates by studying the effect of Au NP on the IR signal of sodium benzoate and taurine molecules (ii) to understand the interfacial interaction of sodium benzoate and taurine with Au NP surface and (iii) determine the possible sites of interaction of the molecules with Au NP.

5.2.2. EXPERIMENTS

5.2.2.1. FABRICATION OF AUNP FILMS ON GLASS SUBSTRATE

For ATR–SEIRA experiments, Au NP films were prepared by wet chemical deposition of Au NP on silanised glass surface [248]. Freshly prepared piranha cleaned glass slides (10×100 mm) were silanised by immersing them in a 10% solution of APTES dissolved in ethanol for 4 h. The silanisation reaction involves the hydroxylation of glass substrate followed by

hydrolysis of the APTES ethoxy group. Slides were removed and cleaned ultrasonically in ethanol for several times to remove unbound APTES molecules. The slides were kept in oven at 120°C for 1 hr to enhance the covalent bonding of APTES with glass substrate. The silanised glass slides were dipped in freshly prepared Au colloid prepared by citrate reduction method for 4 h (described in section 2.3.4) followed by rinsing with deionized water and left to dry in oven at 120 °C for 15 min. The Au NP films thus prepared were immersed in aqueous solutions of sodium benzoate and taurine (10^{-2}M), removed and dried in air. Sodium benzoate and taurine was obtained from sigma and used without further purification and all the chemicals used are of AR grade. Deionized water was used for all preparations. The schematic representation of preparation method is shown in Scheme 5.1.

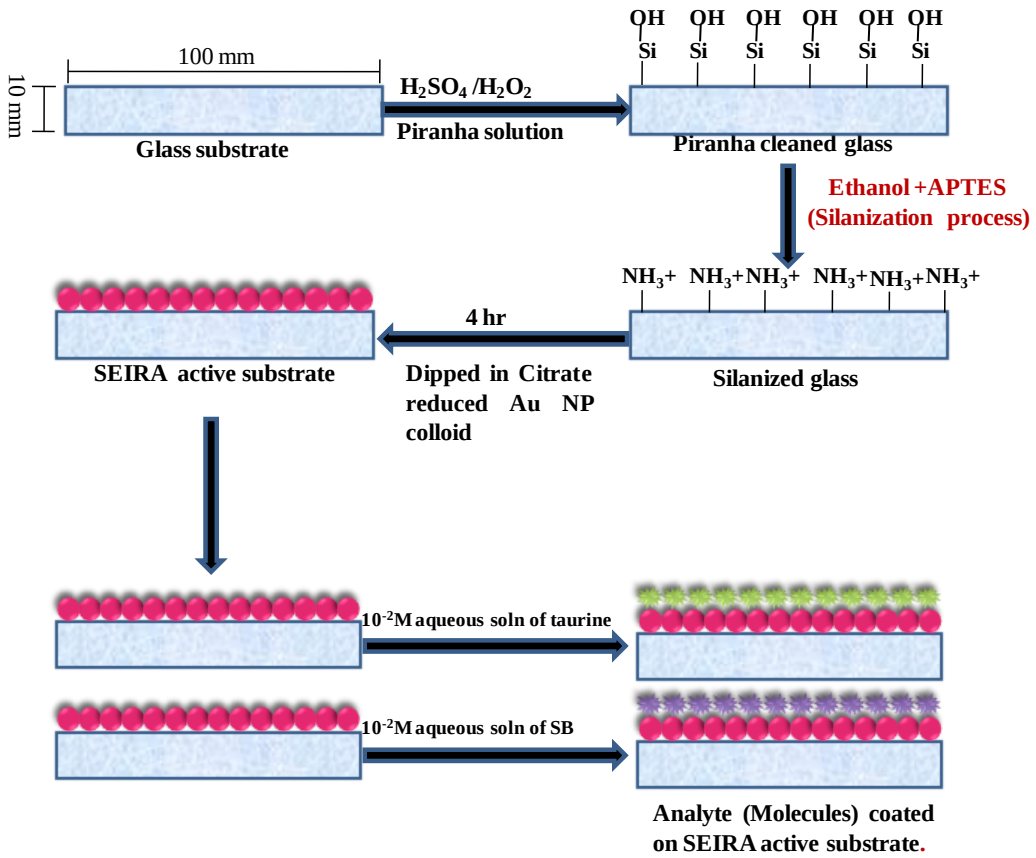

Scheme 5.1. Schematic of preparation of Au NP film on glass substrate.

5.2.2.2. CHARACTERIZATION OF Au NP FILMS

The fabricated Au NP films were characterized by taking AFM images. AFM images were obtained by NT-MDT Solver P-47H multimode ambient based scanning probe microscope system as described in section 2.3.5.2. The cantilever used was a Si with typical spring constant of 6 N/m and resonant frequency of 135 kHz.

5.2.2.3. ATR AND ATR–SEIRA SPECTRAL MEASUREMENTS USING FTIR

The ATR-SEIRA spectra of sodium benzoate and taurine adsorbed on Au NP films on glass substrate were obtained in the 650-1800 cm^{-1} region at spectral resolution of 4 cm^{-1} with Bruker 80V FTIR, using multiple reflection horizontal ATR (Pike technologies) unit of ZnSe crystal (100×10 mm^2) as an internal reflection element with internal incidence angle of 45º, KBr beamsplitter, DTGS detector, and globar source. The glass substrate (size: ~ 100 x 10 mm^2) were placed over the ATR crystal and maximum pressure was applied using slip-clutch mechanism which ensures good sample contact as shown in Scheme 5.2. A beam of infrared light is passed through the ZnSe crystal in such a way that it undergoes total internal reflection at the surface in contact with the glass slide. This internal reflectance creates an evanescent wave that goes beyond the surface of the crystal and penetrates into the sample (which is held in contact with the crystal). The IR beam undergoes several reflections before exiting the crystal. To ensure good optical contact, the glass slides were placed over the ATR crystal and maximum pressure was applied using the pressure clamp provided with the instrument. The spectrum of a silanised glass substrate was used as reference in all the measurements. ATR spectra of powdered sodium benzoate and taurine were also recorded in the 650-1800 cm^{-1} region at the spectral resolution of 4 cm^{-1}.

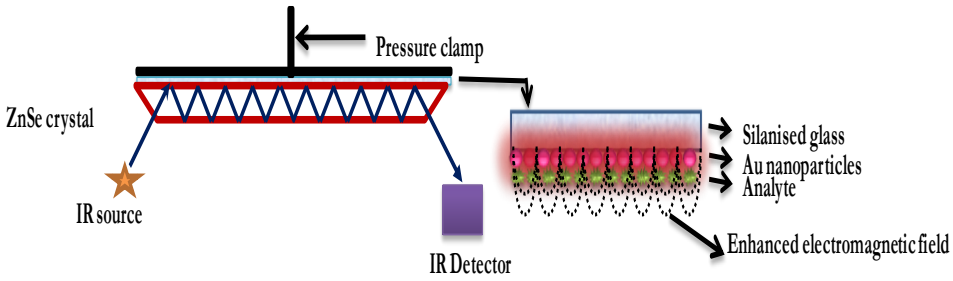

Scheme 5.2. Schematic representation of ATR set up.

5.2.3. RESULTS

5.2.3.1. AFM IMAGE OF THE Au NP FILM

The morphology of Au NP film on glass substrate is shown in Figure 5.1. The RMS surface roughness measured from the AFM image of the Au NP film is ~ 9 nm and the average size of the particles is ~76 nm.

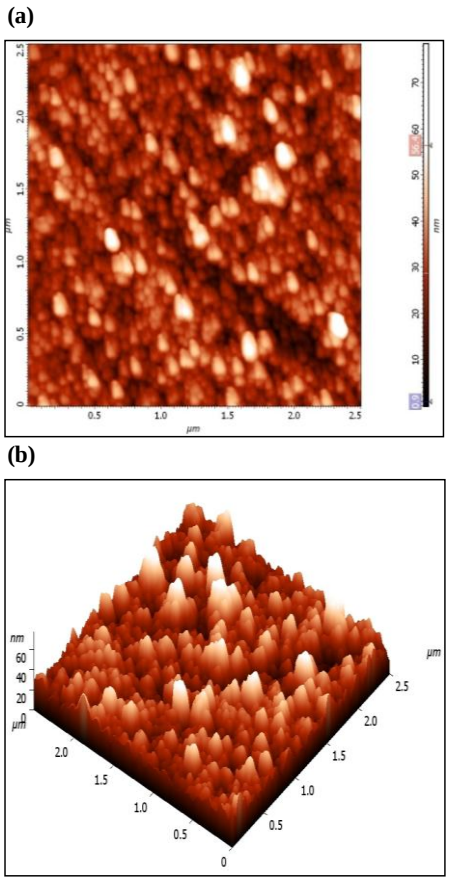

Figure 5.1. AFM image of Au NP film on glass substrate (a) 2D, (b) 3D.

5.2.3.2. ATR / ATR-SEIRA SPECTRA OF SODIUM BENZOATE

The ATR bands of sodium benzoate powder are assigned based on the literature [238-240] and are shown in Figure 5.2a. The assignments are presented in Table 5.1. Bands present in the spectra originate from both carboxylate vibrations and ring vibrations. Bands originating from carboxylate anion vibrations are: (1) asymmetric stretch $\nu_{asym}(COO^-)$ located at 1552 cm^{-1} (2) symmetric stretch $\nu_{sym}(COO^-)$ at 1419 cm^{-1} (3) in plane symmetric deformation $\delta(COO^-)$ at 844 cm^{-1} (4) out of plane symmetric deformation $\gamma_{sym}(COO^-)$ at 710 cm^{-1}. The remaining bands present in the spectra originate from aromatic ring vibrations. The peaks at 1395, 1597 and 1622 cm^{-1} originate from ν (CC) stretch of the benzene ring.

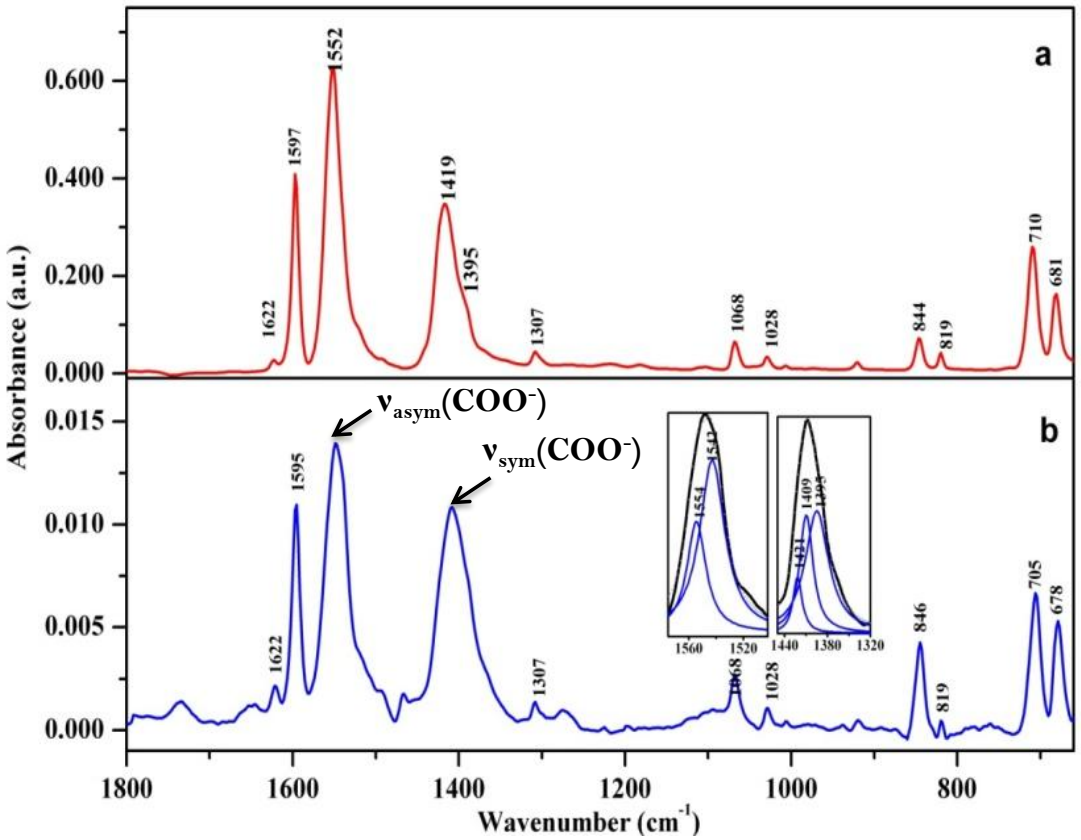

Figure 5.2. (a) ATR-FTIR spectrum of sodium benzoate and (b) ATR-SEIRA spectrum of sodium benzoate.

The ATR-SEIRA spectrum of benzoate deposited from the aqueous solution on Au NP film is shown in Figure 5.2b and their assignments are given in Table 5.1. The spectrum is similar

to the ATR spectrum of sodium benzoate powder except that the modes associated to the carboxylate stretches (symmetric and asymmetric). These modes are broadened in SEIRA spectrum. A new red-shifted asymmetric stretch band ($\nu_{asym}(COO^-)$) appears at 1542 cm^{-1} along with the 1554 cm^{-1} band, as shown in the inset of Figure 5.2b. Similarly, in the symmetric stretch ($\nu_{sym}(COO^-)$, a red shifted band also appears at 1409 cm^{-1} along with the original stretch at 1421 cm^{-1}. The deformation band of carboxylate at 846 cm^{-1} show increase in the band width and in the relative intensities with the adjacent peak of γ CH (819 cm^{-1}). The ring vibrations do not show any significant change.

Table 5.1. Assignments of ATR & ATR-SEIRA bands of sodium benzoate.

ATR of powder sodium benzoate (cm^{-1})	**ATR-SEIRA of sodium benzoate (cm^{-1})**	**Assignments**
1622 w	1622 w	ν (CC)
1597 s	1595 s	ν (CC)
1552 s	1554 m	$\nu_{asym}(COO)^-$
	1542 s	
1419 s	1421 m	$\nu_{sym}(COO)^-$
	1409 s	
1395 m	1395 m	ν (CC) + δ CH
1307 w	1307 w	δ (CH)
1068 w	1068 w	δ (CH)
1028 w	1028 w	δ (CH)
844 w	846 m	δ (COO^-)
819 w	819 w	γ (CH)
710 m	705 m	$\gamma_{sym}(COO^-)$
681 m	679 m	τ_{ring}, γ (CH)
w: weak, m: medium, vw : very weak, s: strong, br: broad, sh: shoulder, υ: stretch, sym: symmetric, asym.: asymmetric, δ: in plane bend, w: wag, r: rock, t: twist.		

5.2.3.3. ATR / ATR-SEIRA SPECTRA OF TAURINE

ATR spectrum of solid taurine is shown in Figure 5.3a and the bands are assigned based on the literature [245-247] given in Table 5.2. Taurine ($NH_3^+C_\alpha H_2C_\beta H_2SO_3^-$) exists in the form of zwitter ions in the solid state. The characteristic bands of NH_3^+ deformation vibrations (symmetric and asymmetric vibrations) are observed in the 1500-1650 cm^{-1} region. They are seen as medium intense bands at 1512, 1585 and 1616 cm^{-1} respectively. The prominent bands seen in the spectrum are due to asymmetric (1216 cm^{-1}); symmetric stretches (1034 cm^{-1}) of SO_3, C_β-S stretch (738 cm^{-1}) and NH_3 rock (1182 cm^{-1}). The deformation modes of CH_2 like scissoring (1457, 1427 cm^{-1}), twisting (1303, 1250 cm^{-1}), wagging (1388, 1344 cm^{-1}) and rocking (960, 893, 846 cm^{-1}) modes are observed and are listed in the Table 5.2.

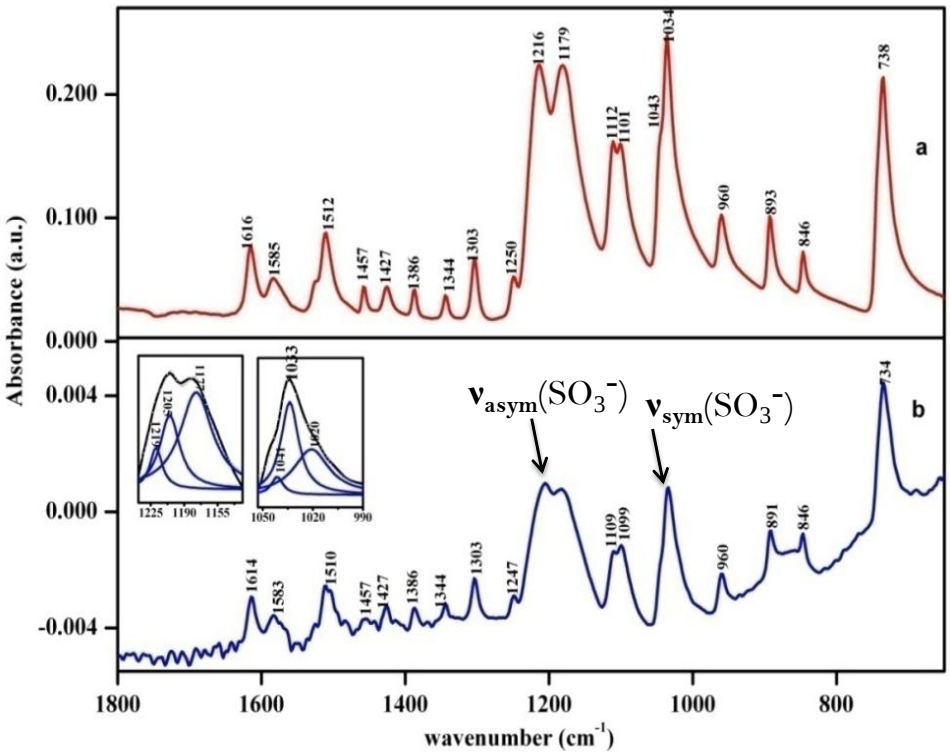

Figure 5.3. (a) ATR-FTIR spectrum of taurine and (b) ATR-SEIRA spectrum of taurine.

Figure 5.3b depicts the ATR-SEIRA spectrum of taurine and the peak assignments are listed in Table 5.2. The spectrum show changes when compared to Figure 5.3a. Similar to the

observation with sodium benzoate, changes are seen in the asymmetric and symmetric stretches of SO_3 group of taurine. Broadening of both the peaks with appearance of additional red shifted bands (1205 cm^{-1} and 1020 cm^{-1}) is observed and is shown in the inset of Figure 5.3b. The C_β-S stretch shows red shift from 738 to 734 cm^{-1}. The remaining bands do not show any significant change. The silanised glass substrate without the Au NP film was dipped in 10^{-2} M solution of taurine and the ATR spectrum was recorded which gave no signal of taurine.

Table 5.2. Assignments of ATR & ATR-SEIRA bands of taurine.

ATR of powder taurine (cm^{-1})	**ATR-SEIRA of taurine(cm^{-1})**	**Assignments**
1616 w	1614 w	δ_{asym} (NH_3)
1585 w	1583 w	δ_{asym} (NH_3)
1512 w	1510 w	δ_{sym} (NH_3)
1457 w	1457 w	δ ($C_\beta H_2$)
1427 w	1427 w	δ ($C_\alpha H_2$)
1388 w	1386 w	*w*($C_\alpha H_2$)
1344 w	1344 w	*w* ($C_\beta H_2$)
1303 w	1303 w	t($C_\beta H_2$)
1250 w	1247 w	t ($C_\alpha H_2$)
1216 s	1219w	υ_{asym}(SO_3)
	1205 m	
1182 s	1179 s	r(NH_3)
1112 m	1109 m	γ ($C_\alpha C_\beta N$)
1101 m	1099 m	
1043m	1041m	υ ($C_\alpha N$)
1034 s	1033 s	υ_{sym} (SO_3)
	1020 m	
960 w	960 w	r ($C_\beta H_2$),υ ($C_\alpha C_\beta$)
893 m	891 w	r ($C_\alpha H_2$)
846 w	846 w	r ($C_\beta H_2$), υ ($C_\alpha N$)
738 s	734 s	υ ($C_\beta S$)
w: weak, m: medium, vw : very weak, s: strong, br: broad,sh: shoulder, υ: stretch, sym: symmetric, asym.: asymmetric,δ : in plane bend,*w*: wag, r: rock, t: twist.		

5.2.4. DISCUSSION

ATR spectrum of sodium benzoate and taurine deposited on Au NP films show distinct changes when compared to their powder samples. All the changes are associated with the carboxylate and sulphonate groups of sodium benzoate and taurine respectively. From the SEIRA spectra, the symmetric and asymmetric stretches of both the carboxylate and sulphonate groups appears to be broadened when compared with normal IR spectra and the peak fitting of these bands revealed the appearance of new redshifted bands. The broadening of the above mentioned vibrational bands is an evidence of multi-layer formation of molecules wherein the layer closest to the Au NP film is chemically bound to the film. The stretching frequencies of carboxylate and sulphonate groups involved in the chemical binding are softened and given rise to red shifted bands and the observed redshift in the bands is thus a direct consequence of chemical interaction of molecules with the Au NP film. The unshifted bands (symmetric and asymmetric) of both sodium benzoate and taurine are due to the top layers which are not involved in chemical interaction with metal. The signatures of both chemisorbed and physisorbed layers on Au NP are clearly observed. Hence, with help of SEIRA method, the formation of monolayer and multilayer can also monitored. SERS studies of sodium benzoate on silver colloid showed a red-shift of 32 cm^{-1}in the symmetric stretch of the carboxylate group [249], while the redshift observed in the present study is10 cm^{-1}. The above observation seems to suggest that the interaction of sodium benzoate with Au NP is weaker than the interaction with the Ag NP. In the case of taurine, a red shift of 14 cm^{-1} is observed in the sulphonate group when compared to the ATR spectrum of its powder and no surface enhanced vibrational studies of taurine are reported so far.

In order to estimate the enhancement in IR signal, the ATR spectrum of the silanised glass slides (without Au NP film) soaked in taurine and sodium benzoate were measured and

we could not get the IR absorption signal and hence the enhancement arising out of the SEIRA effect was difficult to evaluate quantitatively.

Sensitivity limitations and the strong liquid water absorption bands limit the infrared spectroscopy in getting the vibrational spectrum of biomolecules present in aqueous environment. Here, the present ATR-SEIRA method can be used as powerful tool to obtain the vibrational information of biomolecules present in aqueous media. The biological molecules present in aqueous solutions can thus be brought to the adsorbed state on SEIRA substrate and easily detected. Thus it is a useful technique to obtain vibrations of biological molecules present in the aqueous solution which otherwise would be difficult due to the interference of water bands.

5.2.5. CONCLUSION

ATR-SEIRA spectra of sodium benzoate and taurine deposited from aqueous solutions on Au NP film were recorded and compared with the ATR spectra of sodium benzoate and taurine powders. The SEIRA spectra of both sodium benzoate and taurine show distinct changes in the vibrational modes of carboxylate and sulphonate groups respectively. The bands of the asymmetric and symmetric stretches of both the groups appear broadened due to the presence of red-shifted bands along with the original stretching vibrations. Although the enhancement could not be estimated, the studies indicate multilayer formation of both sodium benzoate and taurine on the Au NP film with bottom layer chemically bound to Au NP through carboxylate and sulphonate groups respectively.

5.3. SEIRA STUDIES OF URACIL, A RNA NUCLEOBASE: EFFECT OF MORPHOLOGY OF Au NP FILM

5.3.1. INTRODUCTION

The study described in above section 5.2 clearly shows that wet-chemically prepared Au NP film on glass substrate has the potential to enhance the IR absorption signal and more importantly, the simple method used in the fabrication of Au NP film on glass substrate and its coupling with ATR crystal is very effective to carry out the SEIRA measurements. As discussed in section 1.1.2, the strength of SEIRA signal depends on the metal types and also on the metal film morphology [101-104]. In wet-chemical method, the morphology of Au NP films can be easily varied by changing the immersion duration of silanised glass substrates in Au NP sol. This section will elaborate the impact of morphology of wet-chemically prepared Au NP films on SEIRA signal.

Uracil, a RNA nucleobase, has been selected for the study due to its significance in bio-spectroscopy and bio-sensing. It is an essential component of genetic material and has significant role in biological science such as replication, transmission of genetic information and molecular recognition [250]. Thin films of uracil and other nucleic acid bases are also being used for field effect transistor, molecular electronics and bio-sensors [251, 252]. Here, SEIRA studies of uracil and impact of Au NP film morphology on SEIRA signal is presented and discussed. Under the identical conditions, IR absorptions of uracil adsorbed on silanised glass substrate without Au NP film were also measured for comparison with the SEIRA spectra.

5.3.2. EXPERIMENTS

5.3.2.1. SAMPLE PREPARATION

Au NP films were prepared by wet-chemical deposition of Au NP on silanised glass slides as discussed in section 5.1.2. Piranha cleaned fresh glass slides (100 × 10 mm^2) were silanised by immersing them in a 1% ethanolic solution of APTES. The silanised glass slides were ultrasonically cleaned in ethanol several times to remove unbound APTES molecules. The slides were kept in oven at 120 °C for 1 h to enhance the covalent bonding. Subsequently, these slides were dipped in fresh gold colloid, prepared by citrate reduction method, for ½ an hour, 2 and 4 h as shown in Scheme 5.3. They were removed, rinsed with deionized water and left to dry in oven at 120 °C for 15 min. The Au NP films deposited on the silanised glass slides after ½ an hour, 2 and 4 h of deposition times are referred as G1, G2 and G3 respectively in the following text. G1, G2, G3 and a silanised glass slide without Au NP film were immersed separately in 10^{-6} M aqueous solution of uracil for 24 h, removed and dried in air by keeping the glass slides vertical. 9 μg of uracil powder was dissolved in 80 ml of deionised water to get 10^{-6} M uracil solution. Similarly, fresh set of above glass slides were immersed in 10^{-4} and 10^{-2} M solution of uracil for 24 h, removed and dried in air. Uracil gets deposited on both the surfaces of the glass slide but ATR-FTIR measurements were carried out for only one surface. Uracil was obtained from Sigma and used without further purification. All the chemicals used in study are of AR grade.

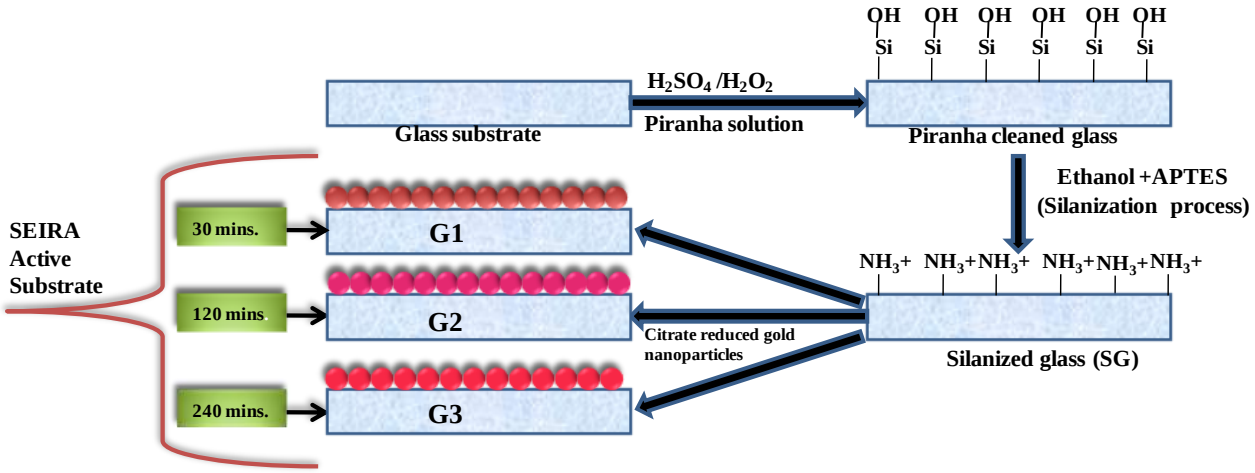

Scheme 5.3. Schematic of preparation of Au NP film with different morphology on glass substrate.

5.3.2.2. CHARACTERIZATION OF Au NP FILMS

In order to correlate surface morphology with the SEIRA spectra, AFM images of the Au NP films deposited on the silanised glass slides (G1, G2 and G3) were obtained using NT-MDT Solver P-47H multimode ambient based scanning probe microscope system. The cantilever used was Si with typical spring constant of 6 N/m and resonant frequency of 135 kHz.

5.3.2.3. IR SPECTRAL MEASUREMENTS

The IR absorption spectra of uracil adsorbed on G1, G2, G3 films and on silanised glass slides without Au NP film were measured at spectral resolution of 4 cm^{-1} with Bruker 80 V FTIR spectrometer using multiple reflection horizontal ATR unit of ZnSe crystal (100 × 10 mm^2) as IRE with internal incidence angle of 45°, KBr beamsplitter, DTGS detector, and globar source. The schematic diagram of the experimental setup is shown in Scheme 5.2 (Section 5.2.2). To ensure good optical contact, the glass slides were placed over the ATR crystal and maximum pressure was applied using the pressure clamp provided with the instrument as shown in Scheme 5.2. The IR absorption spectrum of uracil powder was also

recorded at the spectral resolution of 4 cm^{-1} by ATR method. The powder was spread uniformly onto the ATR crystal and the spectrum was recorded.

5.3.3. RESULTS

5.3.3.1. AFM IMAGES

The morphology of Au NP films G1, G2 and G3 is shown in Figure 5.4 (a, b, c). Each of the Figure 5.4 (a), (b) and (c) has both 2D and 3D images adjacent to each other. The film parameters are given in Table 5.3.

Table 5.3. Film parameters of G1, G2 and G3 Au NP films obtained from AFM.

Film parameter	**G1**	**G2**	**G3**
Peak to peak height, S_y	5.52 nm	24.9 nm	25.58 nm
Ten point height	2.98 nm	12.40 nm	12.78 nm
Average roughness, S_a	0.311 nm	1.44 nm	0.989 nm
RMS surface roughness	0.45 nm	2.31 nm	1.91 nm

5.3.3.1. ATR-FTIR ABSORPTION SPECTRUM OF URACIL POWDER

The IR spectrum of uracil powder in the spectral region (1280–1800 cm^{-1}) is presented in Figure 5.5 and the observed frequencies with the vibrational mode assignments are tabulated in Table 5.4. The vibrational modes are assigned based on studies carried out by Susi and Ard

[253] and others [254, 255]. Uracil molecule has three double bonds (one C=C and two C=O bonds) numbered as C5=C6, C2=O7 and C4=O8 as shown in inset of Figure 5.5.

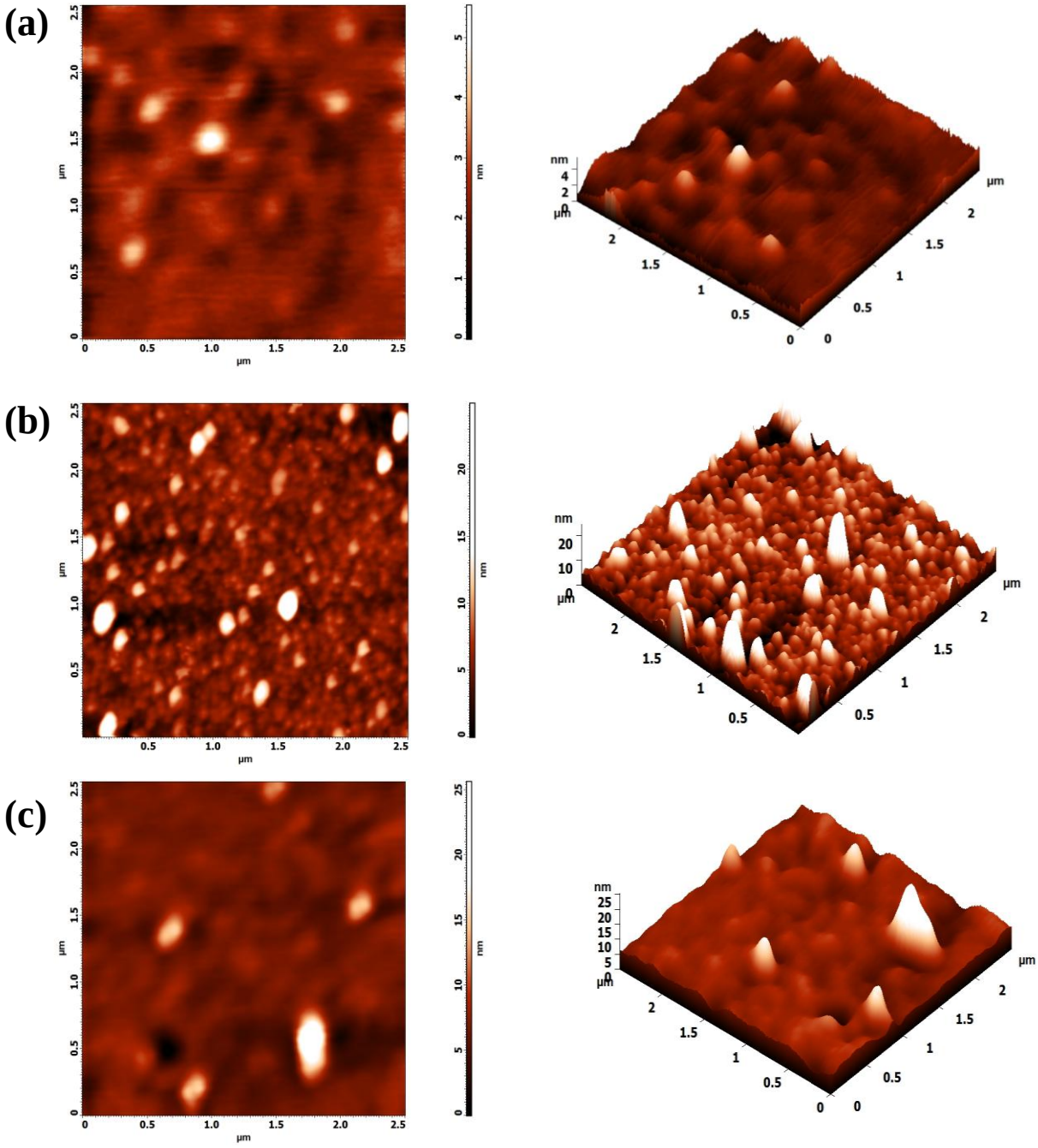

Figure 5.4. 2D and 3D AFM images of Au NP films (a) G1 (b) G2 (c) G3.

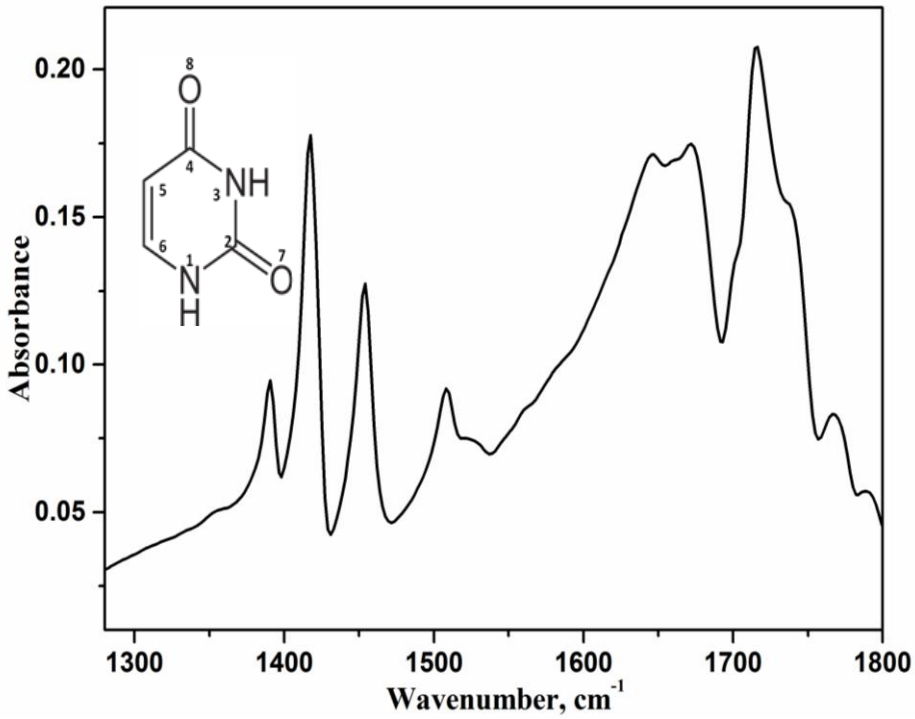

Figure 5.5. ATR-FTIR spectrum of uracil powder.

These double bonds are responsible for many fundamental vibrational bands and some of these vibrational bands appear in 1600-1800 cm^{-1} spectral regions which is also called as the double bond region. The molecule has six C=O vibration modes, out of these, the two stretching modes ν (C4=O8) and ν (C2=O7) are observed at 1672 cm^{-1} and 1716 cm^{-1} respectively as strong peaks. Apart from these two bands, there are few more bands at 1740, 1768 cm^{-1} which are due to the fermi resonance with combination bands reported by Florian and Hrouda [255]. The stretching vibration of C5=C6 is observed as a strong peak at 1645 cm^{-1}. The N1H, N3H, and C5H in-plane bending modes are observed at 1509, 1417 and 1390 cm^{-1} respectively. The stretching modes of pyrimidine ring, which is the part of uracil, are observed at 1454 and 1645 cm^{-1}.

Table 5.4. Assignments of ATR-FTIR spectral peaks (cm^{-1}) of uracil.

Uracil powder	Uracil on G1	Uracil on silanised glass without Au NP	Assignment
1390 w	1390 w	1390 w	δC_5H
1417 s	1417 s	1416 s	δN_3H
1454 s	1454 s	1452 w	νC_6N_1
1509 w	1508 w	1505 w	δN_1H
1645 s	1645 s	1646 s	$\nu C_5=C_6$
1672 s	1677 s	1671 s	$\nu C_4=O_8$
1716 s	1716 s	1711 s	$\nu C_2=O_7$
1740 s	1743 s	1740 w	Overtone+ fermi resonance
1768 w	1769 w	1764 w	combination band
w: weak, m: medium, vw : very weak, s: strong, br: broad, sh: shoulder, υ: stretch, sym: symmetric, asym.: asymmetric, δ: in plane bend, w: wag, r: rock, t: twist.			

5.3.3.2. ATR–FTIR ABSORPTION SPECTRA OF URACIL ON G1, G2 AND G3

Figure 5.6 (a, b, c) correspond to IR spectra (1280-1800 cm^{-1}) of uracil adsorbed from 10^{-6} M aqueous solution of uracil onto G1, G2 and G3 films respectively. Because of the strong absorption of glass, the spectral region below 1280 cm^{-1} is not shown here. Figure 5.7 (a, b, c) and Figure 5.8 (a, b, c) correspond to IR spectra of uracil adsorbed from 10^{-4} and 10^{-2} M aqueous solution onto Au NP films respectively. ‘a’, ‘b’ and ‘c’ in all the figures correspond to G1, G2 and G3 respectively. The assignments of the vibrational bands are tabulated in Table 5.4.

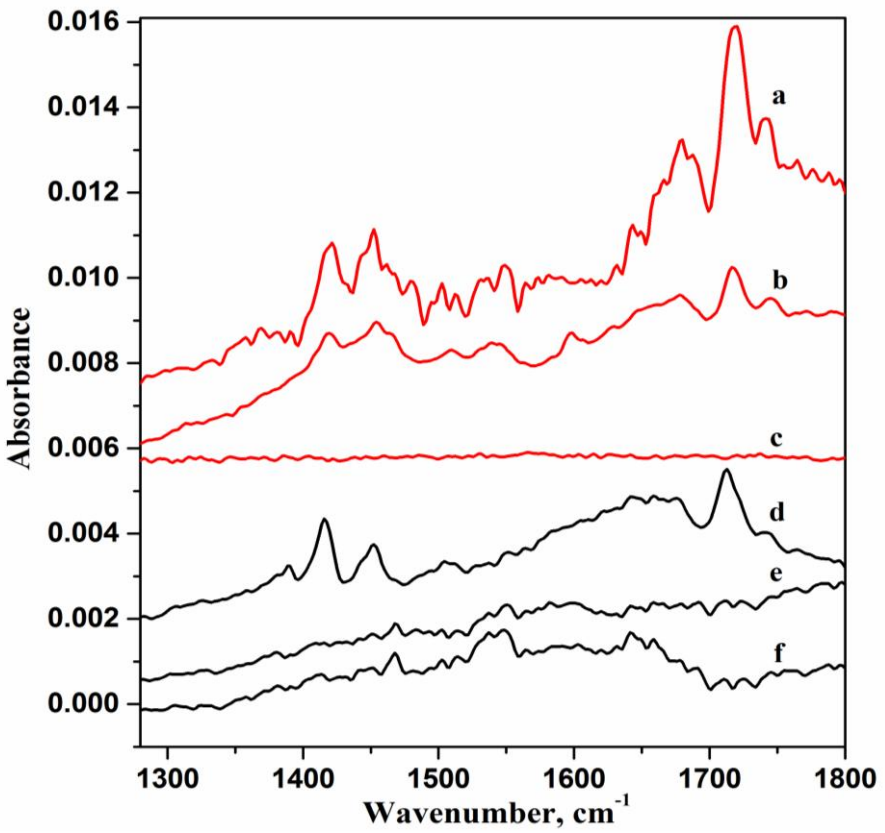

Figure 5.6. ATR- FTIR spectra (—) of uracil deposited on a) G1 b) G2 c) G3 from 10^{-6} M solution. ATR-FTIR spectra (—) of uracil deposited on silanised glass slide without Au NP film from d) 10^{-2} e) 10^{-4} and f) 10^{-6} M.

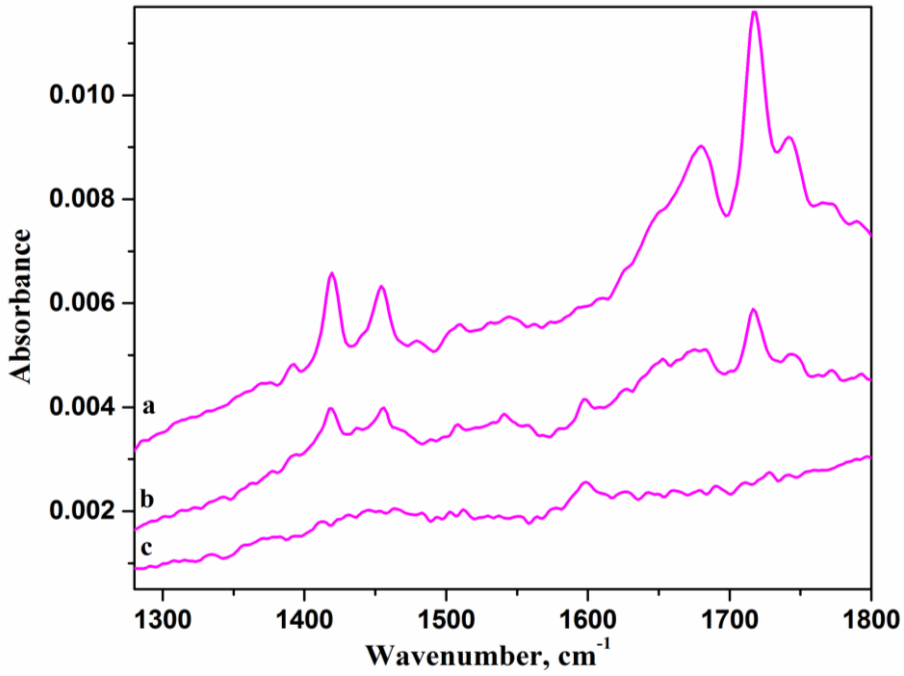

Figure 5.7. ATR-FTIR spectra of uracil deposited on a) G1 b) G2 c) G3 from 10^{-4} M solution.

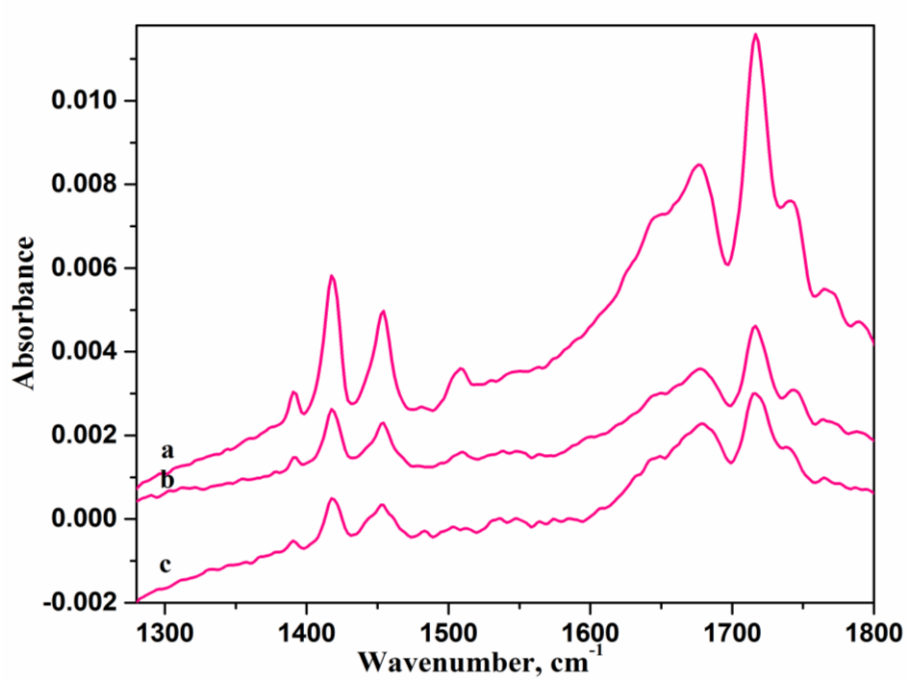

Figure 5.8. ATR-FTIR spectra of uracil deposited on a) G1 b) G2 c) G3 from 10^{-2} M solution.

5.3.3.3. ATR-FTIR ABSORPTION SPECTRA OF URACIL ADSORBED ON SILANISED GLASS SLIDE WITHOUT Au NP FILM:

The IR absorption spectra (1280-1800 cm^{-1}) of uracil adsorbed on silanised glass slide without Au NP film from 10^{-2},10^{-4} and10^{-6} M aqueous solutions are shown in Figure 5.6 (d, e, f) and the assignments are tabulated in Table 5.4.

5.3.4. DISCUSSION

5.3.4.1. COMPARISON OF IR ABSORPTION SPECTRA OF URACIL ADSORBED ON G1, G2 AND G3 FILMS

The intensities obtained for the IR spectra of uracil adsorbed from 10^{-6} M solution of uracil on G1, G2 and G3 are different as seen in Figure 5.6 (a, b, c). While G1 gave the highest intensity, G2 gave reasonably a good spectrum and no discernible spectrum was obtained

from G3 film. The above observation is characteristic feature of SEIRA because it is reported that enhancement chiefly depends on the morphology of the metal film [112, 256-259]. If SEIRA was not prevalent, then similar to G3 film, G1 and G2 films also wouldn't have given the IR bands of uracil. It seems that the morphology of the G3 film have not supported the field enhancement and hence could not give any spectrum. The above results imply that the spectra arising from G1 and G2 films is solely due to the SEIRA phenomenon, with the assumption that the same amount of uracil gets deposited on all the three films. Under the identical conditions, IR absorption spectrum measured for uracil adsorbed from 10^{-6} M solution on silanised glass slide without Au NP film did not give any signal as shown in Figure 5.6 (f) which further supports our arguments. The IR measurements of 10^{-4} and 10^{-2} M concentration of uracil adsorbed on silanised glass slides (without Au NP film) were also recorded, and the observed spectra are shown in Figure 5.6 (e) & (d) respectively. 10^{-2} M concentration of uracil was able give the IR absorption spectrum whose details are reported [260] , whereas no discernible features were seen for concentration $\leq 10^{-2}$ M. The observed IR absorption at higher concentration (10^{-2} M) is due to the formation of a thick film whose absorption spectrum can be measured in the ATR mode, while at lower concentrations (10^{-6} & 10^{-4} M) the thickness of the uracil films might not have reached the minimum threshold thickness.

In order to see the impact on IR absorption spectra due to the increase in the surface coverage of uracil molecules on G1, G2 and G3, the Au NP slides were exposed to higher concentrations solutions (10^{-4} & 10^{-2} M) and the spectra were recorded which are shown in Figure 5.7 and Figure 5.8 respectively. G1 film gave intense spectra for both the concentrations as shown in Figure 5.7 a and Figure 5.8 a, whereas G3 film gave spectrum only for 10^{-2} M solution (Figure 5.8 (c)). G2 film gave modest spectra for both the concentrations as shown in Figure 5.7 b and Figure 5.8 b. The intensity of C_2O_7 stretch (1716

cm^{-1}) of uracil obtained from G1, G2 and G3 films dipped in all the three concentrations of uracil was measured by creating the local base line using OPUS 6.5 package and is shown in Table 5.5. The intensity of the 1712 cm^{-1} peak attributed to C_2O_7 stretch observed for uracil adsorbed on the silanised glass slide without the Au NP film (Figure 5.6 d) is also shown in Table 5.5. From the Table 5.5, it is observed that the intensity I_1 of G1 from 10^{-4} is almost the same obtained from 10^{-6} M solution of uracil. The same is true with the intensity I_2 arising from G2 for both the concentrations ($10^{-4}$and 10^{-6} M). However, the intensity I_1 arising from G1 obtained from 10^{-2} M is higher than the other two concentrations, 10^{-4} and 10^{-6} M. Similarly, the intensity I_2 arising from G2 for 10^{-2} M solution is also higher than that obtained from the lower concentrations. This observation can be attributed to the formation of thick uracil films on G1 and G2 when dipped in higher concentration of 10^{-2} M. It is known that SEIRA is limited to the first monolayer directly attached to the metal NP surface and decays sharply within about 5 nm from the surface [261]. Therefore, the molecular layer close to the Au NP film exhibits more SEIRA intensity. However, the thickness of the formed uracil film will be more than monolayer, the absorption from the remaining layers of uracil becomes significant and give rise to the intense spectra. Hence I_1 of G1 and I_2 of G2 obtained from 10^{-2}M solution is high when compared to the lower concentrations. In the case of G3 film dipped in 10^{-2} M uracil solution, the intensity I_3 obtained is almost the same as that obtained for uracil adsorbed on silanised glass slide without Au NP film. This confirms that SEIRA phenomenon is not prevalent in the G3 film and the absorption spectrum is due to the formation of thick film which is detected in the ATR mode. To summarize, G1 gave ~ 3 times higher intensity for all the three concentrations of uracil than G2. The intensity ratio calculated for G1 with respect to G3 is ~5 for uracil concentration of 10^{-2} M. It may be recalled that G3 film didn't give any signal for 10^{-4}& 10^{-6} M solutions of uracil.

Table 5.5. Intensity of C2O7 stretch of uracil (1716 cm^{-1}) adsorbed on G1, G2, and G3

Concentration of uracil	**Intensity of C_2O_7 stretch of uracil**				**I_1/I_2**	**I_1/I_3**	**I_1/I_4**
	G1 (I_1)	**G2 (I_2)**	**G3 (I_3)**	**silanised glass without AuNP film (I_4)**			
10^{-2} M	0.005	0.002	0.001	0.001	2.5	5.0	5
10^{-4} M	0.003	0.001	-	0.000	3.0	-	-
10^{-6} M	0.003	0.001	-	0.000	3.0	-	-

5.3.4.2. EFFECT OF MORPHOLOGY ON THE SEIRA SPECTRA

In order to correlate the above results with the morphology of the films, AFM images of all the three films (G1, G2 & G3) were measured and shown in Figure 5.4. The RMS surface roughness, peak to peak height, ten point height for G1, G2 and G3 films are listed in Table 5.3. G1 film, which is obtained after ½ an hour of deposition time, is markedly different from G2 and G3 and its parameter are also different as it can be seen from the Table 5.3. There are reports which show that the SEIRA enhancement is closely related to the thickness and the morphology of the film [103, 112, 259]. The maximum SEIRA enhancement observed for silver films, obtained by physical deposition methods, is with thickness ranging from 5 nm to 20 nm [103, 112] and beyond this range the enhancement is decayed. The height of the nanoparticles of the G1 film, which governs the thickness of the film is 2.98 nm and hence has shown intense spectra when compared to G2 and G3. The G1 film has more voids surrounded by Au NP in a circular fashion. In the case of G2 and G3 film, almost all the AFM parameters have close by values except that the Au NP film is nearly continuous in G3 film when compared to G2. G2 has dense, yet separate particles but G3 film is nearly a closed

film. Apart from the thickness, the film morphology also plays an equally important role in the enhancement of the SEIRA signal. Enders et al. found that the strongest enhancement occurs at the percolation threshold of the flat nano-island film on silicon substrate prepared by wet-chemical deposition method [259]. The coalescence of the metal islands leads to dampening of the local plasma oscillations which consequently gives rise to reduction in the SEIRA signal [112]. In case of G3 film, with increase in the deposition time the Au NP grows to form a continuous film and hence G3 film did not serve as a good SEIRA substrate.

5.3.4.3. INTERPRETATION OF THE SEIRA SPECTRA

The peak positions of SEIRA spectra of uracil almost match with the IR absorption spectrum of uracil powder, as shown in Table 5.4. The negligible shift signifies weak interaction of the molecules with the Au NP film suggesting physisorption of the molecules on the film. Unlike our studies, S. Pronkin et al. [262] investigated the adsorption behaviour of uracil with varying potential at gold film electrode using spectro-electrochemical cell. They found that with increase in the positive potential the physisorbed molecules on the gold film electrode chemically binds through N3 of uracil showing large negative shift in the carbonyl stretches of the SEIRA spectrum. In our earlier IR studies of sodium benzoate and taurine on Au NP film, distinct changes in the vibrational modes of carboxylate and sulphonate groups respectively were observed [263]. New red-shifted bands appeared along with the stretches of carboxylate and sulphonate groups leading to the broadening of the above peaks indicating the presence of chemisorbed layer on the Au NP film.

5.3.5. CONCLUSION

SEIRA studies of uracil were carried out on wet-chemically prepared Au NP immobilized on silanised glass slides using ATR geometry. The negligible shift seen in the peak positions of

SEIRA spectra of uracil when compared to the IR spectrum of uracil powder signifies weak interaction of the molecules with the Au NP film suggesting physisorption occurring on the film. The deposition time dependent evolution of the morphological changes in Au NP films and its influence on the SEIRA spectra of uracil were investigated. The spectrum of uracil adsorbed on Au NP film obtained with ½ hr deposition time showed a clear enhancement than 2 and 4hrs deposition times. The film formed by 4 hrs deposition time is nearly a continuous film and served as poor SEIRA substrate.

CHAPTER 6.

SUMMARY AND FUTURE SCOPE

6.1. SUMMARY

Vibrational spectroscopy using Raman scattering and IR absorption has been considered as important and powerful tool for elucidation of molecular structure based on molecular vibrational fingerprint spectra. With the application of plasmonic materials, the strong electric field generated by the excitation of LSPR of plasmonic materials (particularly Ag and Au) has been exploited for enhancing the vibrational spectroscopic signal of molecules placed in the vicinity of metal NP, which has given rise to a new branch of spectroscopy called as surface enhanced spectroscopy. SERS was first demonstrated as enhanced vibrational spectroscopy followed by the discovery of alternative and complementary SEIRA spectroscopy technique. Both these techniques, collectively termed as SEVS, deal with spectroscopy of molecules placed in the vicinity of metal nanostructures. Thus SEVS has been proven to be an ultrasensitive and molecule specific spectroscopic technique which allows us to probe the molecule at ultra low concentration and provide the information about metal-adsorbate interaction, sites through which the interaction takes place and the molecular orientation on the metal surface. Apart from the enhanced localized electromagnetic field which forms the basis of SERS, the LSPR can also initiate various chemical reactions in molecules adsorbed on metal NP surface. The chemically transformed molecules gets easily detected and interpreted by the vibrational spectrum obtained with the help of sensitive SERS technique.

Molecular solids are found to undergo structural transitions, conformational changes, isomerization or even chemical transformations upon applying external pressure, and these changes can be probed with help of Raman spectroscopy. The metal-adsorbate interaction, the charge transfer process between metal and adsorbate are also affected under the application of pressure. Hence, to understand effect of pressure on the metal-adsorbate

systems, it would be worth to carry out high pressure Raman studies on molecular solid without metal to understand the behaviour of molecules in the absence of metal.

The thesis describes SEVS spectroscopic studies of various biologically important molecules using Ag and Au NP which will find applications in the field of bio-sensing, medical and forensic fields. The studies also include the other aspect of LSPR, the hot-electron driven chemical transformation of parent molecule adsorbed on to metal NP surface probed by the SERS. Additionally, it deals with the high pressure Raman studies of a biomolecule whose metal-adsorbate interaction on Ag surface is studied by SERS method and presented in the thesis. The significant results achieved in this research works, together with the conclusions and related future perspectives are summarized below.

Our initial work on the use of SERS for rapid identification of ultra low amounts of t-UCA, and deriving the information about molecular interaction/orientation with Ag metal surface shows the potential application of SERS. In the SERS study of t-UCA, an important UV chromophore and natural moisturising biomolecule present in skin, the near field enhancement of Ag NP due to excitation of LSPR allowed us to probe the vibrational spectroscopic features of t-UCA at physiological concentration. The reduced level concentration of t-UCA in the skin is an indicator of various skin disorders. Our SERS study presents the vibrational spectroscopic information of 50 picomolar of t-UCA in vitro phase. The results also provide the information about the molecular geometry on Ag NP surface, which is highly dependent on number density of t-UCA. At concentration of 50 μM, SERS features strongly suggest the chemical interaction of the molecule through the π electrons of the ethylenic bond and the carboxylate group with the molecule assuming a slightly tilted geometry on the Ag surface. While, at concentrations lower than 50 μM, the molecule assumes a flat geometrical orientation on the Ag surface. The present vitro phase SERS studies of t-UCA at physiological concentration and its interaction with metal NP would

provide the insights for researchers from the field of dermatology and will help in understanding the relation between skin disorder and biochemical changes in the skin.

Our high pressure Raman investigation on t-UCA up to ~14 GPa indicates the onset of ring opening polymerization involving the imidazole ring at pressure 1.4GPa, and on further compression, across 7.5 GPa the irreversible conformational transformation of t-UCA monomer into cis form was identified with help of appearance of characteristics vibrational (C=C stretch) mode of cis-UCA.

The SERS studies of thiazolidine-2 4-dione (TZD) emphasizes the plasmon-induced chemical reaction, plausibly induced by indirect hot-electron transfer mechanism, of the TZD molecule adsorbed on Ag NP. The SERS study of TZD provides the insights into the interaction between plasmon generated hot-electrons and molecules at metal surfaces which leads to formation of new compound. Our SERS results reveal that TZD on Ag NP surface undergo self condensation reaction and produces the TZD dimer product. The formation of TZD dimer on the Ag NP surface is evidenced by the presence of a prominent SERS peak at 1566 cm^{-1} attributed to ν C=C band of the dimer, which is further supported by the DFT calculated vibrational spectrum of TZD dimer and TZD dimer-Ag. The results indicate that the proximity of TZD molecules on the surface of Ag NP is a necessary factor for the dimerization to occur. At lower number density of molecules, most of the molecules lie apart and dimerization is less feasible, and the TZD molecules undergo deprotonation and get adsorbed on the Ag NP surface as anion (enolate). However, at higher concentrations the molecules are close enough to each other on the Ag NP surface for the dimerization reaction to take place, enabling the formation of TZD dimer. The TZD dimer formation is plausible induced by energetic transfer of hot-electron generated by non-radiative decay of LSPR and reaction mechanism involving the hot-electrons is presented.

The ATR-SEIRA spectroscopic studies of few important biomolecules like taurine, sodium benzoate and uracil are described. The SEIRA studies are focused on using wet chemically prepared Au NP films on glass substrate instead of using the films prepared by physical evaporation methods. Generally, metal films directly coated on ATR crystal are used for ATR-SEIRA studies, while we have used the non-coated ATR crystal for SEIRA studies. In the ATR-SEIRA studies of taurine and sodium benzoate, we have demonstrated the potential use of the wet chemically prepared Au NP film on non-conductive glass substrate (SEIRA active substrate) which can be placed over ATR crystal for SEIRA measurements. This was done to avoid the direct coating of metal film over the ATR crystal. We have also demonstrated that the current method is extremely useful to obtain vibrational spectrum of biological molecules present in the aqueous solution, which otherwise will not be possible due to the interference of strong water bands in IR region. The biological molecules present in aqueous solutions can be brought to the adsorbed state on these SEIRA substrates and can be probed and analyzed. From the ATR-SEIRA studies of sodium benzoate and taurine, new red-shifted bands are observed along with the symmetric and asymmetric stretches of carboxylate group of sodium benzoate. Similar behaviour is also seen in the case of symmetric and asymmetric stretches of sulphonate group of taurine. These results suggest the presence of both chemisorbed and physisorbed layers of both sodium benzoate and taurine on the Au NP film with bottom layer chemically bound to Au NP through carboxylate and sulphonate groups respectively.

In SEIRA study of uracil, the impact of morphology of wet-chemically fabricated Au NP films were investigated and results indicates that SEIRA intensity of adsorbed molecules is greatly affected by the Au NP film morphology. The SEIRA spectrum of uracil adsorbed on Au NP film obtained with ½ an hour deposition time showed a clear enhancement than 2 and 4 h deposition duration. The morphological structure obtained for 4 h deposition duration

indicates the coalescence of the metal islands which leads to dampening of the local surface plasmon oscillations, consequently gives rise to reduction in the SEIRA signal. With increase in the deposition time, the Au NP grows to form a continuous film and hence Au NP film obtained 4 h deposition time did not serve as a good SEIRA substrate. The small shift seen in SEIRA spectra indicates the weak interaction of the uracil with Au NP film.

6.2. FUTURE SCOPE

The future scope of the work presented in this thesis is not only on the applicative side, but is also relevant to the fundamental topic such as nanoplasmonic physics, wherein metal NP is considered as a efficient nanosource of hot-electrons/holes, light and electric field. Further works are required for better understanding of the generation of hot-carriers, relaxation dynamics of plasmonic materials and their utilization in molecular transformations for various important applications.

SERS under high pressure is another exciting area to investigate the effect of pressure on interfacial charge transfer (CT) between molecule and metal. The results and outcomes arising from the presented SERS and high pressure Raman studies of t-UCA in this thesis will be used for extending the SERS study under pressure. The obtained results will be helpful to understand the interaction mechanism between π electrons of molecules and SERS metal substrates under high pressure. The investigations of CT between molecule and metal has attracted much attention because of its vast applications [131]. There are some reports mainly focused on the CT process between molecule and substrate under pressure [130, 131]. Recently an anomalous Raman enhancement of R6G (Rhodamine) molecules adsorbed on MoS_2/Au substrate was observed up to 2.39 GPa, at which the degree of charge transfer between R6G molecule and MoS_2/Au substrate reaches a maximum [130]. Hence, the

combined effect of SERS and high pressure phenomenon can bring new insights and offer a new frontier in the research field of SERS.

Majority of SEVS studies rely on the usage of plasmonic metal nanostructures. However, it would be interesting to explore the organic semiconductor based SEVS substrate. These types of substrates are considered to be stable, reproducible and reusable, whereas SERS active substrates made from plasmonic metals have not been found to fit all these criteria. Recently, Yilmaz et al. [264] have extended the SERS studies by employing the metal free π-conjugated organic semiconductor substrate, α,ω-diperfluoro-hexylquaterthiophene (DFH-4T) and opened up a whole new area of research [264]. In their study, pristine DFH-4T films without any additional plasmonic layer exhibited unprecedented Raman signal enhancements up to ~10^3 and the chemical enhancement arising due to charge transfer between the DFH-4T surface and methylene blue (MB) molecules was considered as the dominant mechanism [264]. The combination of a DFH-4T film with a plasmonic Au metal film enabled the extremely low detection (<10^{-21} M) of MB molecule. Although, the results shown by Yilmaz et al. are very promising, further more research is needed on the class of organic semiconductor based SERS materials to study the interaction between adsorbate and substrate in detail. So far, this organic semiconductor based substrate has not been exploited in the field of SEIRA; hence application of organic semiconductor based substrate will certainly help to enhance the IR signal.

APPENDIX I

Table AI.1. Positional coordinates of various forms of t-UCA.

Positional coordinates of zwitterion of t-UCA			
Atom (nos.)	X	Y	Z
N (1)	-1.6595920	-1.0992460	-0.0013170
C (2)	-2.9611160	-0.9334930	-0.0006160
N(3)	-3.3083100	0.3910730	0.0009490
C (4)	-2.1253230	1.1126930	0.0011920
C (5)	-1.1027920	0.1784060	-0.0002740
C (6)	0.3266190	0.4627070	0.4627070
C (7)	1.3291510	-0.4332150	-0.0003260
C (8)	2.8101660	-0.0313980	0.0000790
O (9)	3.6127610	-1.0081300	0.0020110
O (10)	3.0673000	1.2043820	-0.0015680
H (11)	-4.2436370	0.7706850	0.0016060
H (12)	-3.7011500	-1.7244220	-0.0011820
H (13)	-2.1097460	2.1929240	0.0023450
H (14)	0.6108400	1.5154770	-0.0006930
H (15)	1.1182960	-1.5016680	-0.0004290
Positional coordinates of N3-H tautomer of t-UCA anion			
N (1)	-1.5756080	-0.9486980	-0.1625740
C (2)	-2.9160330	-0.9216930	-0.1506000
N(3)	-3.2735200	0.34243200	0.0869480
C (4)	-2.1485080	1.13861200	0.2268690
C (5)	-1.0391130	0.32351700	0.0634690
C (6)	0.3677270	0.60065900	0.0968630
C (7)	1.3285670	-0.2686140	-0.3003960
C (8)	2.8144180	-0.0556060	-0.0389660
O (9)	3.3391610	1.00788900	-0.4139430
O (10)	3.2607140	-1.0481670	0.5932410
H (11)	-4.2312380	0.66423200	0.1496990
H (12)	-3.5785980	-1.7604100	-0.2944650
H (13)	-1.0084360	-1.7802930	-0.2844380
H (14)	2.2151330	2.1981800	0.4133070
H (15)	0.6596460	1.58271700	0.4611160
H (16)	1.0763090	-1.2395950	-0.7336570
Positional coordinates of N1-H tautomer of t-UCA anion			
N (1)	1.6853700	-0.9855160	0.0003500
C (2)	3.0458900	-0.8478630	-0.0001830
N(3)	3.4050610	0.4205730	-0.0003220
C (4)	2.2195340	1.1270160	0.0000570
C (5)	1.1204070	0.2814110	0.0001190
C (6)	-0.3077320	0.5430940	0.0001660
C (7)	-1.2904420	-0.3770350	0.0001510
C (8)	-2.7873650	-0.0391440	0.0000740
O (9)	-3.0906910	1.1827160	-0.0001170
O (10)	-3.5396470	-1.0545660	-0.0002080
H (11)	1.1605250	-1.8487770	-0.0002270
H (12)	3.7166320	-1.6975540	-0.0001240
H (13)	2.2094840	2.2090870	0.0001130
H (14)	-0.6091240	1.5895370	0.0002080
H (15)	-1.0695870	-1.4477670	0.0001380

Table AI.2. Comparison of calculated and reported values (Page et. al. Ref [169]) of the optimized parameters of t-UCA zwitterions.

Bond length (Å)		
	Calculated	**Reported**
N(3)-C(2)	1.335	1.319
C(2)-N(1)	1.340	1.320
N(3)-C(4)	1.385	1.385
C(4)-C(5)	1.386	1.367
C(5)-N(1)	1.399	1.387
C(5)-C(6)	1.434	1.455
C(6)-C(7)	1.355	1.344
C(6)-C(8)	1.523	1.534
C(8)-O(10)	1.258	1.234
C(8)-O(9)	1.243	1.233
C(2)-H	1.078	1.068
C(4)-H	1.077	1.067
C(6)-H	1.087	1.074
C(7)-H	1.092	1.081
N(3)-H	1.012	0.997
N(1)-H	1.013	0.999
Angles (degree)		
N(3)-C(2)-N(1)	106.760	107.77
C(2)-N(3)-C(4)	110.16	109.42
N(3)-C(4)-C(5)	107.46	107.16
C(4)-C(5)-N(1)	104.28	104.88
C(5)-N(1)-C(2)	111.32	110.77
C(4)-C(5)-C(6)	131.95	131.50
C(5)-C(6)-C(7)	124.37	124.38
C(6)-C(7)-C(8)	123.46	122.45
C(7)-C(8)-O(10)	108.76	115.19
C(7)-C(8)-O(9)	118.63	113.10
N(1)-C(2)-H	126.67	126.10
C(2)-N(3)-H	124.42	124.71
N(3)-C(4)-H	122.15	122.17
C(5)-N(1)-H	123.41	124.17
C(5)-C(6)-H	116.46	116.93
C(6)-C(7)-H	121.49	122.26

Table AI.3. Comparison of calculated and reported values (Page et. al. Ref [169]) of the optimized parameters of N3-H tautomer of t-UCA anion.

Bond length (Å)		
	Calculated	**Reported**
N(1)-C(2)	1.312	1.329
C(2)-N(3)	1.369	1.370
N(2)-C(4)	1.385	1.380
C(2)-C(5)	1.385	1.390
C(5)-N(1)	1.393	1.391
C(5)-C(6)	1.457	1.456
C(6)-C(7)	1.344	1.349
C(7)-C(8)	1.534	1.527
C(8)-O(10)	1.264	1.271
C(8)-O(9)	1.262	1.273
C(2)-H	1.083	1.083
C(4)-H	1.080	1.082
C(6)-H	1.090	1.091
C(7)-H	1.089	1.090
N(3)-H	1.009	1.013
Angles (degree)		
N(3)-C(2)-N(1)	111.94	111.69
C(2)-N(3)-C(4)	106.695	107.10
N(3)-C(4)-C(5)	106.198	106.08
C(4)-C(5)-N(1)	108.870	109.20
C(5)-N(1)-C(2)	106.289	105.94
C(4)-C(5)-C(6)	126.333	126.32
C(5)-C(6)-C(7)	126.965	125.99
C(6)-C(7)-C(8)	123.034	122.28
C(7)-C(8)-O(10)	116.933	116.87
C(7)-C(8)-O(9)	114.230	114.19
N(1)-C(2)-H	125.838	125.83
C(2)-N(3)-H	126.778	126.53
N(3)-C(4)-H	122.209	122.36
C(5)-C(6)-H	116.357	117.23
C(6)-C(7)-H	120.622	120.65

Table AI.4. Positional coordinates of Ag complex of N3-H tautomer of t-UCA.

(a) Positional coordinates of Ag complex of N3-H tautomer of t-UCA (I)			
Atom (nos.)	X	Y	Z
N (1)	4.1134920	0.8484780	-0.0000960
C (2)	5.3130030	0.2687320	-0.0000060
N(3)	5.2066340	-1.1155330	-1.1155330
C (4)	3.8418450	-1.4222620	-0.0000400
C (5)	3.1643600	-0.2009310	-0.0000650
C (6)	1.7174740	-0.0178530	-0.0000570
C (7)	1.0548840	1.1638260	-0.0000440
C (8)	-0.4617590	1.2342710	1.2342710
O (9)	-1.0801490	-1.0801490	0.0003010
O (10)	-0.9899560	2.3977590	0.0000480
H (11)	5.9682920	-1.7786990	-1.7786990
H (12)	6.2618560	0.7844990	-0.0000120
H (13)	3.4699410	-2.4343570	-0.0000200
H (14)	1.1044670	-0.9190030	-0.0000060
H (15)	1.5835310	2.1152930	-0.0001110
Ag (16)	-3.2946160	-0.4646830	-0.0000310
(b) Positional coordinates of Ag complex of N3-H tautomer of t-UCA (II)			
N (1)	-3.5405240	0.7337110	-0.3100360
C (2)	-4.6140580	-0.0553060	-0.3084360
N(3)	-4.2928640	-1.3464780	0.0883530
C (4)	-2.9197480	-1.3651780	0.3536050
C (5)	-2.4544240	-0.0724980	0.1049490
C (6)	-1.0767740	0.3885490	0.2399920
C (7)	-0.6211230	1.6349560	-0.0300970
C (8)	0.8308860	2.0482200	0.1288220
O (9)	1.6953290	1.1369550	0.5176120
O (10)	1.0961300	3.2760270	-0.1133990
H (11)	-4.9269540	-2.1285780	0.1666360
H (12)	-5.6162560	0.2443200	-0.5771640
H (13)	-2.3960890	-2.2519340	0.6734200
H (14)	-0.3530460	-0.3508310	0.5845760
H (15)	1.2962310	2.4156920	-0.3759270
Ag (16)	2.3877040	-0.9450130	-0.1082230
(c) Positional coordinates of Ag complex of N3-H tautomer of t-UCA(III)			
N (1)	0.9882410	0.8969060	0.0000290
C (2)	2.0130660	1.7550390	0.0003330
N(3)	1.5613350	3.0562450	0.0000410
C (4)	0.1610770	3.0150030	0.0000590
C (5)	-0.2031380	1.6664390	0.0001030
C (6)	-1.5635100	1.1461780	0.0001560
C (7)	-1.9610010	-0.1493350	0.0001970
C (8)	-3.4498650	-0.5289430	0.0000550
O (9)	-4.2949190	0.4493440	-0.0010050
O (10)	-3.6787200	-1.8000750	0.0009040
H (11)	2.1352030	3.8872780	-0.0000230
H (12)	3.0572320	1.4827030	0.0005120
H (13)	-0.4502640	3.9026530	0.0000750
H (14)	2.3684100	1.8826390	0.0000190
H (15)	-1.2530750	-0.9811040	0.0000020
Ag (16)	1.5923750	-1.4567370	-0.0001210

(d) Positional coordinates of Ag_4 complex of N3-H tautomer of t-UCA(IV)			
N (1)	5.2914730	0.5332820	1.1205520
C (2)	5.9287650	-0.4337220	1.7790310
N(3)	5.2263210	-1.6306260	1.7239520
C (4)	4.0685580	-1.3957380	0.9787970
C (5)	4.1119560	-0.0513610	0.6060570
C (6)	3.1072870	0.6537530	-0.1814090
C (7)	3.1358360	1.9644960	-0.5204540
C (8)	2.0735590	2.6439330	-1.3561010
O (9)	0.9855940	1.9605970	-1.6744640
O (10)	2.3124350	3.8363060	-1.7305330
H (11)	5.4958650	-2.5079050	2.1457350
H (12)	6.8702240	-0.3282010	2.2971390
H (13)	3.3292320	-2.1564650	0.7825030
H (14)	2.2672310	0.0481410	-0.5220880
H (15)	3.9657320	2.5996620	-0.2177270
Ag (16)	-0.4484260	0.6950700	-0.6456230
Ag (17)	-0.2406400	-2.3096110	-1.0513410
Ag (18)	-2.6314500	1.5205510	1.0889670
Ag (19)	-2.1367790	-1.1110570	0.5017710
(e) Positional coordinates of Ag_4 complex of N3-H tautomer of t-UCA(V)			
N (1)	1.1401300	2.4232850	0.1031320
C (2)	0.6409090	3.6632120	0.0993270
N(3)	1.6480930	4.5867750	-0.0668950
C (4)	2.8563290	3.8873070	-0.1755060
C (5)	2.5434540	2.5349920	-0.0607660
C (6)	3.4461830	1.3873560	-0.1261560
C (7)	3.1089130	0.1516870	0.3090120
C (8)	3.9399410	-1.0973400	0.0813760
O (9)	5.1882420	-0.9899180	-0.1362080
O (10)	3.2333270	-2.2121790	0.0983590
H (11)	1.5301610	5.5889630	-0.1138610
H (12)	-0.4062480	3.9096820	0.1887100
H (13)	3.8066300	4.3791760	-0.3046170
H (14)	4.4265350	1.5358210	-0.5764070
H (15)	2.1471290	-0.0050960	0.7959350
Ag (16)	-0.3513230	0.6511220	0.0488360
Ag (17)	0.9529680	-2.1953170	-0.0008370
Ag (18)	-3.1101100	1.0562260	0.0058970
Ag (19)	-1.6959750	-1.6827850	-0.0688820

Table AI.5. Positional coordinates of Ag complex of N1-H tautomer of t-UCA.

(a) Positional coordinates of Ag complex of N1-H tautomer of t-UCA (I)			
Atom (nos.)	X	Y	Z
N (1)	-3.8516580	0.9564830	0.0000810
C (2)	-5.2360300	0.7604260	0.0000290
N(3)	-5.5310020	-0.5471250	-0.0000210
C (4)	-4.3081790	-1.2188540	-0.0001530
C (5)	-3.2146940	-0.3090810	-0.0000280
C (6)	-1.8043460	-0.5029370	-0.0000370
C (7)	-0.8328960	0.5295350	0.0000870
C (8)	0.5703990	0.3015520	0.0000660
O (9)	1.0893860	-0.9454510	0.0002660
O (10)	1.4349030	1.3453630	-0.0001990
H (11)	-3.3631640	1.8393270	0.0001620
H (12)	-5.9517630	1.5691780	0.0000930
H (13)	-4.2608930	-2.2979750	-0.0002740
H (14)	-1.4456400	-1.5290080	-0.0001590
H (15)	-1.1281850	1.5787410	0.0002060
Ag (16)	3.2040090	-0.0976360	-0.0000160
(b) Positional coordinates of Ag complex of N1-H tautomer of t-UCA(II)			
N (1)	3.5432490	0.5797060	-0.3253880
C (2)	4.6733410	-0.2211680	-0.3202750
N(3)	4.3880710	-1.4547560	0.1152060
C (4)	3.0179900	-1.4414970	0.3994250
C (5)	2.4611870	-0.1860290	0.1355200
C (6)	1.0973150	0.3020280	0.2722890
C (7)	0.6642340	1.5576030	-0.0065960
C (8)	-0.7714410	2.0267010	0.1496530
O (9)	-1.6640960	1.1514920	0.5403470
O (10)	-0.9760800	3.2648680	-0.1038110
H (11)	3.4851950	1.5469110	-0.6125170
H (12)	5.6474570	0.1239200	-0.6325440
H (13)	2.5106210	-2.3203350	0.7672750
H (14)	0.3637430	-0.4192700	0.6289400
H (15)	1.3392580	2.3394360	-0.3637270
Ag (16)	-2.4382950	-0.9085530	-0.1189050
N (1)	3.5432490	0.5797060	-0.3253880
C (2)	4.6733410	-0.2211680	-0.3202750
N(3)	4.3880710	-1.4547560	0.1152060
C (4)	3.0179900	-1.4414970	0.3994250
(c) Positional coordinates of Ag complex of N1-H tautomer of t-UCA(III)			
N (1)	-0.7788780	1.4124570	-0.0004010
C (2)	0.5956310	1.5097790	0.0003070
N(3)	1.1438170	0.2866530	0.0010400
C (4)	0.0802700	-0.6251510	0.0010490
C (5)	-1.1399700	0.0542840	0.0000610
C (6)	-2.5117640	-0.4306670	-0.0002200
C (7)	-3.6313350	0.3365180	0.0001580
C (8)	-5.0455090	-0.2595230	-0.0001550
O (9)	-5.1296840	-1.5455540	-0.0002690
O (10)	-5.9855720	0.6281670	-0.0001110
H (11)	-1.4408320	2.1770290	-0.0013970
H (12)	1.1368420	2.4423780	0.0002490
H (13)	0.2459140	-1.6902850	0.0018420
H (14)	-2.6629650	-1.5085620	-0.0006490
H (15)	-3.5982830	1.4309420	0.0010020

APPENDIX II

1. Density functional theory (DFT)

DFT, a computational quantum mechanical calculation method, is used to investigate the many body system particularly atoms, molecules and condensed phases. The ground state properties and potential energies are accurately calculated by DFT method. Therefore, DFT has become a powerful tool in computational chemistry to predict the vibrational frequencies of simple to very complex molecular systems [265]. These DFT calculated frequencies help in assigning the vibrational modes and interpretating the experimental Raman/IR spectra. The concept of DFT method is relied on the Hohenberg-Kohn theorem, which states that the total energy of a system in its ground state is a functional of system's electronic density, ρ(r) [266]. In DFT the total energy, including electron correlation effects, is expressed in the form of electron density and written as:

$$E[\rho(r)] = T[\rho(r)] + U[\rho(r)] + E_{XC}[\rho(r)]$$

Here, *T* describes the kinetic energy term of electrons, *U* is the electrostatic interaction energy between all electrons and nuclei, and E_{XC} is the exchange-correlation energy term of the system. Using the electron density significantly speeds up the calculation. The many-body electronic wavefunction is a function of 3N variables, whereas the electron density is only a function of three variables *x, y, z.* The total electron density $\rho(r)$ can be related to single-particle wave functions and given by:

$$\rho(r) = \sum |\psi(r)|^2$$

The first step of DFT calculation is the geometry optimization of isolated single molecule. Initial structure of molecule is taken from the literature. Geometry optimization starts with solving the Kohn-Sham equation [267] on the initial geometry and energy and force on the molecule are calculated from the solution. In geometry optimization, we attempt

to find the configuration of minimum energy of the molecule. An optimized geometry will have minimum energy and zero force on the molecule.

Once optimized geometry is computed, the equilibrium atomic positions of the atoms are known. After this, the interaction of the atoms is identified which allow the calculation of force constants. These force constants are used to calculate the vibrational frequencies.

2. Vibrational frequency calculation using Gaussian software

Gaussian is the most frequently used computational chemistry software. The computation of vibrational spectra of molecules in their ground and excited states can be done by using the Gaussian program. Gauss View, a graphical user interface for Gaussian, is used to submit inputs and to see the generated output files. For Raman/IR spectrum calculations using Gaussian, the following steps are required [268]:

i. Build molecule in Gauss View interface. Go to Calculate from Gauss View toolbar and select Gaussian calculation set up. From the opened menu, in the job type section, select Opt + Freq, optimize to a Minimum, Calculate Force Constants-Never, Compute Raman- Yes, and deselect any other option.

ii. In Method section, select ground state, select a basis set, charge and spin-Singlet. After this submit the calculation.

iii. Open the output file of the optimized structure in Gauss View. Verify the convergence of all the parameters (maximum force, RMS force, maximum displacement and RMS displacement) after the geometry optimization calculation.

iv. Go to Results and select the 'vibrations' option to view the Raman/IR spectrum and its vibrational modes.

REFERENCES

[1] S.F. Parker, D. Lennon, P.W. Albers, Vibrational spectroscopy with neutrons: A review of new directions, Appl. Spectrosc., 65 (2011) 1325-1341.

[2] G.C. Schatz, R.P. Van Duyne, Handbook of vibrational spectroscopy, New York: Wiley, 1 (2002) 759.

[3] J.M. Hollas, Modern spectroscopy, John Wiley & Sons, 2004.

[4] P.R. Griffiths, J.A. De Haseth, Fourier transform infrared spectrometry, John Wiley & Sons, 2007.

[5] J.R. Ferraro, Introductory raman spectroscopy, Elsevier, 2003.

[6] C.V. Raman, K.S. Krishnan, A new type of secondary radiation, Nature, 121 (1928) 501-502.

[7] J. Coates, Interpretation of infrared spectra, a practical approach, Encyclopedia of analytical chemistry: applications, theory and instrumentation, (2006).

[8] F. Neubrech, C. Huck, K. Weber, A. Pucci, H. Giessen, Surface-enhanced infrared spectroscopy using resonant nanoantennas, Chem. Rev., 117 (2017) 5110-5145.

[9] S.A. Meyer, E.C.L. Ru, P.G. Etchegoin, Quantifying resonant Raman cross sections with SERS, J. Phys. Chem. A, 114 (2010) 5515-5519.

[10] A. Kudelski, Characterization of thiolate-based mono-and bilayers by vibrational spectroscopy: A review, Vib. Spectrosc., 39 (2005) 200-213.

[11] K.B. Biggs, J.P. Camden, J.N. Anker, R.P.V. Duyne, Surface-enhanced Raman spectroscopy of benzenethiol adsorbed from the gas phase onto silver film over nanosphere surfaces: determination of the sticking probability and detection limit time, J. Phys. Chem. A, 113 (2009) 4581-4586.

[12] R. Aroca, Surface-enhanced vibrational spectroscopy, John Wiley & Sons, 2006.

[13] M. Fleischmann, P.J. Hendra, A.J. McQuillan, Raman spectra of pyridine adsorbed at a silver electrode, Chem. Phys. Lett., 26 (1974) 163-166.

[14] D.L. Jeanmaire, R.P. Van Duyne, Surface Raman spectroelectrochemistry: Part I. Heterocyclic, aromatic, and aliphatic amines adsorbed on the anodized silver electrode, J. electroanal. chem. interfacial electrochem., 84 (1977) 1-20.

[15] M.G. Albrecht, J.A. Creighton, Anomalously intense Raman spectra of pyridine at a silver electrode, J. Am. Chem. Soc., 99 (1977) 5215-5217.

[16] A. Hartstein, J. Kirtley, J. Tsang, Enhancement of the infrared absorption from molecular monolayers with thin metal overlayers, Phys. Rev. Lett., 45 (1980) 201-204.

[17] P.K. Jain, X. Huang, I.H. El-Sayed, M.A. El-Sayed, Noble metals on the nanoscale: optical and photothermal properties and some applications in imaging, sensing, biology, and medicine, Acc. Chem. Res., 41 (2008) 1578-1586.

[18] V.V. Mody, R. Siwale, A. Singh, H.R. Mody, Introduction to metallic nanoparticles, J. Pharm. Bioallied Sci., 2 (2010) 282-289.

[19] M. Holzinger, A. Le Goff, S. Cosnier, Nanomaterials for biosensing applications: a review, Frontiers in Chemistry, 2 (2014) 1-10.

[20] M.A. García, Surface plasmons in metallic nanoparticles: fundamentals and applications, J. Phys. D: Appl. Phys., 44 (2011) 283001-283020.

[21] K. Watanabe, D. Menzel, N. Nilius, H.-J. Freund, Photochemistry on metal nanoparticles, Chem. Rev., 106 (2006) 4301-4320.

[22] X.-Y. Dong, Z.-W. Gao, K.-F. Yang, W.-Q. Zhang, L.-W. Xu, Nanosilver as a new generation of silver catalysts in organic transformations for efficient synthesis of fine chemicals, Catal. Sci. Technol., 5 (2015) 2554-2574.

[23] K.L. Kelly, E. Coronado, L.L. Zhao, G.C. Schatz, The optical properties of metal nanoparticles: the influence of size, shape, and dielectric environment, in, J. Phys. Chem. B, 2003, pp. 668-677.

[24] K.A. Willets, R.P. Van Duyne, Localized surface plasmon resonance spectroscopy and sensing, Annu. Rev. Phys. Chem., 58 (2007) 267-297.

[25] C.S. Levin, J. Kundu, A. Barhoumi, N.J. Halas, Nanoshell-based substrates for surface enhanced spectroscopic detection of biomolecules, Analyst, 134 (2009) 1745-1750.

[26] M. Jahn, S. Patze, I.J. Hidi, R. Knipper, A.I. Radu, A. Mühlig, S. Yüksel, V. Peksa, K. Weber, T. Mayerhöfer, Plasmonic nanostructures for surface enhanced spectroscopic methods, Analyst, 141 (2016) 756-793.

[27] L. Jensen, C.M. Aikens, G.C. Schatz, Electronic structure methods for studying surface-enhanced Raman scattering, Chem. Soc. Rev., 37 (2008) 1061-1073.

[28] C. D'Andrea, J. Bochterle, A. Toma, C. Huck, F. Neubrech, E. Messina, B. Fazio, O.M. Marago, E. Di Fabrizio, M. Lamy de La Chapelle, Optical nanoantennas for multiband surface-enhanced infrared and Raman spectroscopy, ACS nano, 7 (2013) 3522-3531.

[29] W. Xie, S. Schlucker, Medical applications of surface-enhanced Raman scattering, Phys. Chem. Chem. Phys., 15 (2013) 5329-5344.

[30] K. Ataka, J. Heberle, Biochemical applications of surface-enhanced infrared absorption spectroscopy, Anal. Bioanal. Chem., 388 (2007) 47-54.

[31] S. Schlücker, Surface-Enhanced raman spectroscopy: Concepts and chemical applications, Angew. Chem. Int. Ed., 53 (2014) 4756-4795.

[32] E. Podstawka, Y. Ozaki, L.M. Proniewicz, Part III: Surface-enhanced Raman scattering of amino acids and their homodipeptide monolayers deposited onto colloidal gold surface, Appl. Spectrosc., 59 (2005) 1516-1526.

[33] W. Ren, Y. Fang, E. Wang, A Binary Functional Substrate for Enrichment and Ultrasensitive SERS Spectroscopic Detection of Folic Acid Using Graphene Oxide/Ag Nanoparticle Hybrids, ACS Nano, 5 (2011) 6425-6433.

[34] L. Yang, C. Du, X. Luo, Rapid glucose detection by surface enhanced Raman scattering spectroscopy, J Nanosci Nanotechnol, 9 (2009) 2660-2663.

[35] A. Ceja-Fdez, T. Lopez-Luke, A. Torres-Castro, D.A. Wheeler, J.Z. Zhang, E. De la Rosa, Glucose detection using SERS with multi-branched gold nanostructures in aqueous medium, RSC Advances, 4 (2014) 59233-59241.

[36] Y.C. Cao, R. Jin, C.A. Mirkin, Nanoparticles with Raman spectroscopic fingerprints for DNA and RNA detection, Science, 297 (2002) 1536-1540.

[37] T. Kang, S.M. Yoo, I. Yoon, S.Y. Lee, B. Kim, Patterned Multiplex Pathogen DNA Detection by Au Particle-on-Wire SERS Sensor, Nano Lett., 10 (2010) 1189-1193.

[38] R.M. Jarvis, A. Brooker, R. Goodacre, Surface-enhanced Raman spectroscopy for bacterial discrimination utilizing a scanning electron microscope with a Raman spectroscopy interface, Anal. Chem., 76 (2004) 5198-5202.

[39] S. Shanmukh, L. Jones, J. Driskell, Y. Zhao, R. Dluhy, R.A. Tripp, Rapid and sensitive detection of respiratory virus molecular signatures using a silver nanorod array SERS substrate, Nano Lett., 6 (2006) 2630-2636.

[40] J.D. Driskell, K.M. Kwarta, R.J. Lipert, M.D. Porter, J.D. Neill, J.F. Ridpath, Low-level detection of viral pathogens by a surface-enhanced Raman scattering based immunoassay, Anal. Chem., 77 (2005) 6147-6154.

[41] W.Y. Wei, I.M. White, Inkjet-printed paper-based SERS dipsticks and swabs for trace chemical detection, Analyst, 138 (2013) 1020-1025.

[42] W. Xie, S. Schluecker, Rationally designed multifunctional plasmonic nanostructures for surface-enhanced Raman spectroscopy: a review, Rep. Prog. Phys., 77 (2014) 116502-116524.

[43] J. Zheng, L. He, Surface-enhanced Raman spectroscopy for the chemical analysis of food, Compr. Rev. Food Sci. Food Saf., 13 (2014) 317-328.

[44] J.F. Li, Y.F. Huang, Y. Ding, Z.L. Yang, S.B. Li, X.S. Zhou, F.R. Fan, W. Zhang, Z.Y. Zhou, B. Ren, Shell-isolated nanoparticle-enhanced Raman spectroscopy, Nature, 464 (2010) 392-395.

[45] D.-W. Li, W.-L. Zhai, Y.-T. Li, Y.-T. Long, Recent progress in surface enhanced Raman spectroscopy for the detection of environmental pollutants, Microchimica Acta, 181 (2014) 23-43.

[46] M. Moskovits, Surface-enhanced spectroscopy, Rev. Mod. Phys., 57 (1985) 783-826.

[47] B. Sharma, R.R. Frontiera, A.-I. Henry, E. Ringe, R.P. Van Duyne, SERS: Materials, applications, and the future, Mater. Today, 15 (2012) 16-25.

[48] A. Campion, P. Kambhampati, Surface-enhanced Raman scattering, Chem. Soc. Rev., 27 (1998) 241-250.

[49] N. Kumar, S. Thomas, R. Rao, N. Maiti, R.J. Kshirsagar, Surface-enhanced Raman scattering based sensing of trans-urocanic acid, an epidermal photoreceptor using silver nanoparticles aided by density functional theoretical calculations, J. Raman Spectrosc., 50 (2019) 837-846.

[50] S. Thomas, N. Biswas, S. Venkateswaran, S. Kapoor, R. D'Cunha, T. Mukherjee, Raman, infrared, SERS and DFT calculations of a triazole derivative (akacid), Chem. Phys. Lett., 402 (2005) 361-366.

[51] S. Thomas, N. Biswas, S. Venkateswaran, S. Kapoor, S. Naumov, T. Mukherjee, Studies on adsorption of 5-amino tetrazole on silver nanoparticles by SERS and DFT calculations, The Journal of Physical Chemistry A, 109 (2005) 9928-9934.

[52] N. Maiti, S. Thomas, A. Debnath, S. Kapoor, Raman and XPS study on the interaction of taurine with silver nanoparticles, RSC Advances, 6 (2016) 56406-56411.

[53] N. Maiti, S. Thomas, J.A. Jacob, R. Chadha, T. Mukherjee, S. Kapoor, DFT and surface-enhanced Raman scattering study of tryptophan–silver complex, J. Colloid Interface Sci., 380 (2012) 141-149.

[54] N. Biswas, S. Thomas, A. Sarkar, T. Mukherjee, S. Kapoor, Adsorption of methimazole on silver nanoparticles: FTIR, Raman, and surface-enhanced Raman scattering study aided by density functional theory, J. Phys. Chem. C, 113 (2009) 7091-7100.

[55] M. Moskovits, Surface selection rules, J. Chem. Phys., 77 (1982) 4408-4416.

[56] M. Moskovits, J.S. Suh, Surface selection rules for surface-enhanced Raman spectroscopy: calculations and application to the surface-enhanced Raman spectrum of phthalazine on silver, J. Phys. Chem., 88 (1984) 5526-5530.

[57] M. Moskovits, J.S. Suh, The geometry of several molecular ions adsorbed on the surface of colloidal silver, The Journal of Physical Chemistry, 88 (1984) 1293-1298.

[58] M. Moskovits, J.S. Suh, Surface geometry change in 2-naphthoic acid adsorbed on silver, J. Phys. Chem., 92 (1988) 6327-6329.

[59] M. Moskovits, J.S. Suh, Conformation of mono- and dicarboxylic acids adsorbed on silver surfaces, J. Am. Chem. Soc., 107 (1985) 6826-6829.

[60] E. Katz, I. Willner, Integrated nanoparticle–biomolecule hybrid systems: synthesis, properties, and applications, Angew. Chem. Int. Ed., 43 (2004) 6042-6108.

[61] N.L. Rosi, C.A. Mirkin, Nanostructures in biodiagnostics, Chem. Rev., 105 (2005) 1547-1562.

[62] Basic Electromagnetic Theory of SERS, in: Surface Enhanced Raman Spectroscopy, pp. 1-37.

[63] P.L. Stiles, J.A. Dieringer, N.C. Shah, R.P. Van Duyne, Surface-enhanced Raman spectroscopy, Annu. Rev. Anal. Chem., 1 (2008) 601-626.

[64] P.K. Jain, K.S. Lee, I.H. El-Sayed, M.A. El-Sayed, Calculated absorption and scattering properties of gold nanoparticles of different size, shape, and composition: applications in biological imaging and biomedicine, J. Phys. Chem. B, 110 (2006) 7238-7248.

[65] J.M. McMahon, Y. Wang, L.J. Sherry, R.P. Van Duyne, L.D. Marks, S.K. Gray, G.C. Schatz, Correlating the structure, optical spectra, and electrodynamics of single silver nanocubes, J. Phys. Chem. C, 113 (2009) 2731-2735.

[66] S.P. Centeno, I. Lopez-Tocon, J. Roman-Perez, J.F. Arenas, J. Soto, J.C. Otero, Franck–condon dominates the surface-enhanced Raman scattering of 3-methylpyridine: propensity rules of the charge-transfer mechanism under reduced symmetry, J. Phys. Chem. C, 116 (2012) 23639-23645.

[67] W.B. Caldwell, K. Chen, B.R. Herr, C.A. Mirkin, J.C. Hulteen, R.P. Van Duyne, Self-assembled monolayers of ferrocenylazobenzenes on Au (111)/mica films: surface-enhanced Raman scattering response vs surface morphology, Langmuir, 10 (1994) 4109-4115.

[68] Y.-F. Huang, H.-P. Zhu, G.-K. Liu, D.-Y. Wu, B. Ren, Z.-Q. Tian, When the signal is not from the original molecule to be detected: chemical transformation of para-aminothiophenol on Ag during the SERS measurement, J. Am. Chem. Soc., 132 (2010) 9244-9246.

[69] D.-Y. Wu, X.-M. Liu, Y.-F. Huang, B. Ren, X. Xu, Z.-Q. Tian, Surface catalytic coupling reaction of p-mercaptoaniline linking to silver nanostructures responsible for abnormal SERS enhancement: a DFT study, J. Phys. Chem. C, 113 (2009) 18212-18222.

[70] S. Mukherjee, L. Zhou, A.M. Goodman, N. Large, C. Ayala-Orozco, Y. Zhang, P. Nordlander, N.J. Halas, Hot-electron-induced dissociation of H_2 on gold nanoparticles supported on SiO_2, J. Am. Chem. Soc., 136 (2013) 64-67.

[71] E. Kazuma, J. Jung, H. Ueba, M. Trenary, Y. Kim, Real-space and real-time observation of a plasmon-induced chemical reaction of a single molecule, Science, 360 (2018) 521-526.

[72] E. Kazuma, J. Jung, H. Ueba, M. Trenary, Y. Kim, Direct pathway to molecular photodissociation on metal surfaces using visible light, J. Am. Chem. Soc., 139 (2017) 3115-3121.

[73] C. Boerigter, R. Campana, M. Morabito, S. Linic, Evidence and implications of direct charge excitation as the dominant mechanism in plasmon-mediated photocatalysis, Nat. Commun., 7 (2016) 10545 (10541-10549).

[74] S. Mukherjee, L. Zhou, A.M. Goodman, N. Large, C. Ayala-Orozco, Y. Zhang, P. Nordlander, N.J. Halas, Hot-electron-induced dissociation of H_2 on gold nanoparticles supported on SiO_2, J. Am. Chem. Soc., 136 (2014) 64-67.

[75] P. Christopher, H. Xin, S. Linic, Visible-light-enhanced catalytic oxidation reactions on plasmonic silver nanostructures, Nat. Chem., 3 (2011) 467-472.

[76] P. Singh, V. Deckert, Local protonation control using plasmonic activation, Chem. Commun., 50 (2014) 11204-11207.

[77] M. Sun, H. Xu, A novel application of plasmonics: plasmon-driven surface-catalyzed reactions, Small, 8 (2012) 2777-2786.

[78] M. Xiao, R. Jiang, F. Wang, C. Fang, J. Wang, C.Y. Jimmy, Plasmon-enhanced chemical reactions, J. Mater. Chem. A, 1 (2013) 5790-5805.

[79] E. Kazuma, Y. Kim, Mechanistic Studies of Plasmon Chemistry on Metal Catalysts, Angew. Chem. Int. Ed., 58 (2019) 4800-4808.

[80] C. Zhan, M. Moskovits, Z.-Q. Tian, Recent Progress and Prospects in Plasmon-Mediated Chemical Reaction, Matter, 3 (2020) 42-56.

[81] S. Linic, U. Aslam, C. Boerigter, M. Morabito, Photochemical transformations on plasmonic metal nanoparticles, Nat. Mater., 14 (2015) 567-576.

[82] M.L. Brongersma, N.J. Halas, P. Nordlander, Plasmon-induced hot carrier science and technology, Nat. Nanotechnol., 10 (2015) 25-34.

[83] J.R. Adleman, D.A. Boyd, D.G. Goodwin, D. Psaltis, Heterogenous catalysis mediated by plasmon heating, Nano Lett., 9 (2009) 4417-4423.

[84] A. Manjavacas, J.G. Liu, V. Kulkarni, P. Nordlander, Plasmon-induced hot carriers in metallic nanoparticles, ACS nano, 8 (2014) 7630-7638.

[85] G.V. Hartland, L.V. Besteiro, P. Johns, A.O. Govorov, What's so hot about electrons in metal nanoparticles?, ACS Energy Letters, 2 (2017) 1641-1653.

[86] A.O. Govorov, H. Zhang, Y.K. Gun'ko, Theory of photoinjection of hot plasmonic carriers from metal nanostructures into semiconductors and surface molecules, J. Phys. Chem. C, 117 (2013) 16616-16631.

[87] G. Baffou, R. Quidant, Nanoplasmonics for chemistry, Chem. Soc. Rev., 43 (2014) 3898-3907.

[88] E.C. Le Ru, P.G. Etchegoin, Quantifying SERS enhancements, MRSBu, 38 (2013) 631-640.

[89] M. Osawa, Surface-enhanced infrared absorption, in: Near-field optics and surface plasmon polaritons, Springer, 2001, pp. 163-187.

[90] W.C. Chan, Bio-applications of Nanoparticles, Springer Science & Business Media, 2009.

[91] R.F. Aroca, D.J. Ross, C. Domingo, Surface-enhanced infrared spectroscopy, Appl. Spectrosc., 58 (2004) 324A-338A.

[92] N. Kumar, S. Thomas, R. Tokas, R. Kshirsagar, SEIRA studies of uracil adsorbed on wet-chemically prepared gold nanoparticles film on glass substrate–Effect of morphology of film, Spectrochimica Acta Part A: Molecular and Biomolecular Spectroscopy, 129 (2014) 359-364.

[93] C.W. Brown, Y. Li, J.A. Seelenbinder, P. Pivarnik, A.G. Rand, S.V. Letcher, O.J. Gregory, M.J. Platek, Immunoassays based on surface-enhanced infrared absorption spectroscopy, Anal. Chem., 70 (1998) 2991-2996.

[94] K.B. Alici, Hybridization of Fano and vibrational resonances in surface-enhanced infrared absorption spectroscopy of streptavidin monolayers on metamaterial substrates, IEEE Transactions on Nanotechnology, 13 (2014) 216-221.

[95] C. Wu, A.B. Khanikaev, R. Adato, N. Arju, A.A. Yanik, H. Altug, G. Shvets, Fano-resonant asymmetric metamaterials for ultrasensitive spectroscopy and identification of molecular monolayers, Nat. Mater., 11 (2012) 69-75.

[96] S. Sanchez-Cortes, C. Domingo, J. Garcia-Ramos, J. Aznarez, Surface-enhanced vibrational study (SEIR and SERS) of dithiocarbamate pesticides on gold films, Langmuir, 17 (2001) 1157-1162.

[97] D. Ross, R. Aroca, Effective medium theories in surface enhanced infrared spectroscopy: the pentacene example, J. Chem. Phys., 117 (2002) 8095-8103.

[98] F. Le, D.W. Brandl, Y.A. Urzhumov, H. Wang, J. Kundu, N.J. Halas, J. Aizpurua, P. Nordlander, Metallic nanoparticle arrays: a common substrate for both surface-enhanced Raman scattering and surface-enhanced infrared absorption, ACS nano, 2 (2008) 707-718.

[99] E. Prodan, C. Radloff, N.J. Halas, P. Nordlander, A hybridization model for the plasmon response of complex nanostructures, Science, 302 (2003) 419-422.

[100] P. Nordlander, E. Prodan, Plasmon hybridization in nanoparticles near metallic surfaces, Nano Lett., 4 (2004) 2209-2213.

[101] Y. Nishikawa, T. Nagasawa, K. Fujiwara, M. Osawa, Silver island films for surface-enhanced infrared absorption spectroscopy: effect of island morphology on the absorption enhancement, Vib. Spectrosc., 6 (1993) 43-53.

[102] J. Yang, P.R. Griffiths, Preparation and characterization by surface-enhanced infrared absorption spectroscopy of silver nanoparticles formed on germanium substrates by electroless displacement, Anal. Bioanal. Chem., 388 (2007) 109-119.

[103] M. Osawa, Dynamic processes in electrochemical reactions studied by surface-enhanced infrared absorption spectroscopy (SEIRAS), Bull. Chem. Soc. Jpn., 70 (1997) 2861-2880.

[104] A. Priebe, M. Sinther, G. Fahsold, A. Pucci, The correlation between film thickness and adsorbate line shape in surface enhanced infrared absorption, J. Chem. Phys., 119 (2003) 4887-4890.

[105] A. Hatta, Y. Suzuki, W. Suëtaka, Infrared absorption enhancement of monolayer species on thin evaporated Ag films by use of a Kretschmann configuration: Evidence for two types of enhanced surface electric fields, Appl. Phys. A, 35 (1984) 135-140.

[106] T. Kamata, A. Kato, J. Umemura, T. Takenaka, Intensity enhancement of infrared attenuated total reflection spectra of stearic acid Langmuir-Blodgett monolayers with evaporated silver island films, Langmuir, 3 (1987) 1150-1154.

[107] M. Osawa, K.-i. Ataka, K. Yoshii, T. Yotsuyanagi, Surface-enhanced infrared ATR spectroscopy for in situ studies of electrode/electrolyte interfaces, J. Electron. Spectrosc. Relat. Phenom., 64 (1993) 371-379.

[108] M. Osawa, M. Ikeda, Surface-enhanced infrared absorption of p-nitrobenzoic acid deposited on silver island films: contributions of electromagnetic and chemical mechanisms, J. Phys. Chem., 95 (1991) 9914-9919.

[109] Y. Nishikawa, K. Fujiwara, T. Shima, A study on the qualitative and quantitative analysis of nanogram samples by transmission infrared spectroscopy with the use of silver island films, Appl. Spectrosc., 45 (1991) 747-751.

[110] D.A. Perry, J.S. Cordova, W.D. Spencer, L.G. Smith, A.S. Biris, SERS, SEIRA, TPD, and DFT study of cyanobenzoic acid isomer film growth on silver nanostructured films and powder, J. Phys. Chem. C, 114 (2010) 14953-14961.

[111] A. Fasasi, P.R. Griffiths, L. Scudiero, Surface-enhanced infrared absorption (SEIRA) of adsorbates on copper nanoparticles synthesized by galvanic displacement, Appl. Spectrosc., 65 (2011) 750-755.

[112] Y. Nishikawa, K. Fujiwara, K. Ataka, M. Osawa, Surface-enhanced infrared external reflection spectroscopy at low reflective surfaces and its application to surface analysis of semiconductors, glasses, and polymers, Anal. Chem., 65 (1993) 556-562.

[113] H. Wanzenböck, B. Mizaikoff, N. Weissenbacher, R. Kellner, Surface enhanced infrared absorption spectroscopy (SEIRA) using external reflection on low-cost substrates, Fresenius' journal of analytical chemistry, 362 (1998) 15-20.

[114] M. Osawa, K.-i. Ataka, Electromagnetic mechanism of enhanced infrared absorption of molecules adsorbed on metal island films, Surf Sci., 262 (1992) L118-L122.

[115] D.A. Heaps, P.R. Griffiths, Reduction of detection limits of the direct deposition GC/FT-IR interface by surface-enhanced infrared absorption, Anal. Chem., 77 (2005) 5965-5972.

[116] D. Enders, A. Pucci, Surface enhanced infrared absorption of octadecanethiol on wet-chemically prepared Au nanoparticle films, Appl. Phys. Lett., 88 (2006) 184104 (184101-184103).

[117] H. Miyake, S. Ye, M. Osawa, Electroless deposition of gold thin films on silicon for surface-enhanced infrared spectroelectrochemistry, Electrochem. Commun., 4 (2002) 973-977.

[118] V. Schettino, R. Bini, Molecules under extreme conditions: Chemical reactions at high pressure, Phys. Chem. Chem. Phys., 5 (2003) 1951-1965.

[119] R. Bini, V. Schettino, Materials under extreme conditions: molecular crystals at high pressure, World Scientific, 2014.

[120] C. Murli, A. Mishra, S. Thomas, S.M. Sharma, Ring-opening polymerization in carnosine under pressure, J. Phys. Chem. B, 116 (2012) 4671-4676.

[121] M. Citroni, M. Ceppatelli, R. Bini, V. Schettino, Laser-induced selectivity for dimerization versus polymerization of butadiene under pressure, Science, 295 (2002) 2058-2060.

[122] P. Pruzan, J. Chervin, M. Thiery, J. Itie, J. Besson, J. Forgerit, M. Revault, Transformation of benzene to a polymer after static pressurization to 30 GPa, J. Chem. Phys., 92 (1990) 6910-6915.

[123] L. Ciabini, M. Santoro, R. Bini, V. Schettino, High pressure photoinduced ring opening of benzene, Phys. Rev. Lett., 88 (2002) 085505 (085501-085504).

[124] F. Cansell, J. Petitet, D. Fabre, High-pressure Raman scattering in dimethyl phenyl silanol, J. Appl. Phys., 65 (1989) 3280-3282.

[125] V. Schettino, R. Bini, Constraining molecules at the closest approach: chemistry at high pressure, Chem. Soc. Rev., 36 (2007) 869-880.

[126] Z. Dong, N.M. Seemann, N. Lu, Y. Song, Effects of high pressure on azobenzene and hydrazobenzene probed by Raman spectroscopy, J. Phys. Chem. B, 115 (2011) 14912-14918.

[127] L. Ciabini, M. Santoro, F.A. Gorelli, R. Bini, V. Schettino, S. Raugei, Triggering dynamics of the high-pressure benzene amorphization, Nat. Mater., 6 (2007) 39-43.

[128] K.K. Zhuravlev, K. Traikov, Z. Dong, S. Xie, Y. Song, Z. Liu, Raman and infrared spectroscopy of pyridine under high pressure, Phys. Rev. B, 82 (2010) 064116 (064111-064118).

[129] H. Drickamer, Pi electron systems at high pressure, Science, 156 (1967) 1712-1712.

[130] H. Sun, M. Yao, Y. Song, L. Zhu, J. Dong, R. Liu, P. Li, B. Zhao, B. Liu, Pressure-induced SERS enhancement in MoS_2/Au/R6G system by a two-step charge transfer process, Nanoscale, 11 (2019) 21493–21501.

[131] P. Li, X. Wang, H. Li, X. Yang, X. Zhang, L. Zhang, Y. Ozaki, B. Liu, B. Zhao, Investigation of charge-transfer between a 4-mercaptobenzoic acid monolayer and TiO 2 nanoparticles under high pressure using surface-enhanced Raman scattering, Chem. Commun., 54 (2018) 6280-6283.

[132] N.K. Gibbs, M. Norval, Urocanic acid in the skin: a mixed blessing?, J Invest Dermatol, 131 (2011) 14-17.

[133] A.R. Young, Chromophores in human skin, Phys Med Biol, 42 (1997) 789-802.

[134] C.N. Palmer, A.D. Irvine, A. Terron-Kwiatkowski, Y. Zhao, H. Liao, S.P. Lee, D.R. Goudie, A. Sandilands, L.E. Campbell, F.J. Smith, Common loss-of-function variants of the epidermal barrier protein filaggrin are a major predisposing factor for atopic dermatitis, Nat. Genet., 38 (2006) 441-446.

[135] N. Chadha, M.S. Bahia, M. Kaur, O. Silakari, Thiazolidine-2, 4-dione derivatives: programmed chemical weapons for key protein targets of various pathological conditions, Biorg. Med. Chem., 23 (2015) 2953-2974.

[136] V.S. Jain, D.K. Vora, C. Ramaa, Thiazolidine-2, 4-diones: Progress towards multifarious applications, Biorg. Med. Chem., 21 (2013) 1599-1620.

[137] R.S. Bhatti, S. Shah, P. Krishan, J.S. Sandhu, Recent pharmacological developments on rhodanines and 2, 4-thiazolidinediones, International journal of medicinal chemistry, 2013 (2013) 1-16.

[138] C. Day, Thiazolidinediones: a new class of antidiabetic drugs, Diabetic Medicine, 16 (1999) 179-192.

[139] M.M. Ip, P.W. Sylvester, L. Schenkel, Antitumor efficacy in rats of CGP 19984, a thiazolidinedione derivative that inhibits luteinizing hormone secretion, Cancer Res., 46 (1986) 1735-1740.

[140] T. Fujita, Y. Sugiyama, S. Taketomi, T. Sohda, Y. Kawamatsu, H. Iwatsuka, Z. Suzuoki, Reduction of insulin resistance in obese and/or diabetic animals by 5-[4-(1-methylcyclohexylmethoxy) benzyl]-thiazolidine-2, 4-dione (ADD-3878, U-63,287, ciglitazone), a new antidiabetic agent, Diabetes, 32 (1983) 804-810.

[141] P. Karagiannidis, S. Hadjikakou, P. Aslanidis, A. Hountas, Synthesis and photochemical study of Cu (I) complexes with tri-p-tolylphosphine and heterocyclic thiones. The crystal structure of [CuCl (pymtH)(p-CH3C6H4) 3P] 2, Inorg. Chim. Acta, 178 (1990) 27-34.

[142] E.S. Raper, Complexes of heterocyclic thione donors, Coord. Chem. Rev., 61 (1985) 115-184.

[143] E. Knoevenagel, Condensation von Malonsäure mit aromatischen Aldehyden durch Ammoniak und Amine, Berichte der deutschen chemischen Gesellschaft, 31 (1898) 2596-2619.

[144] A.P. Roy, S.K. Deb, M.A. Rekha, A.K. Sinha, Multichannel Raman spectroscopy, Ind. J. Pure Appl. Phys., 30 (1992) 724-728.

[145] A.A. Michelson, XXVIII. Visibility of interference-fringes in the focus of a telescope, The London, Edinburgh, and Dublin Philosophical Magazine and Journal of Science, 31 (1891) 256-259.

[146] J.A. Creighton, C.G. Blatchford, M.G. Albrecht, Plasma resonance enhancement of Raman scattering by pyridine adsorbed on silver or gold sol particles of size comparable to the excitation wavelength, Journal of the Chemical Society, Faraday Transactions 2: Molecular and Chemical Physics, 75 (1979) 790-798.

[147] J. Turkevich, P.C. Stevenson, J. Hillier, A study of the nucleation and growth processes in the synthesis of colloidal gold, Discuss. Faraday Soc., 11 (1951) 55-75.

[148] B.R. Kumar, T.S. Rao, AFM studies on surface morphology, topography and texture of nanostructured zinc aluminum oxide thin films, Digest Journal of Nanomaterials and Biostructures, 7 (2012) 1881-1889.

[149] S. Solin, A. Ramdas, Raman spectrum of diamond, Phys. Rev. B, 1 (1970) 1687-1697.

[150] H. Mao, P. Bell, J.t. Shaner, D. Steinberg, Specific volume measurements of Cu, Mo, Pd, and Ag and calibration of the ruby R 1 fluorescence pressure gauge from 0.06 to 1 Mbar, J. Appl. Phys., 49 (1978) 3276-3283.

[151] G. Piermarini, S. Block, Ultrahigh pressure diamond-anvil cell and several semiconductor phase transition pressures in relation to the fixed point pressure scale, Rev. Sci. Instrum., 46 (1975) 973-979.

[152] H. Mao, J.-A. Xu, P. Bell, Calibration of the ruby pressure gauge to 800 kbar under quasi-hydrostatic conditions, Journal of Geophysical Research: Solid Earth, 91 (1986) 4673-4676.

[153] W.L. Ryan, D.H. Levy, Electronic spectroscopy and photoisomerization of trans-urocanic acid in a supersonic jet, J. Am. Chem. Soc., 123 (2001) 961-966.

[154] K.M. Hanson, B. Li, J.D. Simon, A Spectroscopic Study of the Epidermal Ultraviolet Chromophore trans-Urocanic Acid, J. Am. Chem. Soc., 119 (1997) 2715-2721.

[155] J. Brookman, J.N. Chacon, R.S. Sinclair, Some photophysical studies of cis- and trans-urocanic acid, Photochem. Photobiol. Sci, 1 (2002) 327-332.

[156] J. Danielsson, A. Laaksonen, Gas phase photoisomerization of urocanic acid – a theoretical study, Chem. Phys. Lett., 370 (2003) 625-630.

[157] D. Tuna, A.L. Sobolewski, W. Domcke, Photochemical mechanisms of radiationless deactivation processes in urocanic acid, J. Phys. Chem. B, 118 (2014) 976-985.

[158] E.C. De Fabo, F.P. Noonan, Mechanism of immune suppression by ultraviolet irradiation in vivo. I. Evidence for the existence of a unique photoreceptor in skin and its role in photoimmunology, J Exp Med, 158 (1983) 84-98.

[159] D. Tuna, L. Spörkel, M. Barbatti, W. Thiel, Nonadiabatic dynamics simulations of photoexcited urocanic acid, Chem. Phys., 515 (2018) 521-534.

[160] M. Barbatti, The role of tautomers in the UV absorption of urocanic acid, Phys. Chem. Chem. Phys., 13 (2011) 4686-4692.

[161] H. Sharma, P.K. Mishra, S. Talegaonkar, B. Vaidya, Metal nanoparticles: a theranostic nanotool against cancer, Drug Discov. Today, 20 (2015) 1143-1151.

[162] H. Liao, C.L. Nehl, J.H. Hafner, Biomedical applications of plasmon resonant metal nanoparticles, (2006).

[163] M.S. Khan, G.D. Vishakante, H. Siddaramaiah, Gold nanoparticles: a paradigm shift in biomedical applications, Adv. Colloid Interface Sci., 199 (2013) 44-58.

[164] L. Wei, J. Lu, H. Xu, A. Patel, Z.-S. Chen, G. Chen, Silver nanoparticles: synthesis, properties, and therapeutic applications, Drug Discov. Today, 20 (2015) 595-601.

[165] A.D. Becke, A new mixing of Hartree–Fock and local density-functional theories, J. Chem. Phys., 98 (1993) 1372-1377.

[166] M. Frisch, G. Trucks, H. Schlegel, G. Scuseria, M. Robb, J. Cheeseman, J. Montgomery Jr, T. Vreven, K. Kudin, J. Burant, Gaussian 03, revision c. 02; Gaussian, Inc., Wallingford, CT, 4 (2004).

[167] M. Shukla, P. Mishra, Electronic spectra, structure and photoisomerization of urocanic acid, Spectrochimica Acta Part A: Molecular and Biomolecular Spectroscopy, 51 (1995) 831-838.

[168] O. Dmitrenko, W. Reischl, R.D. Bach, J. Spanget-Larsen, TD-DFT computational insight into the origin of wavelength-dependent E/Z photoisomerization of urocanic acid, J. Phys. Chem. A, 108 (2004) 5662-5669.

[169] C.S. Page, M. Olivucci, M. Merchán, A theoretical study of the low-lying states of the anionic and protonated ionic forms of urocanic acid, J. Phys. Chem. A, 104 (2000) 8796-8805.

[170] E. Liang, C. Engert, W. Kiefer, Surface-enhanced Raman spectroscopy of p-aminobenzoic acid with excitation in the visible and near infrared spectral region, Vib. Spectrosc., 6 (1993) 79-85.

[171] S. Sánchez-Cortés, J.V. García-Ramos, G. Morcillo, A. Tinti, Morphological Study of Silver Colloids Employed in Surface-Enhanced Raman Spectroscopy: Activation when Exciting in Visible and Near-Infrared Regions, J. Colloid Interface Sci., 175 (1995) 358-368.

[172] E. Liang, C. Engert, W. Kiefer, Surface-enhanced Raman scattering of pyridine in silver colloids excited in the near-infrared region, J. Raman Spectrosc., 24 (1993) 775-779.

[173] S. Hawkinson, Urocanic acid dihydrate (4-imidazoleacrylic acid dihydrate), Acta Crystallographica Section B: Structural Crystallography and Crystal Chemistry, 33 (1977) 2288-2291.

[174] T. Mohammad, H. Morrison, H. HogenEsch, Urocanic Acid Photochemistry and Photobiology, Photochem. Photobiol., 69 (1999) 115-135.

[175] V. Arjunan, P. Remya, U. Sathish, T. Rani, S. Mohan, Spectroscopic and density functional theory studies of trans-3-(trans-4-imidazolyl)acrylic acid, Spectrochimica Acta Part A: Molecular and Biomolecular Spectroscopy, 129 (2014) 466-477.

[176] S. Thomas, N. Biswas, V.V. Malkar, T. Mukherjee, S. Kapoor, Studies on adsorption of carnosine on silver nanoparticles by SERS, Chem. Phys. Lett., 491 (2010) 59-64.

[177] J. Suh, K. Michaelian, Surface-enhanced Raman scattering as a probe of surface geometry effects on the polymerization of a acrylic acid on silver, J. Phys. Chem., 91 (1987) 598-600.

[178] P.N. Sanda, J.M. Warlaumont, J.E. Demuth, J.C. Tsang, K. Christmann, J.A. Bradley, Surface-Enchanced Raman Scattering from Pyridine on Ag(111), Phys. Rev. Lett., 45 (1980) 1519-1523.

[179] U.K. Sarkar, A. Pal, S. Chakrabarti, T. Misra, Classical and chemical effects of SERS from 2, 2′: 5, 2 ″terthiophene adsorbed on Ag-sols, Chem. Phys. Lett., 190 (1992) 59-63.

[180] C. Murli, Y. Song, Pressure-induced polymerization of acrylic acid: a Raman spectroscopic study, J. Phys. Chem. B, 114 (2010) 9744-9750.

[181] F. Li-Mei, L. Chun-Yu, M. Zhi-Wei, S. Cheng-Lin, Z. Mi, High pressure Raman investigations on crystalline crotonic acid, Optik-International Journal for Light and Electron Optics, 127 (2016) 3112-3116.

[182] R. Kiyama, S. Minomura, Cis-trans isomerization of maleic acid to fumaric acid under pressure, The Physico-Chemical Society of Japan, 22 (1952) 4-8.

[183] G. Yang, Z. Dreger, Y. Li, H. Drickamer, Pressure-Induced Isomerization of 2-(2 ‘-Hydroxyphenyl) Benzoxazole in Solid Media, J. Phys. Chem. A, 101 (1997) 7948-7952.

[184] M. Tabata, H. Takamura, K. Yokota, Y. Nozaki, T. Hoshina, H. Minakawa, K. Kodaira, Pressure-induced cis to trans isomerization of poly (o-methoxyphenylacetylene) polymerized by Rh complex catalyst. A Raman, x-ray, and ESR study, Macromolecules, 27 (1994) 6234-6236.

[185] G. Vinogradov, Y.Y. Bit-Gevorgizov, Y.L. Frenkin, Y.Y. Podol'skii, Properties and features of the structure of polybutadiene crosslinked under pressure, Polymer Science USSR, 33 (1991) 983-986.

[186] M. Tabata, Y. Tanaka, Y. Sadahiro, T. Sone, K. Yokota, I. Miura, Pressure-induced cis to trans isomerization of aromatic polyacetylenes. 2. Poly ((o-ethoxyphenyl) acetylene) stereoregularly polymerized using a Rh complex catalyst, Macromolecules, 30 (1997) 5200-5204.

[187] R. D'Amato, T. Sone, M. Tabata, Y. Sadahiro, M.V. Russo, A. Furlani, Pressure-induced cis to trans isomerization of poly ((p-nitrophenyl) acetylene) prepared using Rh complex catalysts. Extension of π conjugation length, Macromolecules, 31 (1998) 8660-8665.

[188] B. Loo, Y. Tse, K. Parsons, C. Adelman, A. El-Hage, Y. Lee, Surface-enhanced Raman spectroscopy of imidazole adsorbed on electrode and colloidal surfaces of Cu, Ag, and Au, J. Raman Spectrosc., 37 (2006) 299-304.

[189] G. Kister, G. Cassanas, E. Fabregue, L. Bardet, Vibrational analysis of ring-opening polymerizations of glycolide, L-lactide and D, L-lactide, Eur. Polym. J., 28 (1992) 1273-1277.

[190] D. Lin-Vien, N.B. Colthup, W.G. Fateley, J.G. Grasselli, The handbook of infrared and Raman characteristic frequencies of organic molecules, Elsevier, 1991.

[191] B.G.a.L.P. M. Bourguel, Compt. rend., 195 (1932) 129

[192] G. Johnson, R. Machado, K. Freidl, M. Achenbach, P. Clark, S. Reidy, Evaluation of Raman spectroscopy for determining cis and trans isomers in partially hydrogenated soybean oil, Organic process research & development, 6 (2002) 637-644.

[193] G.F. Bailey, R.J. Horvat, Raman spectroscopic analysis of thecis/trans isomer composition of edible vegetable oils, J. Am. Oil Chem. Soc., 49 (1972) 494-498.

[194] B.C. Smith, The infrared spectroscopy of Alkenes, (2016).

[195] G.J. Puppels, P.J. Caspers, G.W. Lucassen, Depth selective pH measurement and UV exposure measurement, in, Google Patents, 2010.

[196] M. Egawa, J. Nomura, H. Iwaki, The evaluation of the amount of cis- and trans-urocanic acid in the stratum corneum by Raman spectroscopy, Photochem. Photobiol. Sci, 9 (2010) 730-733.

[197] J.H. Anglin, In vivo changes in urocanic acid of guinea pig and human epidermis by ultraviolet light, in, PhD diss., 1962.

[198] J. Umemura, S. Hayashi, Infrared spectra and molecular configurations of liquid and crystalline acrylic acids, Bull. Inst. Chem. Res, Kyoto Univ., (1975) 585-595.

[199] T.A. Singleton, K.S. Ramsay, M.M. Barsan, I.S. Butler, C.J. Barrett, Azobenzene photoisomerization under high external pressures: testing the strength of a light-activated molecular muscle, J. Phys. Chem. B, 116 (2012) 9860-9865.

[200] C.C. Trout, J.V. Badding, Solid state polymerization of acetylene at high pressure and low temperature, J. Phys. Chem. A, 104 (2000) 8142-8145.

[201] K. Aoki, Y. Kakudate, M. Yoshida, S. Usuba, S. Fujiwara, Solid state polymerization of cyanoacetylene into conjugated linear chains under pressure, J. Chem. Phys., 91 (1989) 778-782.

[202] C. Dugave, L. Demange, Cis− trans isomerization of organic molecules and biomolecules: implications and applications, Chem. Rev., 103 (2003) 2475-2532.

[203] L. Kang, P. Xu, B. Zhang, H. Tsai, X. Han, H.-L. Wang, Laser wavelength-and power-dependent plasmon-driven chemical reactions monitored using single particle surface enhanced Raman spectroscopy, Chem. Commun., 49 (2013) 3389-3391.

[204] R. Chadha, N. Maiti, S. Kapoor, Catalytic Reactions on the Surface of Ag Nanoparticles: A Photochemical Effect and/or Molecule Property?, J. Phys. Chem. C, 118 (2014) 26227-26235.

[205] A.C. Dhayagude, N. Maiti, A.K. Debnath, S.S. Joshi, S. Kapoor, Metal nanoparticle catalyzed charge rearrangement in selenourea probed by surface-enhanced Raman scattering, RSC Advances, 6 (2016) 17405-17414.

[206] S. Mukherjee, F. Libisch, N. Large, O. Neumann, L.V. Brown, J. Cheng, J.B. Lassiter, E.A. Carter, P. Nordlander, N.J. Halas, Hot electrons do the impossible: plasmon-induced dissociation of H2 on Au, Nano Lett., 13 (2012) 240-247.

[207] W. Xie, B. Walkenfort, S. Schlücker, Label-free SERS monitoring of chemical reactions catalyzed by small gold nanoparticles using 3D plasmonic superstructures, J. Am. Chem. Soc., 135 (2012) 1657-1660.

[208] J. Lee, S. Mubeen, X. Ji, G.D. Stucky, M. Moskovits, Plasmonic photoanodes for solar water splitting with visible light, Nano Lett., 12 (2012) 5014-5019.

[209] V. Joseph, C. Engelbrekt, J. Zhang, U. Gernert, J. Ulstrup, J. Kneipp, Characterizing the kinetics of nanoparticle-catalyzed reactions by surface-enhanced Raman scattering, Angew. Chem. Int. Ed., 51 (2012) 7592-7596.

[210] B. Dong, Y. Fang, L. Xia, H. Xu, M. Sun, Is 4-nitrobenzenethiol converted to p, p′-dimercaptoazobenzene or 4-aminothiophenol by surface photochemistry reaction?, J. Raman Spectrosc., 42 (2011) 1205-1206.

[211] X. Ren, E. Cao, W. Lin, Y. Song, W. Liang, J. Wang, Recent advances in surface plasmon-driven catalytic reactions, RSC Advances, 7 (2017) 31189-31203.

[212] A. Merlen, M. Chaigneau, S. Coussan, Vibrational modes of aminothiophenol: a TERS and DFT study, Phys. Chem. Chem. Phys., 17 (2015) 19134-19138.

[213] E.A. Sprague-Klein, B. Negru, L.R. Madison, S.C. Coste, B.K. Rugg, A.M. Felts, M.O. McAnally, M. Banik, V.A. Apkarian, M.R. Wasielewski, Photoinduced plasmon-driven chemistry in trans-1, 2-bis (4-pyridyl) ethylene gold nanosphere oligomers, J. Am. Chem. Soc., 140 (2018) 10583-10592.

[214] Z. Zhang, D. Kinzel, V. Deckert, Photo-induced or plasmon-induced reaction: Investigation of the light-induced Azo-coupling of amino groups, J. Phys. Chem. C, 120 (2016) 20978-20983.

[215] Q. Ding, M. Chen, Y. Fang, Z. Zhang, M. Sun, Plasmon-driven diazo coupling reactions of p-nitroaniline via− NH2 or− NO2 in atmosphere environment, J. Phys. Chem. C, 121 (2017) 5225-5231.

[216] N.C. Brandt, E.L. Keller, R.R. Frontiera, Ultrafast surface-enhanced raman probing of the role of hot electrons in plasmon-driven chemistry, J. Phys. Chem. Lett., 7 (2016) 3179-3185.

[217] M.J. Kale, T. Avanesian, H. Xin, J. Yan, P. Christopher, Controlling catalytic selectivity on metal nanoparticles by direct photoexcitation of adsorbate–metal bonds, Nano Lett., 14 (2014) 5405-5412.

[218] Z. Zhang, T. Deckert-Gaudig, P. Singh, V. Deckert, Single molecule level plasmonic catalysis–a dilution study of p-nitrothiophenol on gold dimers, Chem. Commun., 51 (2015) 3069-3072.

[219] S. Jabeen, T.J. Dines, R. Withnall, S.A. Leharne, B.Z. Chowdhry, Surface-enhanced Raman scattering studies of rhodanines: evidence for substrate surface-induced dimerization, Phys. Chem. Chem. Phys., 11 (2009) 7476-7483.

[220] G. Jones, The K noevenagel Condensation, Organic reactions, 15 (2004) 204-599.

[221] Z.S. Safi, A theoretical study on the structure of thiazolidine-2, 4-dione and its 5-substituted derivatives in the gas phase. Implications for the thiazolidine-2, 4-dione-water complex, Arabian Journal of Chemistry, 9 (2016) 616-625.

[222] V. Enchev, S. Chorbadjiev, B. Jordanov, Comparative study of the structure of rhodanine, isorhodanine, thiazolidine-2, 4-dione, and thiorhodanine, Chemistry of heterocyclic compounds, 38 (2002) 1110-1120.

[223] G. Form, E. Raper, T. Downie, The crystal and molecular structure of thiazolidine-2, 4-dione, Acta Crystallographica Section B: Structural Crystallography and Crystal Chemistry, 31 (1975) 2181-2184.

[224] R.N. Devi, M.G. Khrenova, S. Israel, C. Anzline, A.A. Astakhov, V.G. Tsirelson, Testing the ability of rhodanine and 2, 4-thiazolidinedione to interact with the human pancreatic alpha-amylase: electron-density descriptors complement molecular docking, QM, and QM/MM dynamics calculations, J. Mol. Model., 23 (2017) 252.

[225] R. Hilal, H. Ead, A. Osman, A molecular orbital treatment of the electronic structure and spectra of tautomeric rhodanines, Appl. Spectrosc., 32 (1978) 557-563.

[226] S.R. Mahalle, P.D. Netankar, S.P. Bondge, R.A. Mane, An efficient method for Knoevenagel condensation: a facile synthesis of 5-arylidenyl 2, 4-thiazolidinedione, Green Chem. Lett. Rev., 1 (2008) 103-106.

[227] S. Haferkamp, F. Fischer, W. Kraus, F. Emmerling, Mechanochemical Knoevenagel condensation investigated in situ, Beilstein J. Org. Chem., 13 (2017) 2010-2014.

[228] E.L. Keller, R.R. Frontiera, Ultrafast nanoscale Raman thermometry proves heating is not a primary mechanism for plasmon-driven photocatalysis, ACS nano, 12 (2018) 5848-5855.

[229] Y. Li, X. Cao, L. Zhan, J. Xue, J. Wang, C. Xiong, Z. Nie, Hot electron transfer promotes ion production in plasmonic metal nanostructure assisted laser desorption ionization mass spectrometry, Chem. Commun., 54 (2018) 10905-10908.

[230] M. Moskovits, J. Suh, The geometry of several molecular ions adsorbed on the surface of colloidal silver, J. Phys. Chem., 88 (1984) 1293-1298.

[231] N. Kumar, S. Thomas, R. Rao, N. Maiti, R.J. Kshirsagar, Plasmon–Induced Dimerization of Thiazolidine-2, 4-Dione on Silver Nanoparticles-Revealed by Surface-Enhanced Raman Scattering Study, J. Phys. Chem. A, 123 (2019) 9770-9780.

[232] C.J. Murphy, A.M. Gole, J.W. Stone, P.N. Sisco, A.M. Alkilany, E.C. Goldsmith, S.C. Baxter, Gold nanoparticles in biology: beyond toxicity to cellular imaging, Accounts of chemical research, 41 (2008) 1721-1730.

[233] J.L. Elechiguerra, J.L. Burt, J.R. Morones, A. Camacho-Bragado, X. Gao, H.H. Lara, M.J. Yacaman, Interaction of silver nanoparticles with HIV-1, J. Nanobiotechnology, 3 (2005) 1-10.

[234] P. Gómez-Romero, C. Sanchez, Functional hybrid materials, John Wiley & Sons, 2006.

[235] A. Wibbertmann, J. Kielhorn, G. Koennecker, I. Mangelsdorf, C. Melber, Concise International Chemical Assessment Document 26. Benzoic acid and sodium benzoate, World Health Organisation Geneva, 26 (2000) 1-48.

[236] J.R. Chipley, Sodium benzoate and benzoic acid, FOOD SCIENCE AND TECHNOLOGY-NEW YORK-MARCEL DEKKER-, 145 (2005) 11.

[237] J.G. Castro, M.R. Delgado, M. Sánchez, F.G. Montelongo, Simultaneous 2nd order derivative spectrophotometry determination of sorbic and benzoic acids in soft drinks, Anal. Lett., 25 (1992) 2367-2376.

[238] W. Lewandowski, B. Dasiewicz, P. Koczoń, J. Skierski, K. Dobrosz-Teperek, R. Świsłocka, L. Fuks, W. Priebe, A. Mazurek, Vibrational study of alkaline metal nicotinates, benzoates and salicylates, J. Mol. Struct., 604 (2002) 189-193.

[239] K. Machida, A. Kuwae, Y. Saito, T. Uno, Vibrational spectra of sodium benzoate-d0,-pd and-d5 and normal vibrations of benzoate ion, Spectrochimica Acta Part A: Molecular Spectroscopy, 34 (1978) 793-800.

[240] S.-H. Choi, H.G. Park, Surface-enhanced Raman scattering (SERS) spectra of sodium benzoate and 4-picoline in Ag colloids prepared by γ-irradiation, Appl. Surf. Sci., 243 (2005) 76-81.

[241] T. Bouckenooghe, C. Remacle, B. Reusens, Is taurine a functional nutrient?, Current Opinion in Clinical Nutrition & Metabolic Care, 9 (2006) 728-733.

[242] Y.-J. Xu, A.S. Arneja, P.S. Tappia, N.S. Dhalla, The potential health benefits of taurine in cardiovascular disease, Experimental & Clinical Cardiology, 13 (2008) 57-65.

[243] J.A. Sturman, Taurine in development, Physiol. Rev., 73 (1993) 119-147.

[244] W.X. Kong, S.W. Chen, Y.L. Li, Y.J. Zhang, R. Wang, L. Min, X. Mi, Effects of taurine on rat behaviors in three anxiety models, Pharmacol. Biochem. Behav., 83 (2006) 271-276.

[245] K. Ohno, Y. Mandai, H. Matsuura, Vibrational spectra and molecular conformation of taurine and its related compounds, J. Mol. Struct., 268 (1992) 41-50.

[246] P. Freire, F. Melo, J. Mendes Filho, Polarized Raman and infrared spectra of taurine crystals, J. Raman Spectrosc., 27 (1996) 507-512.

[247] C. Garrigou-Lagrange, Analyse des spectres de vibration de la β-alanine, de la taurine et de la ciliatine-β, Can. J. Chem., 56 (1978) 663-669.

[248] O. Seitz, M.M. Chehimi, E. Cabet-Deliry, S. Truong, N. Felidj, C. Perruchot, S.J. Greaves, J.F. Watts, Preparation and characterisation of gold nanoparticle assemblies on silanised glass plates, Colloids Surf. Physicochem. Eng. Aspects, 218 (2003) 225-239.

[249] N. Peica, C. Lehene, N. Leopold, O. Cozar, W. Kiefer, Raman and surface-enhanced Raman studies of the food additive sodium benzoate, Journal of optoelectronics and advanced materials, 9 (2007) 2943-2948.

[250] J. Kundu, O. Neumann, B. Janesko, D. Zhang, S. Lal, A. Barhoumi, G. Scuseria, N. Halas, Adenine− and adenosine monophosphate (AMP)− gold binding interactions studied by surface-enhanced Raman and infrared spectroscopies, J. Phys. Chem. C, 113 (2009) 14390-14397.

[251] P. Stoliar, E. Bystrenova, S. Quiroga, P. Annibale, M. Facchini, M. Spijkman, S. Setayesh, D. De Leeuw, F. Biscarini, DNA adsorption measured with ultra-thin film organic field effect transistors, Biosensors Bioelectron., 24 (2009) 2935-2938.

[252] W. Göpel, Controlled signal transduction across interfaces of “intelligent” molecular systems, Biosensors Bioelectron., 10 (1995) 35-59.

[253] H. Susi, J.S. Ard, Vibrational spectra of nucleic acid constituents—I: planar vibrations of uracil, Spectrochimica Acta Part A: Molecular Spectroscopy, 27 (1971) 1549-1562.

[254] J. Bandekar, G. Zundel, Normal coordinate analysis treatment on uracil in solid state, Spectrochimica Acta Part A: Molecular Spectroscopy, 39 (1983) 343-355.

[255] J. Florián, V. Hrouda, Scaled quantum mechanical force fields and vibrational spectra of solid state nucleic acid constituents V: thymine and uracil, Spectrochimica Acta Part A: Molecular Spectroscopy, 49 (1993) 921-938.

[256] D.A. Heaps, P.R. Griffiths, Band shapes in the infrared spectra of thin organic films on metal nanoparticles, Vib. Spectrosc., 42 (2006) 45-50.

[257] M.M. Killian, E. Villa-Aleman, Z. Sun, S. Crittenden, C.L. Leverette, Dependence of surface-enhanced infrared absorption (SEIRA) enhancement and spectral quality on the choice of underlying substrate: a closer look at Silver (Ag) films prepared by physical vapor deposition (PVD), Appl. Spectrosc., 65 (2011) 272-283.

[258] Z. Zhang, T. Imae, Study of surface-enhanced infrared spectroscopy: 1. Dependence of the enhancement on thickness of metal island films and structure of chemisorbed molecules, J. Colloid Interface Sci., 233 (2001) 99-106.

[259] D. Enders, T. Nagao, A. Pucci, T. Nakayama, M. Aono, Surface-enhanced ATR-IR spectroscopy with interface-grown plasmonic gold-island films near the percolation threshold, Phys. Chem. Chem. Phys., 13 (2011) 4935-4941.

[260] N. Kumar, S. Thomas, R. Kshirsagar, FTIR study of thin film of uracil on silanised glass substrate using attenuated total reflection (ATR), in: AIP Conf. Proc., AIP, 2013, pp. 716-717.

[261] S. Kawata, M. Ohtsu, M. Irie, Near-field optics and surface plasmon polaritons, Springer Science & Business Media, 2001.

[262] S. Pronkin, T. Wandlowski, Time-resolved in situ ATR-SEIRAS study of adsorption and 2D phase formation of uracil on gold electrodes, Journal of Electroanalytical Chemistry, 550 (2003) 131-147.

[263] N. Kumar, S. Thomas, R. Tokas, R. Kshirsagar, Investigation on the adsorption characteristics of sodium benzoate and taurine on gold nanoparticle film by ATR–FTIR spectroscopy, Spectrochimica Acta Part A: Molecular and Biomolecular Spectroscopy, 118 (2014) 614-618.

[264] M. Yilmaz, E. Babur, M. Ozdemir, R.L. Gieseking, Y. Dede, U. Tamer, G.C. Schatz, A. Facchetti, H. Usta, G. Demirel, Nanostructured organic semiconductor films for molecular detection with surface-enhanced Raman spectroscopy, Nat. Mater., 16 (2017) 918-924.

[265] F. Jensen, Introduction to computational chemistry, John wiley & sons, 2017.

[266] P. Hohenberg, W. Kohn, Inhomogeneous electron gas, Phys. Rev., 136 (1964) 864-870.

[267] W. Kohn, L.J. Sham, Self-consistent equations including exchange and correlation effects, Phys. Rev., 140 (1965) 1133-1137.

[268] A.A. Altaf, S. Kausar, A. Badshah, Spectral Calculations with DFT, Density Functional Calculations: Recent Progresses of Theory and Application, (2018) 101-127.